Computational Studies of the Oxygen Evolution Reaction on Oxynitride Catalysts

Lan, Zhenyun

Publication date:
2021

Document Version
Publisher's PDF, also known as Version of record

Technical University of Denmark

Computational Studies of the Oxygen Evolution Reaction on Oxynitride Catalysts

Zhenyun Lan

Ph.D. Thesis

Department of Energy Conversion and Storage

Technical University of Denmark

August 2021

Computational Studies of the Oxygen Evolution Reaction on Oxynitrides Catalysts

August 31th, 2021

Authors

Zhenyun Lan

zhenlan@.dtu.dk

Supervisors

Professor Tejs Vegge

Section for Atomic Scale Materials Modelling

Department of Energy Conversion and Storage

Technical University of Denmark

E-mail: teve@dtu.dk

Associate Professor Ivano Eligio Castelli

Section for Atomic Scale Materials Modelling

Department of Energy Conversion and Storage

Technical University of Denmark

E-mail: ivca@dtu.dk

Department of Energy Conversion and Storage

Technical University of Denmark

Fysikvej, Building 301

2800 Kgs. Lyngby, Denmark

www.energy.dtu.dk

Tel: +45 46 77 58 00

E-mail: info@energy.dtu.dkqi

Preface and acknowledgement

This dissertation is submitted to Technical University of Denmark (DTU) for the degree of Doctor of Philosophy (Ph.D.). The work has been carried out over the last three years at the Section for Atomic Scale Materials Modelling, Department of Energy Conversion and Storage, DTU, under the supervision of Professor Tejs Vegge and the co-supervision of Associate Professor Ivano Eligio Castelli. Also, I gratefully acknowledge the financial support from China Scholarship Council.

My three-years life in DTU is coming to an end, I would like to thank everyone I met and worked with here. First, I would like to express my sincere appreciation to my supervisors, Professor Tejs Vegge and Associate Professor Ivano Eligio Castelli for their constant support, valuable suggestions and kindness over the past three years. Meanwhile, I would also like to thank Professor Ulrich Aschauer from University of Bern and Dr. Didrik René Småbråten for their support and very useful scientific discussions during my external stay.

Secondly, many thanks to my nice colleagues from the section of Atomic Scale Materials Modelling, DTU. In particular, Karina Ulvskov Frederiksen guided me a lot on preparing the important documents and Steen Lysgaard gave me IT support. I would like to thank Alexandra Craft Ludvigsen for helping to translate the abstract of this thesis into Danish. Thank you all to make my stay in DTU enjoyable.

Finally, I would like to thank my families and boyfriend for their endless support and love.

Zhenyun Lan

August 2021, Lyngby Denmark

Contributions during PhD project

This thesis is mainly based on the following papers.

1. Theoretical Insight on Anion Ordering, Strain, and Doping Engineering of the Oxygen Evolution Reaction in $BaTaO_2N$ (Chapter 3)

Zhenyun Lan, Tejs Vegge, Ivano E. Castelli *

Chem. Mater. 2021, 33, 9, 3297–3303

2. Enhancing Oxygen Evolution Reaction Activity by Using Switchable Polarization in Ferroelectric $InSnO_2N$ (Chapter 4)

Zhenyun Lan, Didrik René Småbråten, Chengcheng Xiao, Tejs Vegge, Ulrich Aschauerb,* and Ivano E. Castelli* (Submitted)

Other Publications not included in this thesis

(1) **Lan, Z.**, Meng, J, Zheng K, et al. Exploring the Intrinsic Point Defects in Cesium Copper Halides. J. Phys. Chem. C, 2021, 125, 1592-1598.

(2) Meng, J. †, **Lan, Z.**†, Castelli I E, et al. Atomic-Scale Observation of Oxygen Vacancy-Induced Step Reconstruction in WO_3. J. Phys. Chem. C, 2021, 125, 8456-8460.

(3) Meng, J.†, **Lan, Z.**†, Abdellah, M., et al. Modulating Charge-Carrier Dynamics in Mn-Doped All-Inorganic Halide Perovskite Quantum Dots through the Doping-Induced Deep Trap States. J. Phys. Chem. Lett. 2020, 11, 3705–3711.

(4) Liang, M., Lin, W., **Lan, Z.**, et al. Electronic Structure and Trap States of Two-Dimensional Ruddlesden–Popper Perovskites with the Relaxed Goldschmidt Tolerance Factor. ACS Appl. Electron. Mater. 2020, 2, 1402–1412.

(5) Liang, M., Lin, W., Zhao, Q., Zou, X., **Lan, Z.**, et al. Free Carriers versus Self-Trapped Excitons at Different Facets of Ruddlesden–Popper Two-Dimensional Lead Halide Perovskite Single Crystals. J. Phys. Chem. Lett. 2021, 12, 4965-4971.

Abstract

Over the last decade, oxynitride materials have been demonstrated to be the most promising materials for water splitting into oxygen and hydrogen. Despite this, the overpotentials needed to drive these reactions are still far from the minimum theoretical values. The oxygen evolution reaction (OER), in particular, is the most serious bottleneck to enable a direct splitting of water using visible light, which can accelerate the transition to a sustainable future. Doping, strain and polarization engineering have been proved to be effective methods in tailoring the surface electronic structures and catalytic properties. Therefore, in this thesis, we apply density functional theory (DFT) to investigate the effects that doping, strain and polarization engineering have on the OER, providing valuable suggestions to guide experiments towards more efficient OER activity.

The first work (Chapter 3) studies the effect of anion ordering, strain, and doping engineering of the OER in $BaTaO_2N$. Here, we use DFT simulations to show that strain and surface doping can be applied to enhance the OER performance. For the TaON-terminated $BaTaO_2N$ (001) surfaces, by applying 4% compressive uniaxial strain, the theoretical overpotential can be reduced to 0.59 V. While for the most stable TaO_2N-(100) surface, a small tensile uniaxial strain of 1%, which is easily reached by experiments, can reduce the theoretical overpotential from 0.43 V to 0.37 V under (photo)electrochemical conditions. This value is very close to the minimum predicted theoretical overpotential of oxides.

The second work (Chapter 4) shows switchable polarization modulation on the OER activity in ferroelectric $InSnO_2N$. Basing on DFT calculation, we have theoretically studied how the surface ferroelectric switching affects the OER performance of the improper ferroelectric $InSnO_2N$. For the clean surface, the surface with negatively polarized bulk has a lower theoretical overpotential of 0.58 V than the surface with positively polarized bulk (0.77 V), due to the increased surface electrons density. Under (photo)-electrochemical operating condition, for the surface with negatively polarized bulk, a 1 monolayer (ML) OH coverage is preferred, while for the positively polarized bulk, a 2/3 ML OH covered surface is the most stable. The theoretical overpotentials of the OER on the OH-covered surfaces with negatively and positively polarized bulk are equal (0.89 V). Switching the polarization direction during the OER, much lower theoretical

overpotentials are obtained, 0.20 V for the clean surface and 0.23 V for the surface with OH coverage. These values are far below the minimum theoretical overpotential for oxides (0.37 V).

Resumé

I løbet af det sidste årti har oxynitride materialer vist sig at være de mest lovende materialer til at splitte vand til oxygen og hydrogen. På trods af det, er de overpotentialer som er nødvendige for at aktivere disse reaktioner stadig langt fra minimum af de teoretiske værdier. Især oxygenudviklingsreaktionen (OER) er den mest alvorlige flaskehals for at muliggøre en direkte spaltning af vand ved hjælp af synligt lys, hvilket kan accelerere overgangen til en bæredygtig fremtid. Doping, belastning og polariserings teknikker har vist sig at være effektive metoder til at skræddersy de overfladiske elektroniske strukturer og katalytiske egenskaber. Derfor anvender vi i denne afhandling densitet funktionel teori (DFT) for at undersøge den effekt som doping, belastning og polariserings teknikker har på OER, hvilket giver værdifulde forslag til at lede eksperimenter mod en mere effektiv OER aktivitet.

Det første arbejde (kapitel 3) studerer effekten af anion rækkefølger, belastning og doping teknikker af OER i $BaTaO_2N$. Her bruger vi DFT-simuleringer til at vise, at belastning og overfladedoping kan anvendes til at forbedre OER præstationen. For de TaON-terminerede $BaTaO_2N$ (001) overflader, kan det teoretiske overpotentiale reduceres til 0.59 V ved at påføre 4% ensartet kompressiv belastning. Mens det for den mest stabile TaO_2N-(100) overflade er en lille ensartet træk belastning på 1%, som let opnås ved forsøg, der kan reducere det teoretiske overpotentiale fra 0.43 V til 0.37 V under (foto)elektrokemiske forhold. Denne værdi er meget tæt på det laveste forudsagte teoretiske overpotentiale for oxider.

Det andet arbejde (kapitel 4) viser omskiftelig polarisationsmodulation på OER aktiviteten i ferroelektriske $InSnO_2N$. Baseret på DFT beregning har vi teoretisk undersøgt, hvordan de overfladiske ferroelektriske skift påvirker OER præstationen for den ikke passende ferroelektriske $InSnO_2N$. For den rene overflade har overfladen med negativt polariseret bulk et lavere teoretisk

overpotentiale på 0.58 V end overfladen med positivt polariseret bulk (0.77 V) på grund af den øgede overflade elektrondensitet. Under (foto)-elektrokemisk driftstilstand foretrækkes overfladen med negativt polariseret bulk med en 1 monolags (ML) OH-dækning, mens for den positivt polariserede bulk er en 2/3 ML OH overdækket overflade den mest stabile. De teoretiske overpotentialer for OER på de OH-dækkede overflader med negativt og positivt polariseret bulk er ens, begge på 0.89 V. Ved at skifte polarisationsretningen under OER opnås meget lavere teoretiske overpotentialer, 0.20 V for den rene overflade og 0.23 V for overfladen med OH -dækning. Disse værdier er langt under det minimum teoretiske overpotentiale for oxider (0.37 V).

Abbreviations

DFT: density functional theory

OER: oxygen evolution reaction

ML: monolayer

PEC: photoelectrochemical

VB: valence band

CB: conduction band

HER: hydrogen evolution reaction

TF: Thomas-Fermi

HK: Hohenberg-Kohn

XC: exchange-correlation

LDA: local spin density approximation

LSDA: local spin density approximation

GGA: Generalized Gradient Approximation

PCET: proton-coupled electron-transfer

VASP: Vienna Ab initio Simulation Package

QE: quantum espresso

PCET: proton-coupled electron-transfer

DFPT: density functional perturbation theory

VBM: valence band maximum

CBM: conduction band minimum

PDS: potential determining step

PBE: Perdew-Burke-Ernerhof

SHE: standard hydrogen electrode

PDOS: partial density of states

PAW: projector augmented wave

Contents

Preface and acknowledgement ..... **III**
Contributions during PhD project ..... **IV**
Abstract ..... **VI**
Resumé ..... **VIII**
Abbreviations ..... **X**
Chapter 1 Introduction **1**
1.1 Background **1**
1.2 Outline of thesis **2**
1.3 Photocatalysis **3**
1.3.1 Photocatalytic water splitting 3
1.3.2 Requirements for the photo-electrode of semiconductors 4
1.3.3 Surface Pourbaix diagram 6
1.3.4 Oxygen evolution reaction (OER) 7
1.3.5 Photocatalysts for oxygen evolution 10
1.4 Oxynitride materials **10**
1.4.1 Introduction for metal oxynitrides 10
1.4.2 Perovskite oxynitrides 11
1.4.3 Tin based oxynitrides 13
1.5 Strategies for enhancing OER performance **13**
1.5.1 Strain 13
1.5.2 Doping 15
1.5.3 Ferroelectric polarization 15
1.5.4 Anion ordering 16

1.5.5 Other strategies 17

Chapter 2 Methodology 18

2.1 Schrödinger equation 18

2.2 Density functional theory 20

2.2.1 Thomas-Fermi model 20

2.2.2 The theorems of Hohenberg and Kohn 20

2.2.3 The Kohn-Sham equations 21

2.2.4 Exchange correlation functionals 22

2.3 Implementations 24

2.4 Surface energy calculation 25

2.5 OER mechanism 25

Chapter 3 Anion Ordering, Strain, and Doping Engineering of the OER in $BaTaO_2N$ 27

3.1 Introduction 27

3.2 Computational details 29

3.3 Results and discussion 30

3.3.1 Structure of $BaTaO_2N$ 30

3.3.2 TaO_2N-terminated (100) surface 32

3.3.3 TaON-terminated (001) surface 37

3.4 Summary 39

Chapter 4 Enhancing OER by using switchable polarization in ferroelectric $InSnO_2N$ 40

4.1 Introduction 40

4.2 Computational details 42

4.3 Results and discussion 43

4.3.1 Structure and properties of $InSnO_2N$ 43
4.3.2 OER on the SnN-terminated surface 47
4.3.3 Effect of polarization switching on OER 52
4.4 Summary 54
Chapter 5 Conclusion and Outlook **56**
5.1 Conclusion 56
5.2 Outlook 57
Reference **58**
Appendix **79**
Paper1 ..... **79**
Paper2 ..... **94**

Chapter 1
Introduction

In this chapter, an overview of the oxynitride-based materials in the applications of photocatalytic water splitting is provied. First, the outline of this thesis is presented. Then, the principles of the photocatalytic water splitting and OER are introduced. Besides, the properties of oxynitride materials are summarized, especially perovskite oxynitrides and tin based oxynitrides. Finally, the methods to improve the performance of OER are discussed.

1.1 Background

The dependence on technology, the improvement of living standards in developed countries and the increasing population of developing countries undoubtedly lead to an increase in the demand for energy. In order to meet the requirements of rapid growth in energy consumption, the consumption of fossil fuels is increasing quickly, which will cause increased ozone depletion, climate changes, environmental problems, and health risks to living creatures on the earth. What's more, fossil fuels have limited reserves on the earth and are non-renewable resources.[1] Therefore, it is essential to make use of the renewable energy sources to gradually replace the fossil fuels.

There are various types of renewable energy sources, such as solar energy, wind energy hydro energy, marine energy, geothermal energy and biomass energy.[2] It is known that hydrogen not only has a high calorific value (143 MJ/kg)[3] but also produces clean emissions. Through the photoelectrochemical (PEC) water splitting process, water and sunlight can be directly used as the main resources to produce hydrogen and oxygen. The application of this technology enables people to utilize the most abundant resources on the earth, water and solar radiation, at low cost. Hence, PEC water splitting is a protracted strategy for solar energy conversion into hydrogen fuel to achieve the sustainability of social clean energy and environment. In 1972, Fujishima and Honda

reported pioneering research on water splitting on TiO_2 electrodes, which has inspired people's interest in this technology.[4] Since then, a vast amount of studies have been conducted in developing semiconductor photocatalysis, and extensive work has been done to improve the efficiency of photocatalysts.[5–7] In spite of years of researches on PEC solar energy conversion, the conversion efficiency of light to hydrogen fuel is still far from the maximum theoretical efficiency. This means that it is still critical to have an in-depth understanding of some key aspects of the PEC solar-to-hydrogen conversion process for further enhancing of the conversion efficiency.

1.2 Outline of thesis

This thesis includes five chapters. The chapters are outlined as follows:

Chapter 1: Introduction

An overview of the oxynitride-based materials in the applications of photocatalytic water splitting is presented. The methods to improve the performance of OER are also discussed.

Chapter 2: Methodology

A brief introduction to the DFT and its implementations is given.

Chapter 3: Anion ordering, strain, and doping engineering of the OER in $BaTaO_2N$

The role of anion ordering, strain, and doping modifications on the OER for different surfaces of $BaTaO_2N$ has been investigated. Paper 1 is the main part of this chapter and also included in the Appendix.

Chapter 4: Enhancing OER by using switchable polarization in ferroelectric $InSnO_2N$

The OER performance of $InSnO_2N$ surfaces with negatively/positively polarized bulk has been studied. For a given surface, switching of the polarization direction is presented to optimize the adsorption strength for intermediates along the OER pathways and hence enhance the OER activitiy. Paper 2 is the main part of this chapter and also included in the Appendix.

Chapter 5: Conclusion and outlook

The main findings from this project and outlook are summarized.

1.3 Photocatalysis

1.3.1 Photocatalytic water splitting

The term photocatalysis can be traced back nearly 100 years[8,9], which is generally defined as the acceleration of a photochemical reaction by adding a catalyst that is not consumed in the reaction.[10] The catalyst here can absorb light to produce the electron-hole pairs and promote chemical reaction.

In the water splitting chemical reaction, water is broken down to produce hydrogen and oxygen, which is a non-spontaneous reaction. There are different power sources that can be used to break the H-O bonds, like thermal (heat), electrical (current), or light (electromagnetic radiation), which corresponds to thermolysis, electrolysis, or photolysis. For the thermal or thermochemical water splitting, high temperatures (500-2000 °C)[11] is needed to drive the water splitting reaction. When the water splitting process is driven by applying electricity, it is the electrolytic water splitting, in which the electrical energy is converted to the chemical energy at the electrode-solution interface via charge-transfer reaction. Photocatalytic water splitting is another technology, by which the solar energy is used to split the water into hydrogen and oxygen. This technology is an effective route for converting solar energy into clean and renewable hydrogen fuel, and it plays a critical role in solving the energy crisis and environmental problem.

The solar water splitting can be generally divided as two systems, photocatalytic and PEC water splitting. Photocatalytic water splitting usually uses the semiconductor powder as the photocatalyst (Figure 1.1a). When the photocatalyst is dispersed into the solution under the sunlight irradiation, the formation of hydrogen and oxygen will be detected. The general photocatalytic water splitting is involved three steps: photon absorption and electron-hole pair generation; migration of photon-induced carriers to surface; and surface chemical reactions. When the photocatalyst absorbs photons with the energy higher than the band gap of the semiconductor, the electrons are effectively excited from the valence band (VB) to the conduction band (CB) while holes are left in the VB. Then photo-generated electron-hole (e-h) pairs migrate to the photocatalyst surface to take part in the chemical reaction. During this step, some charge carriers (electrons and holes) will recombine, which is undesirable for the photocatalystic water splitting. Various efforts have been carried out to reduce the recombination of the carriers. In the last step, the

photo-excited carriers will react with water on the active surface sites of the photocatalyst, where the water is reduced to hydrogen by electrons and oxidized to oxygen by holes. However, it is a challenge to separate the mixed H_2 and O_2 in the photocatalytic reaction system. This could be overcome by using PEC water splitting system.

The PEC water splitting system combines the energy of solar light and electricity, which is composed of a photoelectrode and a metal electrode immersed in the aqueous electrolyte and is connected by an externally applied circuit voltage (Figure 1.1b). Similar to photocatalytic water splitting, after absorbing photons, for the photoelectrode, electrons will be excited to the CB and holes will remain in the VB. Then the electrons are transported to the metal electrode and participate in the hydrogen evolution reaction (HER) to produce H_2 gas. At the same time, at the surface of the photoelectrode, holes participate in the OER generating the O_2 gas. Therefore, the H_2 and O_2 gas products are separated.

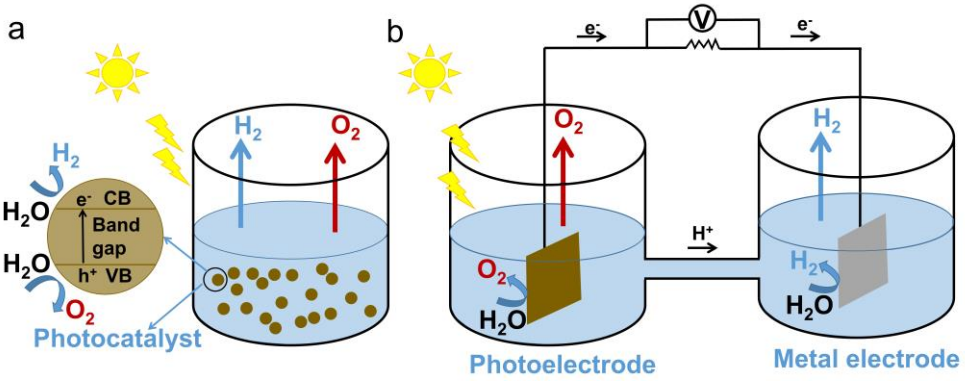

Figure 1.1. Schematic illustration of solar water splitting: (a) photocatalytic water splitting system and (b) PEC water splitting system.

1.3.2 Requirements for the photo-electrode of semiconductors

In the semiconductor-based PEC water splitting, the requirements for the photo-electrode must be met before the water splitting reaction can proceed.

The band gap of the photo-electrode will influence the light harvesting ability, because the photo-electrode only absorbs photons with energy larger than its band gap.

Thermodynamically, free-energy change of the water splitting reaction ($2H_2O \rightarrow O_2 + 2H_2$) is 4.92 eV.[12] Since it is a four-electron process, at least energy of 1.23 eV should be provided from the electron-hole pair for the reaction. However, excess energies should be taken into account. These excess energies include the kinetic and thermodynamic losses. The thermodynamic losses is caused by the second law of thermodynamics. The kinetic losses is due to the non-ideal factors in the conversion process like the overpotentials at electrode, resistive drop at the electrolyte and so on. Therefore, the band gap of the photo-electrode should be large enough to generate the electron-hole carriers to drive the chemical reaction. As the same time, to harvest as much the solar spectrum as possible, the band gap value cannot be too large. Hence, in order to obtain the maximum photon to chemical conversion efficiency, the material used as the photoelectrode in the PEC water splitting system should have a band gap energy of 2.0 – 2.25 eV.[13]

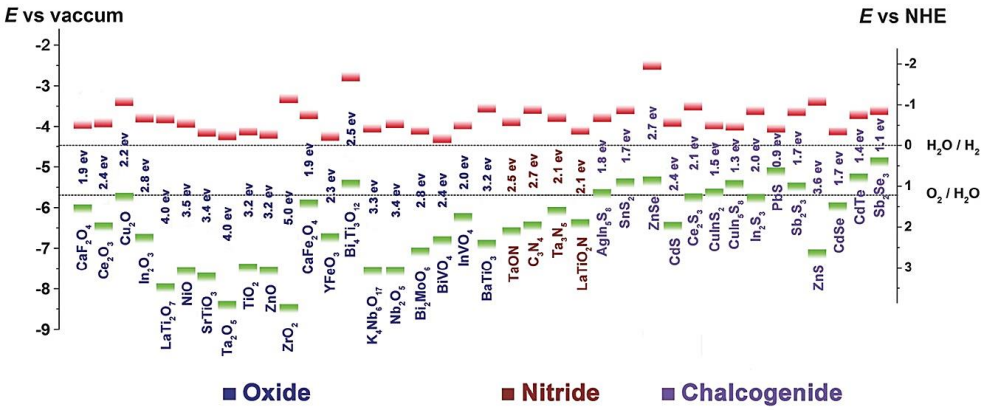

Figure 1.2. Band-edge positions of semiconductors *vs* NHE and vaccum level. The redox potentials for water splitting are shown in dotted lines. Reproduced with permission.[14] Copyright 2015, John Wiley and Sons.

Another requirement is band-edge positions, which is related to the potentials of the generated charge carriers. For the PEC water splitting system, the potential of photogenerated holes is determined by the VB edge of semiconductor. As shown in Figure 1.2, on the one hand, for photo-electrode, VB edge potential *vs* NHE should be more positive than the water oxidation level to drive the oxidation reaction. On the other hand,

only the bottom level of the CB is more negative than the reduction potential of H^+/H_2, the photogenerated electrons with a potential given by the energy of the CB could be used to drive the reduction of protons.

Overpotential is the extra potential for the electrode to drive the reaction on the surface which is the kinetic requirement. The overpotential is particularly important for the placement of the semiconductor's band-edge positions relative to the potentials for the OER and HER, respectively. Taking the overpotential into consideration, if the potential of VB is not positive enough for water oxidation or the potential of the CB is not sufficiently negative for the reduction of protons, the rate of water splitting will be greatly reduced.[13] More details on theory calculation for overpotential will be discussed in section 2.5.

1.3.3 Surface Pourbaix diagram

The surface phase diagram can be constructed in the PEC water splitting system, which shows the stability of the surface that adsorbs the reaction fragments under different values of pH and potential (Figure 1.3).[15,16] This kind of surface phase diagram is called Pourbaix diagram[17,18] that was originally used to describe the bulk transitions.[19] It has been shown that the Pourbaix diagram can accurately demonstrate which the surface

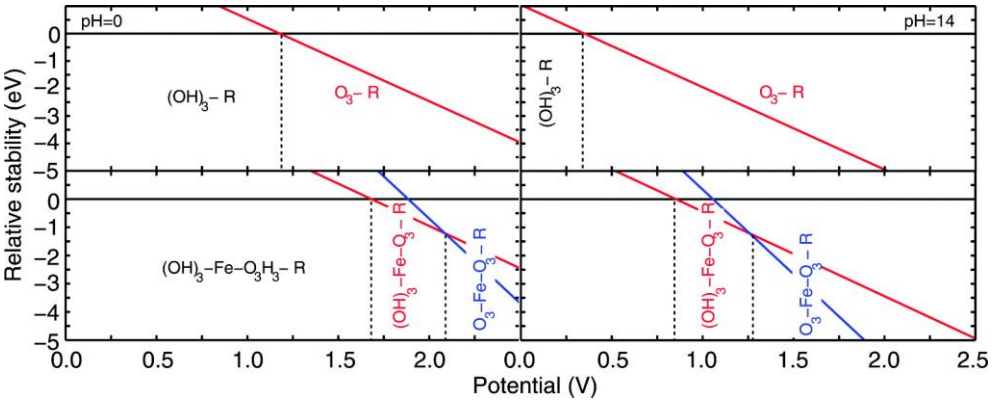

Figure 1.3. The relative stability of surfaces as a function of applied potential at pH = 0 and pH = 14, respectively. Reproduced with permission.[16] Copyright 2011, American Chemical Society.

structure is stable under electrochemical condition by theoretical studies.[16,18,20] The relationship among materials' phase stability, the electrode potential and pH can be described by the Pourbaix diagram. Therefore, the surface Pourbaix diagram has been widely applied in the PEC water splitting system to thermodynamically describe materials' phase stability in an aqueous electrochemical environment

1.3.4 Oxygen evolution reaction (OER)

As a four-electron process, compared with the evolution of hydrogen, the oxygen evolution has received more research attention due to the high overpotential and complex reaction mechanism. Various OER mechanisms have been proposed and discussed, and some of them can be seen in Figure 1.4, while none of them has been fully validated from the experimental study. Kinetic models for OER (Figure 1.4I-III)[21] were proposed by Bockris, who demonstrated that within a specific reaction mechanism the rate determining step can determine the Tafel slope that can be measured in an experiment. However, only based on the Tafel slope, a rate determining step cannot be clearly identified. Moreover, the actual reaction mechanism may not have been taken into consideration in the group of mechanisms for deriving the Tafel slope. Furthermore, in addition to the electrocatalytic reactions, other factors sometimes can also alter the Tafel slope.[22] Therefore, precise knowledge about properties of the electrodes materials is required to get a valid mechanistic insight by analyzing the Tafel slope.

On the basis of the electrochemical framework, Nørskov and co-workers proposed a theoretical framework (see Figure 1.4IV) in which the photooxidation of water can be described from the thermochemical analysis by first-principle calculations.[12] Within this mechanism, for each reaction, the Gibbs free energy is computed as a function of electrode potential. As shown in Figure 1.5, the Gibbs free energy of each reaction less than 0 $J \cdot mol^{-1}$ is a necessary condition for the proceeding of the overall reaction. Although the sum of Gibbs free energy of the four reaction steps is equal to the Gibbs free energy of the overall water splitting reaction, the Gibbs free energy of each reaction step can be different. The Gibbs free energy of every step alters equally with electrode potential when one electron is exchanged in each step. Thus, the highest electrode potential is needed for the reaction with the largest Gibbs free energy to be downhill and this reaction step is the potential determining step. For example, in Figure 1.5, Gibbs free energy of step 3 to be downhill

I) Oxide Path		II) Electrochemical Oxide Path	
1)	$H_2O + M \rightarrow M\text{-}OH + H^+ + e^-$	1)	$H_2O + M \rightarrow M\text{-}OH + H^+ + e^-$
2)	$2\,M\text{-}OH \rightarrow M\text{-}O + M + H_2O$	2)	$M\text{-}OH \rightarrow M\text{-}O + H^+ + e^-$
3)	$2\,M\text{-}O \rightarrow 2\,M + O_2$	3)	$2\,M\text{-}O \rightarrow 2\,M + O_2$
III) Electrochemical Metal Peroxide Path		**IV) DFT-predicted Peroxide Path**	
1)	$H_2O + M \rightarrow M\text{-}OH + H^+ + e^-$	1)	$H_2O + M \rightarrow M\text{-}OH + H^+ + e^-$
2)	$2\,M\text{-}OH \rightarrow M\text{-}O + M + H_2O$	2)	$M\text{-}OH \rightarrow M\text{-}O + H^+ + e^-$
3)	$M\text{-}O + H_2O \rightarrow M\text{-}OOH + H^+ + e^-$	3)	$M\text{-}O + H_2O \rightarrow M\text{-}OOH + H^+ + e^-$
4)	$2\,M\text{-}OOH \rightarrow M\text{-}O + H_2O + O_2 + M$	4)	$M\text{-}OOH \rightarrow M + O_2 + H^+ + e^-$

Figure 1.4. The proposed mechanisms of OER.[23,24] M is a surface active site. Reproduced with permission.[25] Copyright 2016, John Wiley and Sons.

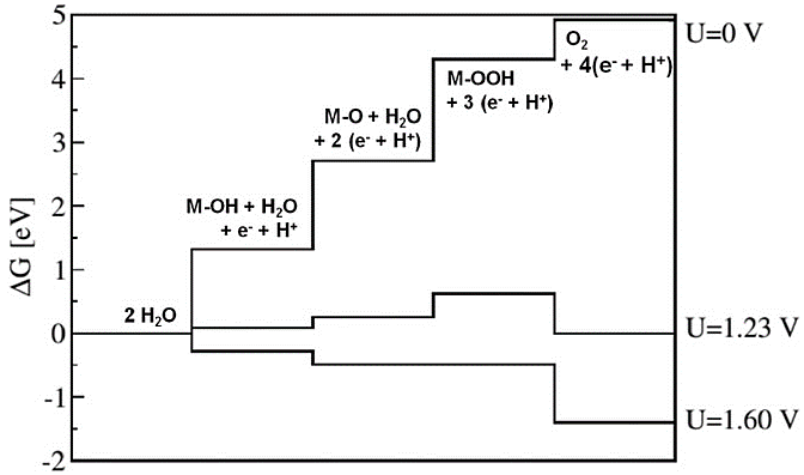

Figure 1.5. Gibbs free energies diagram for RuO_2 (110) surface. The overall reaction has equilibrium potential of 1.23 V *vs* SHE.[24] Reproduced with permission.[25] Copyright 2016, John Wiley and Sons.

requires potential of 1.60 V. Gibbs free energy of the reaction step is dependent on the adsorption energy of the intermediates, which relies on the catalyst. Hence, the potential required to promote the overall reaction is also dependent on the catalyst.[25] The reactivity

trend of the catalyst is described very well using this method, which makes this mechanism reasonable, although thermodynamics are considered alone in this model without taking any kinetic barrier into consideration. This treatment does not represent no kinetic barriers exists, but assuming that the kinetic barriers are proportional to the thermodynamic barriers, and thus based on thermodynamics the trend of reactivity can be qualitatively explained.

Overpotential is the bias between the actual voltage applied to the electrode and the thermodynamic reversible potential of OER in the electrocatalyst, which is a key parameter for comparing performance of different OER activities. According to the DFT calculations, the general scaling relationship between the binding energy of OH* and OOH* has been determined for the studied oxide materials.[26] Based on the computational standard hydrogen electrode (SHE) model, the theoretical overpotentials were estimated by using DFT calculation, and the trends of calculated theoretical overpotentials are in consistent with the experimental results.[26] Therefore, the calculated theoretical overpotential can be used to characterize the OER activities. The OER volcano plots for different kind of materials are shown in Figure 1.6, and there is an upper limit for the OER activities with the lowest overpotential.

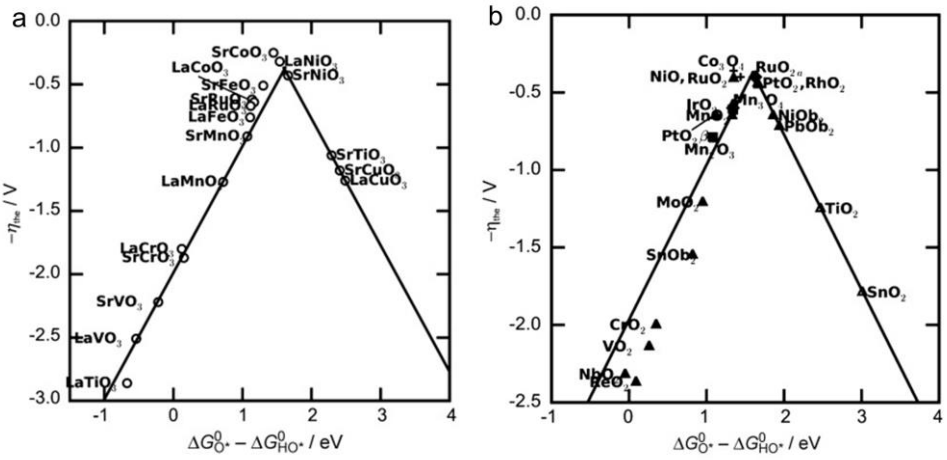

Figure 1.6. OER volcano plots for (a) perovskites and (b) binary oxides. Reproduced with permission.[26] Copyright 2011, John Wiley and Sons.

1.3.5 Photocatalysts for oxygen evolution

Based on different structures, compositions and morphologies, there are diverse kinds of photocatalysts for oxygen evolution. In 1972, titanium dioxide (TiO_2) firstly was found as photoelectrode that can decompose water into H_2 and O_2,[4] which has attracted widespread attention. There are four mainly phases for TiO_2: TiO_2 (B), brookite, anatase and rutile. The structures of these four phases are composed of TiO_6 octahedron with different distortion of the octahedron. Because of the low physicochemical stability of the other two phases, the study of photocatalysts of TiO_2 mainly focus on anatase and rutile. The anatase TiO_2 usually exhibits a better photocatalytic performance than the rutile TiO_2, because there are more oxygen vacancies in anatase TiO_2 causing the band bend to trap electrons and promote charge separation.[27,28] Bismuth vanadate ($BiVO_4$) is also a promising photocatalytic material on account of the ideal band gap of 2.4 eV for the monoclinic phase and suitable VB edge position for oxygen evolution.[29] The photocatalytic activities on different exposed facets of $BiVO_4$ have also been investigated, and a higher photocatalytic oxygen evolution rate has been found for $BiVO_4$ with 30 facets.[30] Besides, it is found that the morphology of $BiVO_4$ can be optimized by controlling the pH value in the synthesis process, which suggests an effective approach to boost the O_2 production activity.[31] Tungsten trioxide (WO_3) has band gap in the range of 2.5-2.8 eV and the suitable VB edge position for oxygen evolution.[32,33] Hence, it has been widely studied as photo(electro)catalyst for water oxidation in term of its morphology regulation,[34–36] exposing facets,[37] and the particle size.[38] Among various iron oxides, as photocatalyst, the hematite Fe_2O_3 (α-Fe_2O_3) has several advantages, such as narrow band gap (1.9-2.2 eV), high stability and plenteous natural resources.[39,40] Since the oxygen evolution activities closely depend on the morphology of α-Fe_2O_3, a lot of investigations on microstructure regulation of α-Fe_2O_3 have been carried out to promote O_2 evolution performance.[33,41–44]

1.4 Oxynitride materials

1.4.1 Introduction for metal oxynitrides

Metal oxynitrides, as an important type of emerging materials, have recently been intensively investigated. Because electronegativity, polarizability and anion charge of nitrogen are different from oxygen, it is possible to turn the properties of oxides by

introducing nitrogen. Due to the less electronegativity and more polarizability of nitrogen, the covalency of metal-nitrogen bond is higher than that of metal-oxygen bond, which results in an increase of nephelauxetic effect, a decrease of the electronic repulsion and a decrease energy of the d orbitals.[45] Besides, because of the higher nitride charge, the crystal field splitting is larger compared with oxides and it is likely to form new compounds with higher cationic oxidation states. Additionally, the introduction of the nitrogen reduces the band gap, and hence makes this type of materials promising for applications as photocatalyst. The oxynitrides with new magnetic, dielectric and conduction properties also have been observed, which enriches the applications of such materials in other fields.[46–50]

1.4.2 Perovskite oxynitrides

Perovskite oxynitrides belong to the family of perovskite and their structures are similar to perovskite oxides. Hence we will introduce perovskite oxides firstly. Perovskite oxides, derived from $CaTiO_3$, have been extensively investigated in various photocatalytic applications due to their various compositions, tunable structures, high stability and outstanding photocatalytic performance. $CaTiO_3$ with mineral form was discovered in 1839, and it is called as "perovskite" to commemorate the famous Russian mineralogist Lev Aleksevich von Perovski.[51] Recently, several perovskites have been discovered, constituting a large family of materials with ABO_3-type structure. In the ABO_3-type structure, the radius of cation A^{2+} is larger than B^{4+}. There is a huge family of the perovskite oxides because the A and B sites elements can be adjusted from the periodic table.[52] Figure 1.7a shows the ideal ABO_3 perovskite oxides structure with cubic symmetry, in which the A-site cations are in 12-fold coordination and B-site cations are in 6-fold octahedral coordination. In addition, the different ionic radii from different constituting cations result in the lattice distortion, which causes the lower symmetry of the perovskite to orthogonal, tetragonal, monoclinic, rhombohedral, and triclinic structures.[53,54]

The substitution of the oxygen with nitrogen in perovskite oxides forms perovskite oxynitrides. It is assumed that the distribution of nitrogen is random and there are two possible anion orderings in the BO_4N_2 octahedron, as shown in Figure 1.7 b. In the BO_4N_2 octahedron, when the N-B-N angle is 90°, it corresponds to the cis-N–B–N connections, and when the N-B-N angle is 180°, it corresponds to the trans-N–B–N connections.

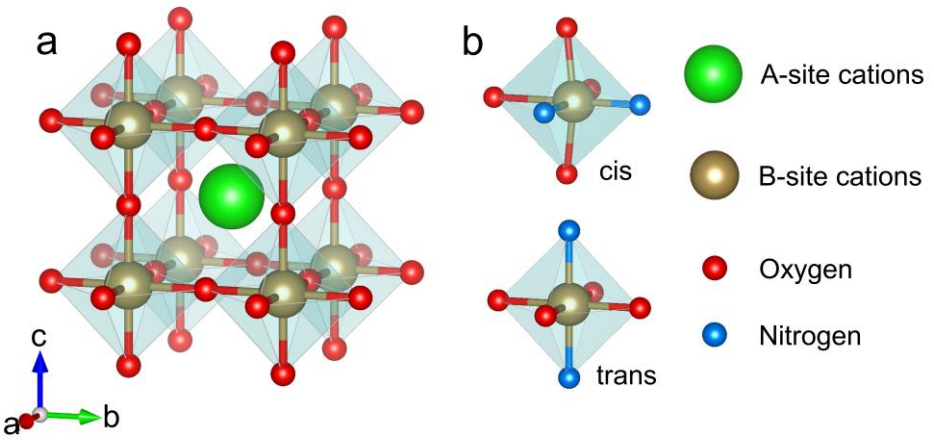

Figure 1.7. Schematic illustration of the (a) ABO_3 perovskite oxides with ideal cubic structure and (b) BO_4N_2 mixed-anion octahedron with cis/trans anion orders.

R. Marchand et al first reported perovskite oxynitrides with the general formula $ABO_{2-x}N_{1+x}$.[55] The introduction of nitrogen in traditional cubic ABO_3 perovskite, the nitrogen content is as high as 2.16 atoms per formula for the perovskite oxynitrides (A = La and B = W).[56] In addition to the nitrogen content, the importance of anion order also cannot be ignored. The local cis arrangement has been determined for the $SrTaO_2N$, $SrNbO_2N$ and RVO_2N (R = La, Pr, Nd) using neutron and electron diffraction.[57–59] The local cis order for $BaTaO_2N$ has also been investigated via both experimental and theory studies.[60–63]

Another perovskite structure, Ruddlesden-Popper oxynitrides, has also been reported to show specific properties. The family of $(SrO)(SrNbO_{2-x}N)_n$ (n = 1, 2), as Ruddlesden-Popper oxynitrides, obtains various oxidation states and transport properties from their layered structures.[64] It has been found that in the layered K_2NiF_4-type-structure Sr_2TaO_3N and Sr_2NbO_3N, the nitrogen atoms are located at the equatorial positions of the octahedron, which have larger total bond strength, being consistent with Pauling's second crystal rule.[65–67]

Lastly, the photocatalytic application of the perovskite oxynitrides will be discussed. In 2002, it was first reported that $LaTiO_2N$, a typical perovskite oxynitrides, was used as

photocatalyst to split water into H_2 and O_2.[68] In addition to titanium perovskite oxynitrides, tantalum perovskites oxynitride, $ATaO_2N$ (A=Ca, Sr and Ba) and $PrTaON_2$ are also potential visible-light-driven candidates of photocatalyst for water splitting. Because their band gaps (1.5-2.5 eV) are smaller than that of TiO_2, and they are stable in aqueous solutions. Moreover, the existence of tantalum provides the possibility of high efficiency, since many photocatalysts with the highest quantum efficiency have tantalum.[69] Niobium perovskite oxynitrides, $ANb(O,N)_3$ (A = Ca, Sr, Ba, and La), have also been reported as promising candidates as water-splitting photocatalysts because of their wide range of visible-light adsorption ability. As the electronegativity of Nb is higher than that of Ta and the CB constituted by the empty Nb-4d orbitals is lower compared to CB formed by Ta-5d, the band gap energies of niobium perovskite oxynitrides are smaller than that of the corresponding Ta-based similar oxynitrides.[70–73]

1.4.3 Tin based oxynitrides

The hexagonal manganite (h-$RMnO_3$, R= Sc, Y, Ho, Er, Tm, Yb and Lu) is the extensively investigated family of multiferroics.[74] Among them, $LuMnO_3$ shows the highest stability, due to the increasing of the thermodynamic stability of h-$RMnO_3$ with decreasing radius of the R cation.[75,76] The crystal structure of $P6_3cm$ phase of h-$LuMnO_3$ is composed by corner-sharing MnO_5 bipyramids which form layers separated by Lu ions, as shown in Figure 1.8a.

A new family of Sn oxynitrides, formula $ASnO_2N$ (A=Y, Eu, La, In and Sc), has been predicted to be ferroelectric semiconductor. The structure of the Sn oxynitrides is shown in Figure 1.8b, which adopts $P6_3cm$ phase of h-$LuMnO_3$ and oxygen in the bipyramids is replaced by introducing nitrogen. Adopting the polar h-$LuMnO_3$ structure, these Sn oxynitrides have sizable spontaneous polarization and the predicted values of band gap range from 1.6 to 3.3 eV, which make them potential applications in photovoltaic, photocatalystic and optoelectronic fields.[77]

1.5 Strategies for enhancing OER performance

1.5.1 Strain

For the last decades, researchers have been working on improving the OER performance by applying various approaches. It has been reported that the binding energy between

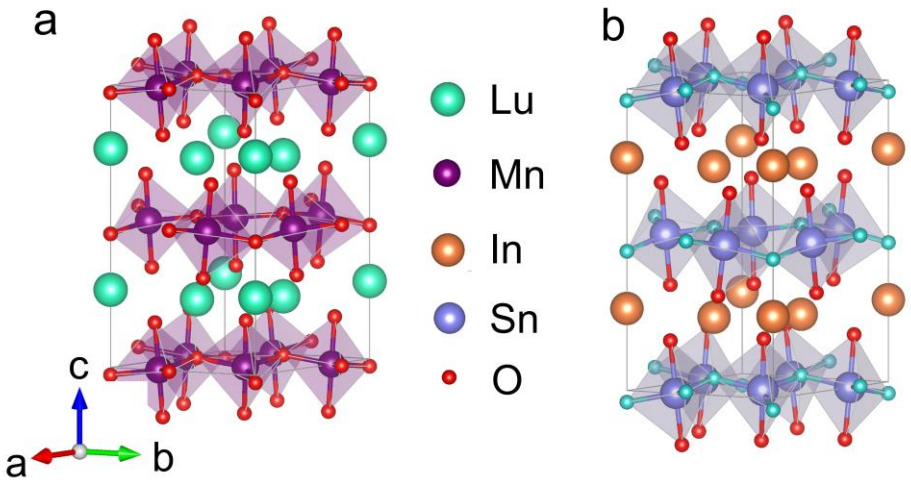

Figure 1.8. The crystal structure of (a) h-$LuMnO_3$ with the ferroelectric $P6_3cm$ phase and (b) $InSnO_2N$ with the ferroelectric $P6_3cm$ phase.

molecular and surface of catalyst can be altered by strain engineering, which further influences the OER activities. For instance, Shao-Horn and co-workers have found that the OER activity of $LaCoO_3$ is enhanced by applying the moderate tensile strain to optimize the orbital filling.[78] The strain-engineering effect on the OER performance of $LaNiO_3$ has also been investigated, where the strain degree from -2.2% to 2.7% was applied to study the OER activity. And the researchers have found that the OER activity can be enhanced when applying the moderate compressive strain that weakens M-O bonding.[79]

The strain can also modulate the OER activities by affecting the d-band electronic structure of catalyst. The d-band electronic structure of the OER catalysts proposed by Norskov et al is an important parameter to describe the catalyst activity.[80] Generally, when the catalyst is under tensile strain, the d-band center will move upward. On the contrary, compressive strain will make the d-band center move down,[81] which is in agreement with the original d-band center theory put forward by Nørskov et al. As reported in a compressive-stress modulation of Ru monoatomic OER case, a variety of

stresses of Ru are generated by the PtCu substrate, which causes Ru d-band center to move gradually. Then an optimized position of the d-band center has been found with an optimal OER activity.[82]

1.5.2 Doping

The OER activity of the water splitting is influenced by the interactions between the adsorbed fragments and the active sites.[83] Each step in the multistep OER process is related to the adsorption energy of the intermediates on active sites. Volcano plot has been used to describe the relationship between the OER activity and the adsorption strength, which shows that a too weak or too strong adsorption strength is not conducive to OER performance.[84,85] According to this, the elemental doping can be applied to modulate the surface structure and electronic structure, and hence regulate the adsorption energy between the active sites and fragments, which is a commonly used strategy to increase OER performance. For example, it has been reported that in the Ni/Co (oxy)hydroxides, Fe-doping dramatically enhances OER activity by providing more active sites.[86–88] Co and Ni doped hematite surfaces have been theoretically predicted to have the minimum overpotential among all considered dopants (Ti, Mn, Co, Ni, Si),[89] which is further validated by the experimental results.[90]

The introduction of new element also can induce lattice strain and thus affects the OER performance. For instance, in the study of B-site ions' doped $SrCoO_{3-\delta}$, it it found that larger iron doping leads to lattice distortion and lattice strain. This turning of the structure influences the stability and performance of the oxide as an OER electrocatalyst.[91]

1.5.3 Ferroelectric polarization

During the photocatalytic water splitting process, it takes hundreds of picoseconds for carriers migration while it only takes several picoseconds for the carrier recombination in bulk much faster than the carrier transportation.[5] Polarization electric field can be used to promote charges separation and hence enhance photocatalytic performance. Some ferroelectric materials with spontaneous polarization have been demonstrated to show a better photocatalytic performance. For instance, under simulated light, compared to paraelectric $BaTiO_3$, Rhodamine B (RhB) decolorization performance of the ferroelectric $BaTiO_3$ increases by three times.[92]

In addition, the polarization can also influence the molecular adsorption,[93] and the surface reaction.[94,95] It has been shown that compared to unsupported TiO_2, the OER performance for heterostructures of TiO_2 on a polar substrate is significantly improved due to dynamical induced dipoles.[96] Moreover, as described by the Sabatier principle, if the interaction between the adsorbate and the catalyst is too weak, the reagent will not be able to bind to the catalyst, and if this interaction is too strong, the reaction product will fail to be desorbed. Hence, there is a trade-off, that is, the strength of the adsorption between the reagent and the surface is as strong as possible, and the adsorption between the product and the surface is as weak as possible. This compromise will fundamentally lead to limited catalytic activity. The relationship between the catalytic activity of various catalytic surfaces and the strength of molecular adsorption can be shown as a volcano diagram similar to Figure 1.6. The strength of adsorption between the catalyst and the intermediate largely depends on the surface electronic state. If there is a single surface whose activity is adjustable from strong binding of reagent to weak binding of product, through external control, then the limitation of the Sabatier principle can be overcome. One possibility is the using of the ferroelectric materials whose surface electric properties is tunable via switching the polarization direction. So far, this approach has been applied in various reactions to improve the surface chemistry and the catalytic activity. For example, the CrO_2 monolayer on ferroelectric $PbTiO_3$ is allowed to directly decompose NO_x and oxidize CO while avoiding oxygen and sulfur poisoning.[94] Recently, some DFT calculations have shown that the fundamental limitations on catalytic efficiency from Sabatier principle can be overcome by switching the out-of-plane polarization directions for the ferroelectric materials.[94,97]

1.5.4 Anion ordering

In the past decades, transition metal oxynitrides, especially the perovskite oxynitrides, as photocatalyst have attracted much attention due to their suitable band gaps.[98,99] Recently, it has been found that the anion arrangements of N^{3-} and O^{2-} in the perovskite-oxynitride crystals are controllable, which can be used to modify the electronic features of the material.[100] The relationship between the anion orderings and electronic features in $CaTaO_2N$ has been studied, which shows that the band gaps of $CaTaO_2N$ with different order of anions are significantly different. Since the structures with three dimensional

anion orderings have more positive valence band maximum relative to two-dimensional ones, it is recommended that they are more suitable for the OER.[101]

1.5.5 Other strategies

In addition to the above mentioned strategies to improve the oxygen evolution performance of photocatalyst, other methods such as the formation of oxygen vacancies, fabrication of special microstructures and surface modification can also effectively promote the OER activity. Oxygen vacancies on the surface can boost the separation of the photogenerated carriers.[102] For instance, for the BiOCl nanosheets, it is found that the surface of (010) with the dissociatively adsorbed water on the oxygen vacancies shows a higher oxidation tendency than the (001) surface with molecularly adsorbed water on the oxygen vacancies, which results in an enhanced oxygen evolution performance.[103] Since the special morphology of the photocatalyst often brings the advantages like larger specific surface area, more favorable visible light absorption and faster migration of photogenerated carriers, a variety of methods have been carried out to fabricate the photocatalysts with special morphology. By the two-phase approach, the unique conical shape of $BiVO_4$ was obtained and it shows a higher oxygen evolution rate than that of the $BiVO_4$ nanosheets.[104] The surface medication like hydrogenation treatment has also been studied. The O_2 evolution rate of hydrogenated WO_3 is about two times higher than the pristine WO_3.[105]

Chapter 2

Methodology

In this chapter, a brief introduction on DFT and simulation methods is given. Firstly, we briefly introduce the Schrödinger equation, Born-Oppenheimer approximation and Hartree-Fock approximation. Then, the DFT is discussed, like Thomas-Fermi model, the theorems of Hohenberg, the Kohn-Sham equations and Exchange Correlation Functionals. At the end of this chapter, we simply present the simulation methods used in this project.

2.1 Schrödinger equation

The time-independent, nonrelativistic Schrödinger equation

$$\hat{H}\Psi(\vec{r},\vec{R}) = E\Psi(\vec{r},\vec{R}) \tag{2-1}$$

Where $\vec{r}$ is the set of all electrons coordinates $\{\vec{r}\}$ and $\vec{R}$ is the set of all nuclei coordinates $\{\vec{R}\}$. E is energy eigenvalue and Ψ is wave function. The Hamiltonian operator $\hat{H}$ is composed of the kinetic energy and interaction energy of the particles (electrons and nuclei).

$$\hat{H} = \hat{H}_e + \hat{H}_N + \hat{H}_{e-N} \tag{2-2}$$

And

$$\hat{H}_e(\vec{r}) = \hat{T}_e(\vec{r}) + \hat{V}_e(\vec{r}) = -\sum_i \frac{\hbar^2}{2m}\nabla_{r_i}^2 + \frac{1}{2}\sum_{i,i'}\frac{e^2}{|\vec{r}_i - \vec{r}_{i'}|} \tag{2-3}$$

$$\hat{H}_N(\vec{R}) = \hat{T}_N(\vec{R}) + \hat{V}_N(\vec{R}) = -\sum_j \frac{\hbar^2}{2M_j}\nabla_{R_j}^2 + \frac{1}{2}\sum_{j,j'}\frac{Z_j Z_{j'} e^2}{|\vec{R}_j - \vec{R}_{j'}|} \tag{2-4}$$

$$\hat{H}_{e-N}(\vec{r},\vec{R}) = \hat{V}(\vec{r},\vec{R}) = -\frac{1}{2}\sum_{i,j}\frac{Z_j e^2}{|\vec{r}_i - \vec{R}_j|} \tag{2-5}$$

here, in equation (2-3), $\hat{H}_e(\vec{r})$ represents the kinetic and interaction energy of the electrons. In equation (2-4), the energy of nuclei $\hat{H}_N(\vec{R})$ is composed of the kinetic energy of the nuclei

and the nucleus-nucleus interaction. In equation (2-5), $\hat{H}_{e-N}(\vec{r},\vec{R})$ represents the nuclei-electrons attractive electrostatic interaction.

Notice that the number of electrons is considerably larger than the number of nuclei. For example, there are about 5 x 10^{22} nuclei and 7 x 10^{23} electrons per cubic centimeter of Si. Thus solving the Schödinger equation for practical materials is very complicated and impracticable. Several approximations have been developed to simplify the solution of the Schödinger equation.

To simplify the Schödinger equation of many-body system, due to large weight difference between the nucleus and electron, the nuclei and electrons can be regarded as two independent subsystems, and the movement of electrons in the actual system can be separated from the movement of the nuclei. This is the Born-Oppenheimer approximation, also known as the adiabatic approximation.[106]

Under the Born-Oppenheimer approximation, the solution of the Schödinger equation (2-1) of the many-body system can be written as:

$$\Psi_n(\vec{r},\vec{R}) = \sum_n x_n(\vec{R})\Phi_n(\vec{r},\vec{R}) \tag{2-6}$$

$\Phi_n(\vec{r},\vec{R})$ is the solution of the Schödinger equation $\hat{H}_0(\vec{r},\vec{R})\Phi_n(\vec{r},\vec{R}) = E_n(\vec{R})\Phi_n(\vec{r},\vec{R})$ determined by many-electron Hamiltonian operator $\hat{H}_0 = \hat{H}_e(r) + \hat{V}_N(R) + \hat{H}_{e-N}(r,R)$. By separating the variables, the Schödinger equation satisfied by the many-electron system can be obtained:

$$\left[-\sum_i \frac{\hbar^2}{2m}\nabla_{r_i}^2 - \frac{1}{2}\sum_{i,j}\frac{Z_j e^2}{|\vec{r}_i - \vec{R}_j|} + \frac{1}{2}\sum_{i,i'}\frac{1}{|\vec{r}_i - \vec{r}_{i'}|}\right]\Phi = \left[-\sum_i \hat{H}_i + \sum_{i,i'}\hat{H}_{ii'}\right]\Phi = E\Phi \tag{2-7}$$

The equation can be simplified into the form described by the single-particle operator $\hat{H}_i$ and the two-particle operator $\hat{H}_{ii'}$. Due to the interaction between electrons $\hat{H}_{ii'}$, it is difficult to solve this equation.

The many-electron Schödinger equation can be simplified to a single-electron effective potential equation by Hartree-Fock approximation, known as single-electron approximation.[107] The Hartree-Fock theory is very accurate for describing atoms and molecules. However, for periodic solids, this method is unrealistic, and the density functional method is more effective.

2.2 Density functional theory

Density functional theory (DFT) as one of the most popular and successful quantum mechanics methods, has been applied for calculating the electronic structure of solids in physics and the binding energy of molecules in chemistry. Although some approximations are required, DFT enables researchers to study surface reactions on atomic level by calculating adsorption energy and electronic structure. Hence, in this thesis, the DFT is the basic theoretical tool to investigate the OER for water splitting on oxynitride photocatalysts.

2.2.1 Thomas-Fermi model

In 1927, Thomas and Fermi proposed Thomas-Fermi (TF) model, the predecessor of DFT. The electron density is used as the variable to replace the wave function, which greatly simplifies the problem from the Hartree-Fock equation.[108] In this model, the exchange and correlate between electrons are not considered. In 1930, Dirac corrected this model by adding the local approximation of exchange interaction,[109] and the total energy of the electronic system can be expressed as:

$$E[\rho(\vec{r})] = C_1 \int \rho(\vec{r})^{\frac{5}{3}} d\vec{r} + \int V(\vec{r})\rho(\vec{r}) d\vec{r} + C_2 \int \rho(\vec{r})^{\frac{4}{3}} d\vec{r} + \frac{1}{2} \iint \frac{\rho(\vec{r})\rho(\vec{r}')}{|\vec{r} - \vec{r}'|} d\vec{r} d\vec{r}' \qquad (2\text{-}8)$$

here, the four items of the right part of the equation are kinetic energy local approximation, external potential energy, exchange-related energy and electrostatic interaction energy between electrons, respectively. The electron density of ground states can be obtained by looking for the lowest energy $E[\rho(\vec{r})]$. However, due to the inaccurate representation of the kinetic energy and exchange energy, this theory has no practical significance for describing the properties of molecules and solids, and has not been widely used.

2.2.2 The theorems of Hohenberg and Kohn

In 1964, Hohenberg and Kohn proposed the theory of inhomogeneous electron gas based on the Thomas-Fermi model and established a strict DFT.[110] The Hohenberg-Kohn (HK) theory contains the following two theorems:

First theorem: The ground state energy of the system is only decided by the electron density.

Second theorem: The ground state energy of a system with an external potential is given by the minimum value of the energy functional and the density that minimizes the energy of the functional corresponds to the ground state density.

From this, the ground-state energy functional of the many-electron system can be given as:

$$E[\rho(\vec{r})] = \int V(\vec{r})\rho(\vec{r})d\vec{r} + T[\rho(\vec{r})] + \frac{1}{2}\iint \frac{\rho(\vec{r})\rho(\vec{r}')}{|\vec{r}-\vec{r}'|}d\vec{r}d\vec{r}' + E_{XC}[\rho(\vec{r})] \tag{2-9}$$

here, the four items of the right part of the equation are external potential energy, electronic kinetic energy, Coulomb repulsion energy between electrons and the exchange-correlation (XC) energy, respectively. The equation only gives the idea of solving the ground state energy of the system theoretically. However, the HK theorems do not provide a practical approach to compute the ground-state energy for a many-electron system because the specific form of the electron density function, kinetic energy functional, and XC energy functional are unknown.

2.2.3 The Kohn-Sham equations

The Kohn-Sham method uses a non-interacting particle kinetic energy functional $T_S[\rho]$ instead of $T[\rho]$, and by assuming it is known, makes use of the single-electron wave function to construct the system electron density:

$$\rho(\vec{r}) = \sum_{i=1}^{N} |\varphi_i(\vec{r})|^2 \tag{2-10}$$

$$T_S[\rho] = \sum_{i=1}^{N} d\vec{r}\varphi_i^*(\vec{r})(-\nabla^2)\varphi_i(\vec{r}) \tag{2-11}$$

The variation of $\rho(\vec{r})$ is used to replace the variation of $\varphi_i(\vec{r})$, and E_i is used to replace Lagrange multiplier.

$$\delta\left\{E[\rho(\vec{r})] - \sum_{i=1}^{N} E_i\left[\int d\vec{r}\varphi_i^*(\vec{r})\varphi_i(\vec{r}) - 1\right]\right\}\Big/\delta\varphi_i(\vec{r}) = 0 \tag{2-12}$$

The effective local potential is:

$$V_{KS}[\rho(\vec{r})] = v(\vec{r}) + \int \frac{\rho(\vec{r}')}{|\vec{r} - \vec{r}'|} d\vec{r}' + \frac{\delta E_{XC}[\rho]}{\delta \rho(\vec{r})} \tag{2-13}$$

The Kohn-Sham equation is:

$$\left[- \nabla^2 + v(\vec{r}) + \int \frac{\rho(\vec{r}')}{|\vec{r} - \vec{r}'|} d\vec{r}' + \frac{\delta E_{XC}[\rho]}{\delta \rho(\vec{r})} \right] \varphi_i(\vec{r}) = E_i \varphi_i(\vec{r}) \tag{2-14}$$

These equations can be solved in a self-consistent manner. In the equation (2-13), the initial guess of the density $\rho(\vec{r})$ is used to determine the effective potential $V_{KS}[\rho(\vec{r})]$. Solving the equation (2-14), the wave functions $\varphi_i(\vec{r})$ can be calculated and a new density is calculated from equation (2-10). The process will iterate until it reaches the self-consistency.

2.2.4 Exchange correlation functionals

In the Kohn-Sham equation, the ground state problem of the many-electron system is reasonably transformed into an effective single-electron form. As XC energy includes unknown items, it is vital to have an approximation of XC functionals to solve the Kohn-Sham equation. Local Density Approximation (LDA)[111] and Generalized Gradient Approximation (GGA)[112] are two widely used approximations.

LDA is the first and easiest way to deal with XC energy. The basic idea of this approximation are: 1) the charge density of a non-uniform electronic system is slowly changing and the whole system can be divided into many small volume units dV(r); 2) the charge density in each small volume unit is approximately considered to be constant, which means that for the inhomogeneous electron gas system, the electron density in each volume only depends on the spatial position r. Therefore, the LDA XC energy is shown as:

$$E_{XC}^{LDA}[\rho] \cong \int \rho(\vec{r}) \varepsilon_{XC}[\rho(\vec{r})] d\vec{r} \tag{2-15}$$

where, $\varepsilon_{XC}[\rho(\vec{r})]$ is the exchange and correlation energy density of a uniform electron gas without electron-electron interaction.

If the spin polarized of electron is taken into consideration the XC energy also is dependent on the spin density of electron. This is the local spin density approximation (LSDA). The XC energy is shown as:

$$E_{XC}^{LDA}[\rho^{\uparrow}, \rho^{\downarrow}] \cong \int [\rho^{\uparrow}(r) + \rho^{\downarrow}(r)] \varepsilon_{XC}[\rho^{\uparrow}, \rho^{\downarrow}] dr^3 \tag{2-16}$$

The LDA generally will provide accurate descriptions of materials' properties, because the systematic error can be canceled by itself. The LDA has a good performance on many systems, especially the metallic system. The calculated basic properties (like structural parameters, phase stability, vibrational frequencies and density of states) are in good consistent with the results from experiment. However, LDA has some disadvantages. It is only suitable for systems with slow density change. When the distribution of electron density is inhomogeneous, it is difficult to describe the materials' properties. In addition, the LDA usually underestimates the band gaps of the materials.

In the actual system, the electron density is not uniformly distributed like free electron gas. Therefore, using gradient expansion for E_{XC} in the real system, the inhomogeneity of electron density can be better described. The GGA functional makes the XC energy rely on not only the electron density but also the derivative of the density, $\nabla\rho(r)$, and shows the form:

$$E_{XC}^{GGA}[\rho] \cong \int \rho(\vec{r})\varepsilon_{XC}[\rho(\vec{r})]d\vec{r} + \int F_{XC}[\rho(\vec{r}), \nabla\rho(\vec{r})]d\vec{r} \quad (2\text{-}17)$$

There are various forms of $E_{XC}^{GGA}[\rho]$. The commonly used XC functional for GGA are Perdew-Burke-Ernerhof (PBE),[112] Perdew-Wang 91 (PW91),[113] Becke,[114] BLYP[115] and so on. At present, PBE and PW91 are commonly used in the fields of physics and chemistry. The recently developed PBEsol is more suitable for solid surface and interface calculations.

As illustrated in Figure 2.1, Jacob's ladder is used to categorize functionals from LDA to hybrid-GGA. Although there are the strengths and weaknesses for each rung, the global predicted results for most properties and the related computational cost will increase as moving from the lower rung to the higher one. Hence, users can choose the functional according to their requirements for accuracy or computational efficiency.

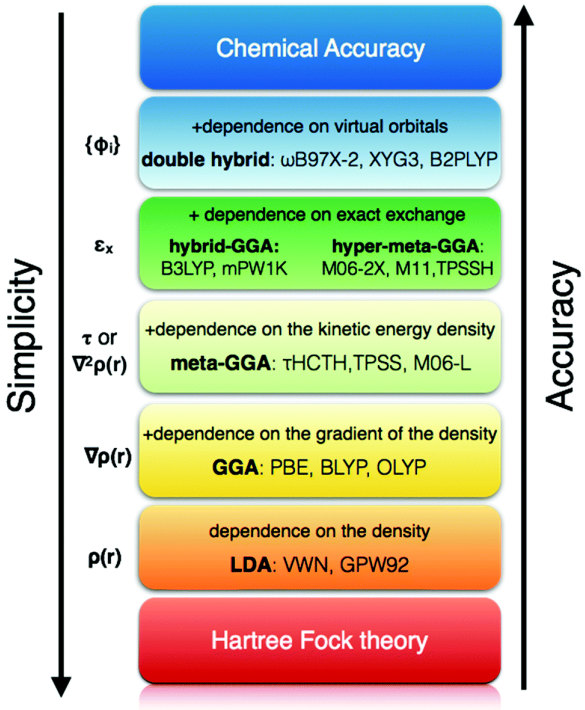

Figure 2.1. Illustration of XC functionals by the Jacob's ladder. Reproduced with permission.[116] Copyright 2016, Chemical Society reviews

2.3 Implementations

There are a wide-range of DFT-based calculation software packages and each has its own characteristics. The common used codes for solids are Vienna Ab initio Simulation Package (VASP),[117–120] quantum espresso (QE)[121] and ABINIT[122–126]. The main simulation code used in this project is VASP.

From DFT simulations, the energy of possible structures can be calculated to well predict the crystal structures. In addition to crystal structures, the structures of molecules and surface also can be optimized by DFT calculations. Among various physical properties, it is critical to know the electronic structure of materials. And density of state and band structure are the two quantities to describe materials' electronic structure, which can be obtained using DFT calculations. Moreover, the vibrational frequencies can be calculated to study the zero-point energies of materials. In the chemical reaction process, through

determining the transition states, the energy barriers can be calculated and hence the rates of the reaction can be measured. Furthermore, the surface energy and the molecular adsorption can be examined by DFT calculation, and the details of surface energy calculations are discussed in section 2.4. Therefore, DFT simulations have broad applications in the catalyst field, especially the catalytic activity on the surface of the structure.

2.4 Surface energy calculation

The symmetric slab with two same terminations is built to calculate the surface energy (γ).[127] The cleavage energy for the termination is calculated from the following equation:

$$E_{surf}^{unr} = \frac{1}{4}\left[E_{slab}^{unr}(\mathrm{A}) + E_{slab}^{unr}(\mathrm{B}) - \mathrm{n}E_{bulk}\right] \quad (2\text{-}18)$$

where E_{slab}^{unr}(A) and E_{slab}^{unr}(B) are the total energies of the unrelaxed slab with A and B terminations, respectively. E_{bulk} is the energy of the bulk and n is the number of the related bulk in these two slabs.

The relaxation energy can be obtained via equation:[128]

$$\Delta E_{surf}^{rel}(\mathrm{X}) = \frac{1}{2}\left[E_{slab}^{rel}(\mathrm{X}) - E_{slab}^{unr}(\mathrm{X})\right] \quad (2\text{-}19)$$

where E_{slab}^{rel}(X) and E_{slab}^{unr}(X) are the energies of the relaxed and unrelaxed X-terminated slabs, respectively. The surface energy of X-terminated surface is then given by:

$$\gamma(\mathrm{X}) = \left[E_{slab}^{unr}(\mathrm{X}) + \Delta E_{surf}^{rel}(\mathrm{X})\right]/\mathrm{S} \quad (2\text{-}20)$$

where S is the surface area of the slab.

2.5 OER mechanism

We study the OER at standard conditions (T = 298 K, P = 1 bar, pH = 0), within the computational SHE framework, by considering a widely used mechanism composed of four proton-coupled electron-transfer (PCET) steps:[12,26]

$$* + H_2O \rightarrow OH^* + H^+ + e^-, \quad (2\text{-}21)$$

$$OH^* \rightarrow O^* + H^+ + e^-, \quad (2\text{-}22)$$

$$O^* + H_2O \rightarrow OOH^* + H^+ + e^-, \quad (2\text{-}23)$$

$$OOH^* \rightarrow * + O_2 + H^+ + e^-. \quad (2\text{-}24)$$

where the symbol * indicates a surface reaction site and O*, OH* and OOH* are adsorbed oxygen, hydroxyl and hydroperoxy intermediates, respectively. It is assumed that the entire OER requires an energy of 4.92 eV (i.e. 1.23 eV for each of the four steps at equilibrium conditions).

We calculated the change in reaction free energy (ΔG) of each OER step as:

$$\Delta G(U, pH, T) = \Delta E + \Delta ZPE - T\Delta S + \Delta G_U + \Delta G_{pH} \quad (2\text{-}25)$$

where, the reaction energy ΔE can be obtained from the DFT total energies and ΔZPE is the change in zero-point energies. ΔS is the change in entropy, where for gas phase molecules values from standard tables are used [129], while the entropy of adsorbed species is assumed to be zero. The influence of a bias potential on all steps containing electron transfer is accounted for by modifying the free energy difference by $\Delta G_U = -eU$, where U is the electrode potential *vs* SHE. The free energy of H^+ ions depends on the concentration, thus the free energy of H^+ ions is corrected by the equation, $\Delta G_{pH} = k_B T \ln[H^+] = - k_B T \ln 10 \, pH$ at pH≠0.

The highest electrode potential is needed for the reaction with the largest Gibbs free energy to be downhill in Gibbs free energy. For example, in Figure 1.5, Gibbs free energy of step 3 to be downhill requires potential of 1.60 V.

As discussed in section 1.3.4, the theoretically thermodynamic overpotential (theoretical overpotential, η), can be used to qualitatively explain the OER activity, which is calculated by the following equation.[26]

$$\eta = \frac{\Delta G_{max}}{e} - 1.23\ V \quad (2\text{-}26)$$

The reaction with the largest Gibbs free energy (ΔG_{max}) among the four OER steps is hence the potential determining step. Since the Gibbs free energy (ΔG) of each reaction step is equivalently affected by $k_B T \ln 10 \, pH$ at pH≠0, the theoretical overpotential, η, is pH-independent.

The stability of the surfaces with O*/OH* coverage relative to the clean surface at pH=0 were calculated according to the following equations:[130]

$$\Delta G = \Delta E_{4O^*} - E_{clean} + 4E_{H_2} - 4E_{H_2O} + (\Delta ZPE - T\Delta S) - 8eU \quad (2\text{-}27)$$

$$\Delta G = \Delta E_{4OH^*} - E_{clean} + 2E_{H_2} - 4E_{H_2O} + (\Delta ZPE - T\Delta S) - 4eU \quad (2\text{-}28)$$

Chapter 3

Anion Ordering, Strain, and Doping Engineering of the OER in $BaTaO_2N$

This chapter is based on the work shown in paper 1-"Theoretical Insight on Anion Ordering, Strain, and Doping Engineering of the Oxygen Evolution Reaction in BaTaO2N". The paper is included in Appendix.

3.1 Introduction

Over the last decade, oxynitrides have been investigated for multiple applications, ranging from ferroelectricity,[131] over electrocatalysis[132] to photocatalysis.[3] In general, by combining oxygen and nitrogen as anions, oxynitrides show higher stability in air and moisture compared to pure nitrides, and the perovskite-structured oxynitrides display smaller band gaps than those of pure oxides,[73] which contribute to their attractive electronic and optical properties in photocatalysis or photoelectrocatalysis for water splitting devices. Among the identified compositions,[98] $BaTaO_2N$ is one of the promising candidates as photoelectrocatalysts for water splitting, because of its optical band gap (approximately 1.9 eV, which is close to the minimum energy needed to split water once the bare energy to split water and the reaction overpotentials are considered)[134] and band-edge positions, which straddle the redox potentials of the hydrogen and oxygen evolution reactions.[135–138] Although much effort has been carried out to improve the performance of $BaTaO_2N$ for water splitting, its photocatalytic activity is still far from practical applications.[135,136,139–141] One of the strategies to improve the catalytic activity is to reduce the overpotentials required to split water into molecular oxygen and hydrogen. The lowest theoretical overpotentials for the OER on oxides and oxynitrides are predicted to be 0.2-

0.4 V.[26] Therefore, the surface reaction, especially for OER, is a critical bottleneck, which currently limits the efficiency of solar-to-chemical conversion and ultimately the use of oxynitrides as materials for water splitting.

The properties of perovskite oxynitrides are sensitive to the surface local structure and oxygen/nitrogen ordering.[49,101,142] The ordering of the O/N anions in oxynitrides is caused by the four coordinate ionic radii of O^{2-} (1.38 Å) and N^{3-} (1.46 Å) and the corresponding chemical bonding environment (valence) between O/N and neighboring high-valence metals (M-O or M-N).[143,144] Therefore, different exposed surface terminations also show different O/N anionic orderings, which affects the physicochemical properties and catalytic activity.[145] In addition to this, doping and strain engineering have been proved to be effective methods in tailoring the surface electronic structures and catalytic properties.[146–149] Substitution (or partial substitution) of the A site and/or B site by other elements with different radii or valences,[150] as well as strain manipulations, can easily alter the geometrical and electronic structure of the active sites.[151] A typical example is efficient electrochemical N_2 reduction could be achieved by doping strain induced bi-Ti^{3+} pairs.[152] More specifically for perovskite oxynitrides, the changes in properties due to the applied strain have also been verified experimentally, starting from computational predictions, such as the change in the anion arrangement in $Ca_{1-x}Sr_xTaO_2N$,[151] the 2D to 3D crossover on a cubic lattice of correlated disorder of O and N atoms within the $Ba_{1-x}Sr_xTaO_2N$ series,[153] and the creation and switching of anion vacancy layers in $SrVO_{2.2}N_{0.6}$.[154] Another example is that epitaxial strain effects lead to a tetragonal distortion of the $BaTaO_2N$ perovskite unit cell, with negligible volume change, which shows a unique combination of high dielectric permittivities and insensitivity to changes in temperature.[155] Furthermore, a ferroelectric response in tensile-strained $SrTaO_2N$ films is observed due to a change of the anion ordering as a function of the applied strain.[156] Regarding the electronic properties, tuning of the bandgap has been achieved in Y-substituted $LaTaO_2N$ from an orthorhombic strain.[157] From the perspective of photocatalysis, controlling the morphological and structural variations of $LaTiO_2N$ and CoO_x nanoparticles could influence the strain in the structure and hence promote the photocatalytic O_2 evolution.[158] It has also been reported that Au-$SrTiO_3$ with tensile strain, where the strain is induced by the difference of the thermal expansion coefficient between Au and $SrTiO_3$, shows 10.5 times higher photocatalytic activity for water splitting than the unstrained Au-$SrTiO_3$.[159] The significant increase in the rate of H_2 and

O_2 formation has also been reported for strained TiO_2, where the strain is obtained by Au dispersion.[160]

In this chapter, we show that doping and strain engineering in particular can be used to improve the catalytic OER performance of $BaTaO_2N$ for water splitting. Using DFT calculations, we have investigated the role of anion ordering, strain and doping modifications in the OER for the (100) TaO_2N-terminated and (001) TaON-terminated surfaces of $BaTaO_2N$. The theoretical overpotential for OER on the clean TaO_2N surface (η = 1.64 V) is much higher than that of a clean TaON surface (η = 0.97 V). On the other hand, under realistic (photo-) electrochemical conditions, the full oxygen-covered TaO_2N surface shows the lowest theoretical overpotential of 0.37 V when 1% tensile uniaxial strain in the [001] direction (Figure 3.1b) is applied, compared to 0.59 V that can be achieved by the TaON termination with full OH coverage and 4% compressive uniaxial strain in the [010] direction. A possible strategy to achieve a lower theoretical overpotential closer to the theoretical limit is to combine strain with doping. The Ca-doped TaON-terminated $BaTaO_2N$ (001) surface, with 4% tensile uniaxial strain in [010] direction, shows a theoretical overpotential of 0.53 V for the clean surface.

3.2 Computational details

The calculations were performed by using the projector augmented wave (PAW)[161] potentials implemented in the VASP package[117] in the framework of the generalized gradient approximation (GGA). The Perdew–Burke–Ernserhof revised for solids (PBEsol) exchange-correlation potential[162] was used for optimizing the bulk structures, while for surface calculations we used the Perdew–Burke–Ernserhof (PBE).[163] The Brillouin zone of the 40-atom bulk unit cells, which is the smallest cell allowing the representation of the correct anion ordering, is sampled with a 6 × 6 × 6 Γ-centered Monkhorst–Pack k-point mesh and for the slab, it is sampled with a 6 × 6 × 1 Γ-centered Monkhorst–Pack k-point mesh.[164] The slab model includes eight atomic layers where the bottom four layers were fixed, and a vacuum thickness of 20 Å was added to separate the reciprocal images. For the doping modification, one Ba atom in the sublayer was replaced by Sr or Ca, and the corresponding doping concentration is 6.25%. Dipole correction was also included. Grimme's D3-type method was carried out for van der Waals interaction corrections.[165] A plane-wave energy cutoff of 550 eV was used. Cell and atomic positions were fully relaxed

until the forces on the atoms were below 0.02 eV/Å. These structures were then used to build the surface models, for which only the atomic positions have been relaxed, keeping the cell frozen. The energy barrier for formation of N_2 on the (100) surface of $BaTaO_2N$ was calculated using the climbing images nudged elastic band (CI-NEB) method and the structures were relaxed with force less than 0.05 eV/Å.[166] A more sophisticated semi-local functional (GLLB-SC)[167,168] was used to calculate the band gap of bulk $BaTaO_2N$ as implemented in the GPAW program package.[169] All data are stored and freely available at the address: DTU DATA.[170] The calculation of surface energy and OER mechanism can be seen in Chapter 2.4 and 2.5. An empirical method based on the electronegativity of the constituent elements, and the band gap was applied to estimate the valance-band edge.[171]

3.3 Results and discussion

3.3.1 Structure of $BaTaO_2N$

The perovskite structure of $BaTaO_2N$ exists two possible N/O orderings in the TaO_4N_2 octahedral structures: one is "cis-type" TaO_4N_2 octahedra corresponding to N–Ta–N bonds with 90° angles and the other one is "trans-type" octahedra with 180° N–Ta–N bonds drawn in Figure 3.1a.[172] Here, we consider different configurations with various 2D O/N orderings and the cis-ordered structure shown in Figure 3.1b, is thermodynamically most stable among all the structures considered. The 40-atom bulk supercell is the smallest cell allowing representation of the correct anion ordering as well as possible octahedral distortions. The corresponding lattice parameters are a = b = 8.287 Å and c = 8.095 Å. The band gap of bulk $BaTaO_2N$ is 2.49 eV, which is narrow enough to absorb visible light. To study photo-oxidation, it is essential to determine the position of valence-band edge versus SHE at pH=0 as the driving force for OER is provided by holes at the upper edge of the valence band. The calculated VB edge position is 2.20 eV *vs* SHE, which could provide an additional potential of 0.97 V with respect to the OER potential.

The two most commonly exposed (100) and (001) facets have been studied. As reported in Figure 3.1c-d, each facet has two terminations: for the (100) facet TaO_2N and BaON-terminated surface; and for the (001) facet, TaON and BaO_2-terminated surface. As indicated by the surface energies in Table 3.1, the Ta-exposed surfaces have the lowest energies, for both the (100) and (001) facets, for which we now investigate their catalytic

properties. For TaO_2N-terminated (100) surfaces, there are 1/3 N atoms within anions and the two N atoms are in the symmetric sites, while for the TaON-terminated (001) surface, there are 1/2 N atoms within anions and each two N atoms connected to the Ta atom forms N−Ta−N bonds with 90° angles.

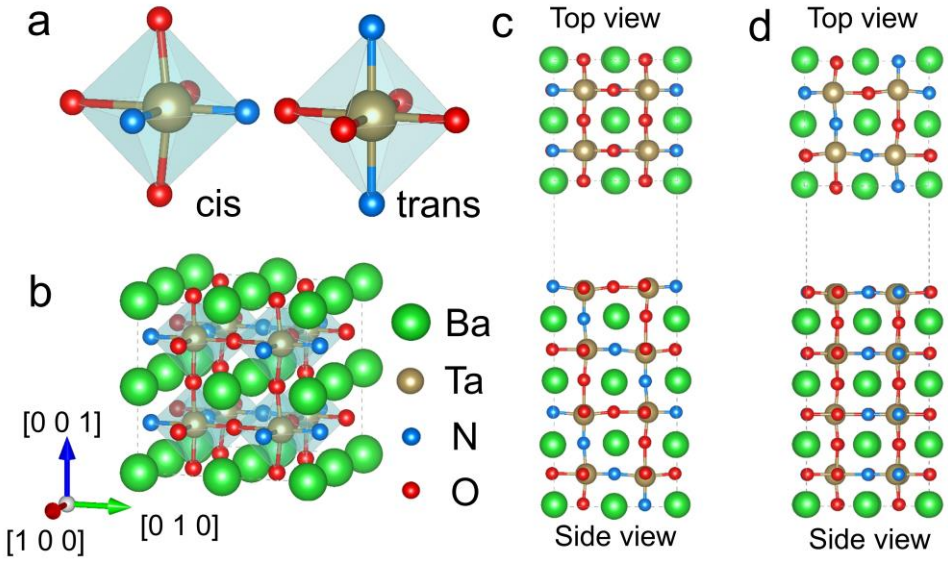

Figure 3.1. (a) Schematic representation of the anion ordering in a TaO_4N_2 mixed-anion octahedron. Structure of the (b) bulk $BaTaO_2N$, (c) (100) surface of $BaTaO_2N$ with TaO_2N termination on top and (d) (001) surface of $BaTaO_2N$ with TaON termination on top.

Table 3.1. Calculated surface energies of different surfaces

Facet	Termination	Surface energy (eV/Å^2)
(100)	TaO_2N	0.032
	BaON	0.056
(001)	TaON	0.081
	BaO_2	0.086

3.3.2 TaO_2N-terminated (100) surface

As shown in Figure 3.2 a-d, the OH and OOH fragments prefer to adsorb on top of one of the Ta atom on the surface. The situation is different for O. When there is only one O, it adsorbs on the bridge site between Ta and N, while for full O coverage, half O atoms are adsorbed on the bridge site and half O atoms are located on top of the Ta atom. To predict the most relevant surface coverage under (photo)-electrocatalytic operating conditions, surface Pourbaix diagrams are computed at pH = 0, as shown in Figure 3.2e. The clean surface is stable only at low potential (below 0.47 V). At operating conditions, where the potential is higher than 1.23 V, the full O coverage is the energetically most stable.

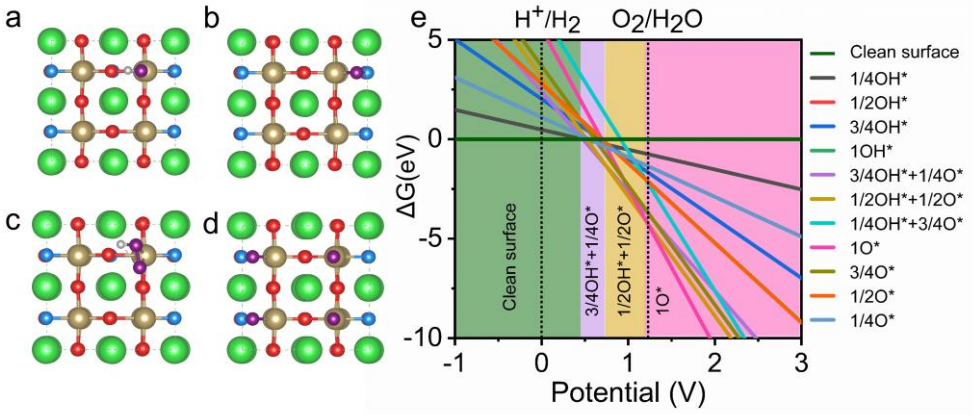

Figure 3.2. Structure of the (100) surface of TaO_2N-terminated $BaTaO_2N$ with (a) 1/4 OH, (b) 1/4 O, (c) 1/4 OOH and (d) 1 O adsorbates. The purple ball and white ball represent the adsorbate O and H atoms, respectively. (e) Surface Pourbaix diagram of the TaO_2N-terminated (100) surface at pH = 0.

To investigate the role of the surface, we first study the OER on the clean surface. The surface configurations are shown in Figure 3.3a: the deprotonation of the H_2O molecule forms OH in step 1; then in step 2, OH is deprotonated to form an adsorbed oxygen O, when it comes in contact with another deprotonated H_2O molecule forming OOH (step 3); and finally, in step 4, an O_2 molecule forms from the deprotonation of OOH and eventually leaves the surface. From the free energy diagrams (Figure 3.3a), we can see that the potential determining step (PDS) is the formation of OOH with a free-energy difference of 2.87 eV, which results in a theoretical overpotential of 1.64 V.

For the full O coverage, half of the O atoms are adsorbed on the bridge sites and half O on top of Ta, therefore there are three kinds of possible reaction sites resulting in three possible OER paths. First the reaction could continue from an O on the bridge site. While we find that OOH cannot be formed from the bridge O, which is similar to the surface reaction on Sr_2TaO_3N.[173] Then, we consider the reaction occurring from the O atom on top of the Ta atom (Ta_1), which shows a theoretical overpotential of $\eta = 0.74$ V in Figure 3.3b. Surprisingly, when the reaction happens on the Ta atom without O on the top sites (Ta_2), the theoretical overpotential is only 0.43 V (Figure 3.3c). For all OER processes, the PDS are the formation of OOH. To understand the reasons for the much lower theoretical overpotential of the latter mechanism, we calculate the Bader charges and the charge transfer q from the Ta. These values (Table 3.2) indicates that the Ta with adsorbed O on the bridge site is more oxidized, which weakens the Ta and O double bond, that breaks more easily on formation of the Ta-OOH intermediate (PDS) leading to a lower theoretical overpotential (0.43 V).

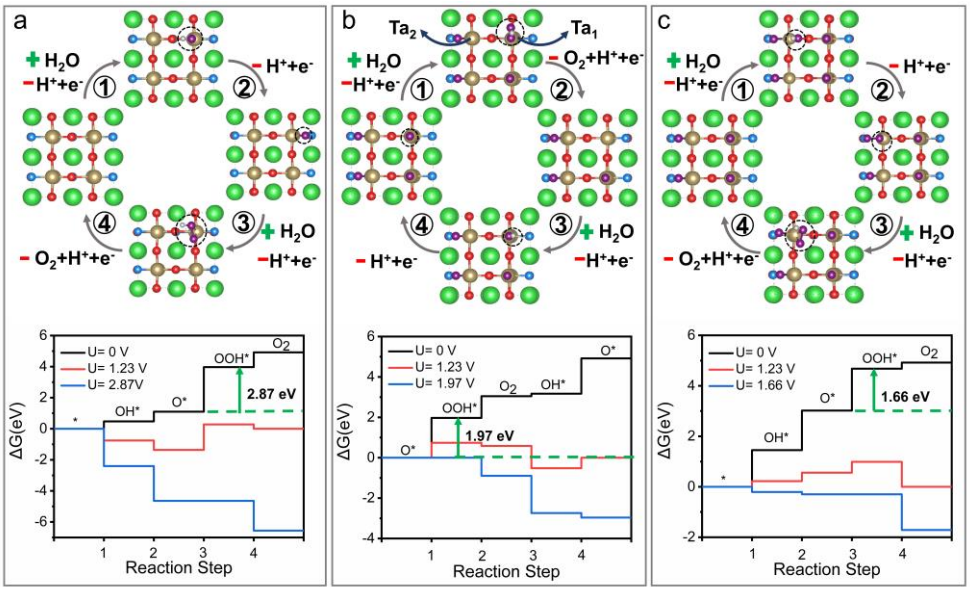

Figure 3.3. OER steps and Gibbs free energy diagrams for the (a) TaO_2N-terminated (100) clean surface, and for the TaO_2N-terminated (100) surface covered with full O (b) Ta_1 site and (c) Ta_2 site.

Table 3.2. Bader charge analysis of Ta in the TaO_2N-terminated (100) surface layer of $BaTaO_2N$ with full O coverage. A positive value q indicates that the electrons are removed from Ta.

	Average Bader charge	Charge transfer q (e)
Ta_1	8.44	+2.51
Ta_2	8.49	+2.56

Strain can be used to control the structure of the surface, with its electronic and catalytic properties. Therefore, to tune and improve the OER activity, we apply compressive and tensile uniaxial strain in both [010] and [001] directions, where the negative value means the compressive strain and the positive represents the tensile strain. As indicated by the volcano plot in Figure 3.4a, under uniaxial strain in the [010] direction the theoretical overpotential increases. This can be seen for both compressive and tensile strain, however the effect is more pronounced for tensile strain. This can be explained as a combination of a change in the electronic properties of the surface, in particular the hybridization of the O-2p and Ta-d orbitals, and a structural modification of the geometry of the surface and adsorbate under different strain conditions.[174] The response to the uniaxial strain in the [001] direction is, however, different. The change of the ΔG_{O^*}-ΔG_{OH^*} in Figure 3.4a is linear with the strain. Under 4% compressive strain, the theoretical overpotential increases from 0.43 to 0.77 V, while under tensile strain, the theoretical overpotential first decreases, reaching the top of the volcano and afterward increases, on the other branch of the volcano. The lowest theoretical overpotential is reached at 1% tensile strain and it is equal to 0.37 V. On the left leg of the volcano, the PDS is the formation of OOH (Figure 3.4b and 3.5a-c), while on the right branch, we find that the formation of O is the PDS (Figure 3.4d and 3.5d). At 1% tensile strain, which is found at the top of the volcano, the PDS is shared between the formation of OOH and O (Figure 3.4c). Hence, the uniaxial strain in the [001] direction can be used to modulate the PDS and tune the OER theoretical overpotential, by changing the adsorption energies of OOH and O on the surface.

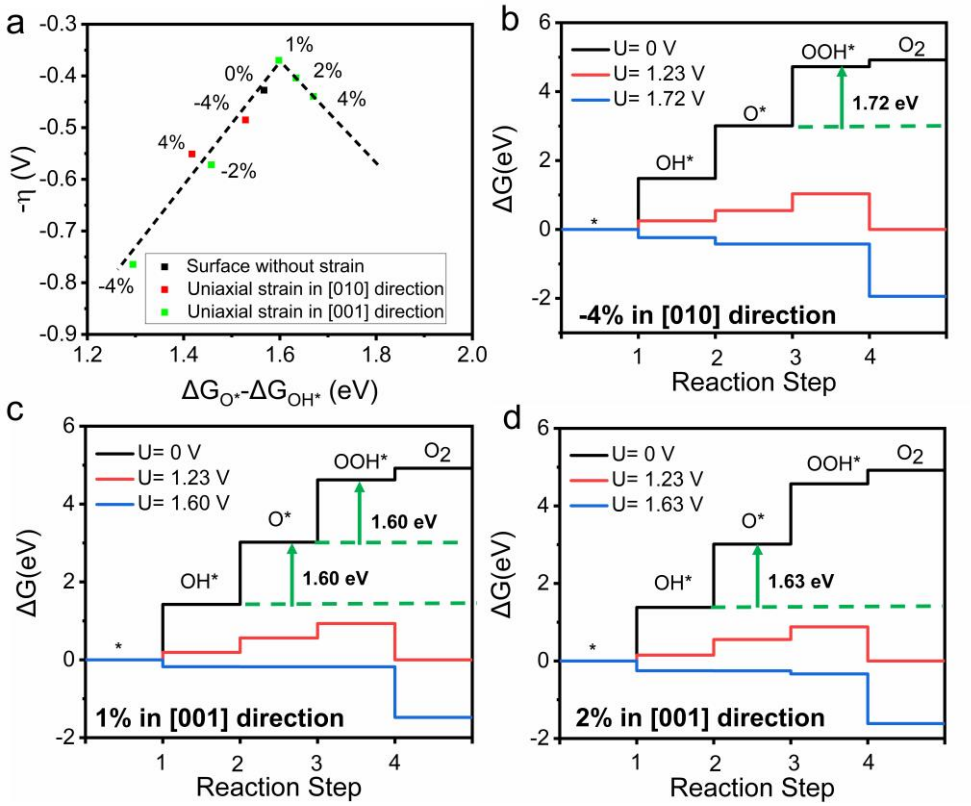

Figure 3.4. (a) Volcano plot of the free-energy difference of (ΔG_{O*}-ΔG_{OH*}) and the OER theoretical overpotential (η) for TaO_2N-terminated (100) full O covered surfaces. Gibbs free energy diagrams for the full O covered TaO_2N-terminated (100) surface with (b) 4% compressive uniaxial strain in the[010] direction, (c) 1% tensile uniaxial strain in the [001] direction and (d) 2% tensile uniaxial strain in the [001] direction.

It should be noted that the oxidation of the N^{3-} ions forming N_2 has been put forward for oxynitrides[175] and perovskite oxynitrides[176] by photo-generated holes during the photocatalytic reaction, which have been supported by an obvious decrease in nitrogen content indicated by XPS. Therefore, we perform NEB calculations to investigate the migration of the surface N atoms to form N_2. As shown in Figure 3.6, the energy barrier is 1.05 eV, and the process is therefore kinetically hindered compared to OER.

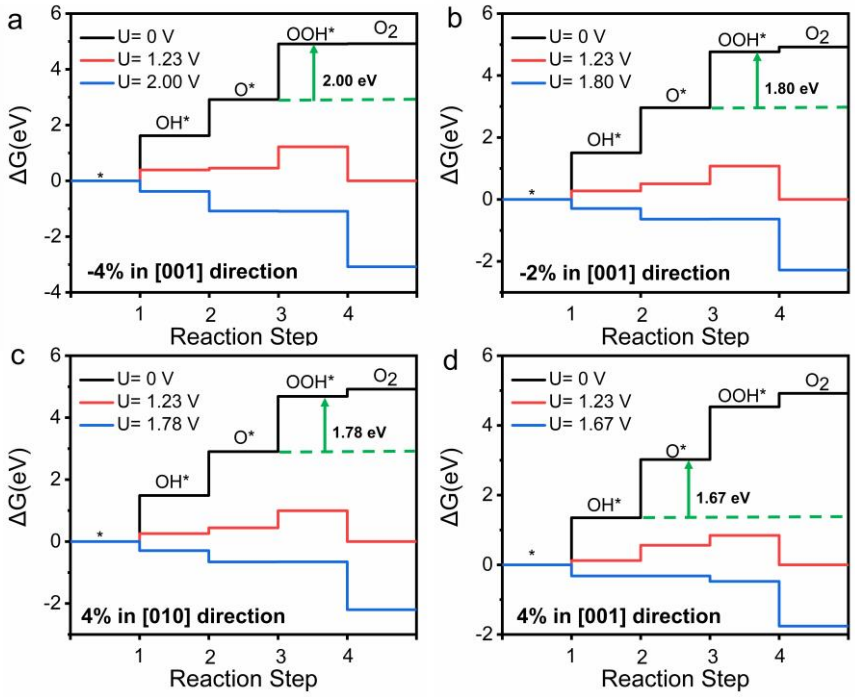

Figure 3.5. Gibbs free energy diagrams for the full O covered TaO_2N-terminated (100) surface with (b) 4% compressive uniaxial strain in the [001] direction, (c) 2% compressive uniaxial strain in the [001] direction, 4% tensile uniaxial strain in the [010] direction, and (d) 4% tensile uniaxial strain in the [001] direction.

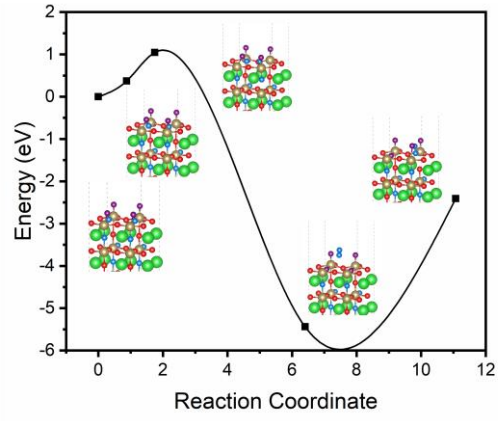

Figure 3.6. Energy barrier of surface nitrogen to for N_2 on the surface.

3.3.3 TaON-terminated (001) surface

Compared to perovskite oxides where all anions are oxygen, the N/O ordering differs from facet to facet. As shown in Figure 3.1c-d, the TaON-terminated (001) surface shows an obviously different N/O order compared to the TaO_2N-terminated (100) surface. On the TaON-terminated (001) surface, the two N atoms connected to the Ta atom forms N−Ta−N bonds with 90° angles. The difference of the N distribution on the surface then will influence the adsorption of the fragments. The photocatalytic properties of the different facets can thus change significantly. As shown in Figure 3.7a, for the clean (001) surface, the PDS is the formation of OOH resulting in a theoretical overpotential of 0.97 V, which is lower than the theoretical overpotential of the corresponding (100) surface (1.64 V). This is caused by a change in the adsorption of O. On the (001) surface, the O would like to be adsorbed on top of Ta, while on the (100) surface, the O prefers on the bridge site with a strong bond with N, which is hard to break to form OOH.

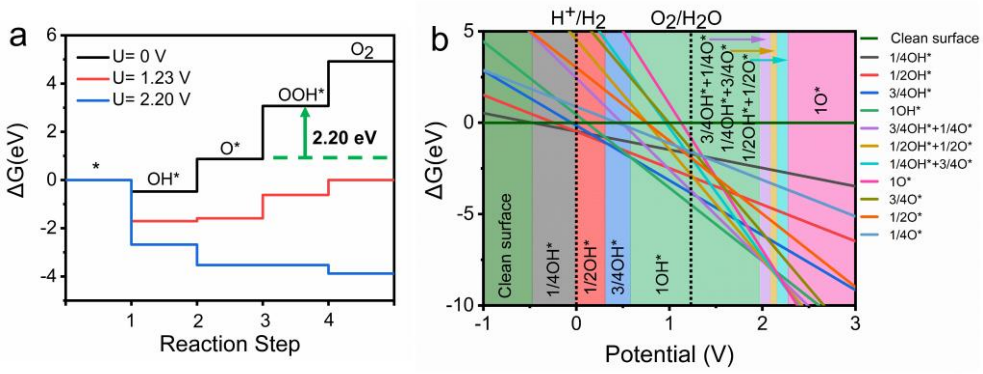

Figure 3.7. (a) Gibbs free energy diagrams for the TaON-terminated (001) clean surface. (b) Surface Pourbaix diagram of the TaON-terminated (001) surface at pH=0.

As shown in Figure 3.8, under 4% tensile uniaxial strain, the theoretical overpotential decreases from 0.97 to 0.69 V for the clean surface, while when 4 % compressive uniaxial strain is applied, the theoretical overpotential changes from 0.78 to 0.59 V for the full OH covered surface (most stable under operating conditions shown in Figure 3.7b). Doping can be a valuable alternative to strain to modulate the theoretical overpotentials. Since for the clean (001) TaON surface, tensile uniaxial strain could reduce the theoretical overpotential to only 0.69 V, we attempt to further decrease the theoretical overpotential,

by combining the substitution of Ba with isovalent elements with smaller radii and strain. We thus replace a sublayer Ba with Ca and Sr. It should be noted that doping alone only has a small effect on the OER activities. Sr-doping slightly reduces the theoretical overpotential from 0.97 to 0.90 V, and Ca-doping further reduces it to 0.88 V. Moreover, combining with 4% tensile uniaxial strain, the smallest theoretical overpotential is reached for the Ca-doping on the clean surface (0.53 V), which results from ΔG_{O^*}-ΔG_{OH^*} increasing with doping and strain. All structures with the full OH coverage surface are already on the right branch of the volcano, and 4% compressive strain is not enough to reach the top of the volcano. In general, this facet requires larger strain compared to the (100) facet, which might be hard to achieve experimentally.

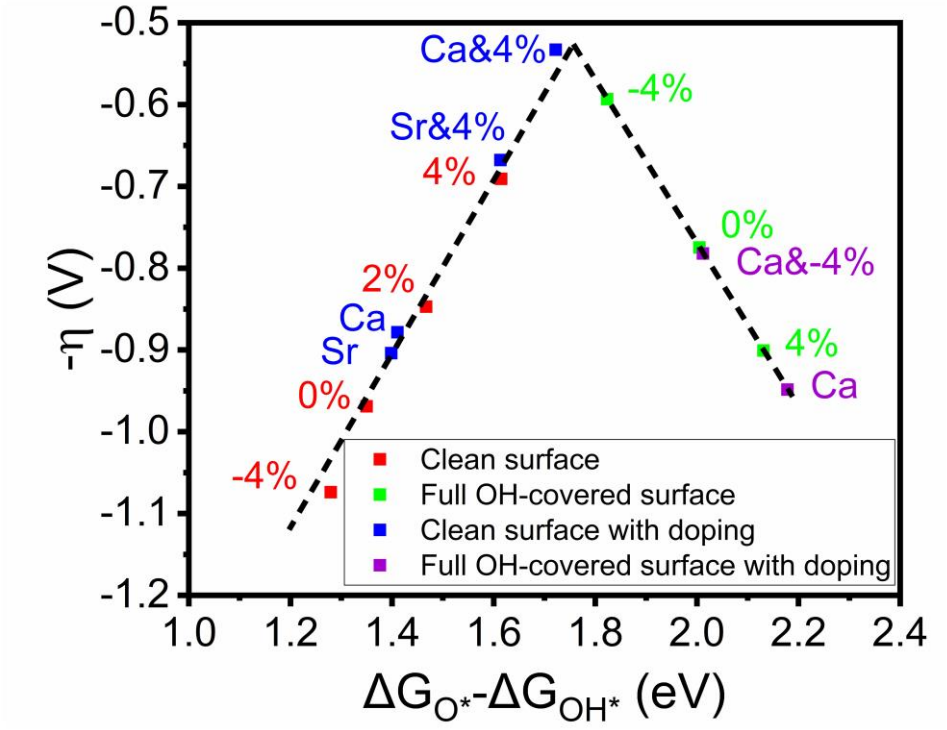

Figure 3.8. Volcano plot of the free-energy difference of (ΔG_{O^*}-ΔG_{OH^*}) and the OER theoretical overpotential (η) for both TaON-terminated (001) clean and full OH covered surfaces. The uniaxial strain is in the [010] direction.

3.4 Summary

In this chapter, we have investigated the effect that doping and strain engineering have on the oxygen evolution reaction for different terminations of the perovskite oxynitride $BaTaO_2N$. For the (100) facet TaO_2N-terminated surface, under (photo)electrochemical conditions, we have discovered that 1% tensile uniaxial strain in the [001] direction can lower the theoretical overpotential to 0.37 V from 0.43 V calculated for the structure without any applied strain. The (001) facet shows larger theoretical overpotentials compared to the (100). As an attempt to reduce them, we apply stain, reaching a theoretical overpotential of 0.59 V, under operational conditions, which, however, is still larger than what we can achieve for the (100) facet. The reason for the difference between the (100) and (001) facets is related to the different anion orderings on the surface. By applying a small strain of 1%, which can be easily reached in experiments, this work provides guidelines to experimentalists on how we can tune surface chemistry and optimize the OER catalytic properties of the material only by controlling anion ordering, strain, and doping.

Chapter 4

Enhancing OER by using switchable polarization in ferroelectric $InSnO_2N$

In the previous chapter we have studied the effects that doping and strain engineering have on the OER for different terminations of the perovskite oxynitride. In this chapter, we further study how the polarization influences the OER activities, especially the polarization in ferroelectric oxynitrides. The main text is based on the work shown in paper 2-"Enhancing Oxygen Evolution Reaction Activity by Using Switchable Polarization in Ferroelectric $InSnO_2N$". The paper is also included in Appendix.

4.1 Introduction

Photoferroic materials that combine ferroelectric and light-harvesting properties, are promising for optoelectronic applications, like photovoltaics[177,178] or photo(electro)chemical (PEC) water-splitting.[179] The spontaneous polarization of ferroelectrics can be reversed by application of an external electric field, with potential benefits for photoelectrocatalytic water splitting.[95,96,180,181] Due to the strong internal electric field induced by the spontaneous electric polarization, the photogenerated electrons and holes migrate in opposite directions, which enhances charge-carrier separation and promotes photocatalytic properties.[182,183] To date, more than 700 ferroelectric materials have been discovered,[184] the majority of those studied for photoelectrocatalytic applications are complex oxides, such as perovskite oxides, $BiFeO_3$,[185] $PbTiO_3$[186,187] and $BaTiO_3$.[92,188] However, their band gaps are in the ultraviolet (UV) range, they are therefore unable to absorb visible light. Although ferroelectricity

could suppress the recombination of photo-induced carriers, the large band gap of these oxides will inhibit practical photocatalytic applications. To solve this, the methods like substitution of one or more oxygen by nitrogen which leads to the so-called oxynitrides has been proposed.[45,70] Compared to oxygen, the lower electronegativity of nitrogen results in reduced band gaps and higher valence band edges that better match the water redox levels.[189–191] Recently, a tin oxynitride-based semiconductor, $InSnO_2N$, was suggested as a new and promising photocatalyst. It has a direct band gap of approx. 1.61 eV, resulting in excellent light absorption.[77] $InSnO_2N$ (Figure 4.1a) is isostructural to the multiferroic hexagonal manganites, h-$RMnO_3$ (R=Y, In, Sc, Ho-Lu). These materials are improper ferroelectrics, in which the corner-sharing Mn-O trigonal bipyramids are separated by layers of R ions and the tilting of the corner-sharing Mn-O trigonal bipyramids leads to the "up-down-down" R-cation displacement along c axis (or [001]) that causes polarization as a secondary effect and promotes separation of photoexcited carriers.[192,193]

In addition to light absorption and carrier separation, the performance of $InSnO_2N$ in a photoelectrochemical device, will depend on its surface redox reaction properties,[194] which are currently unknown. The major obstacle among the water-splitting redox reactions, is the low efficiency of the oxygen evolution reaction (OER).[195–197] The OER is a multistep reaction involving several intermediates and every step is vital for the overall conversion efficiency.[24,198] The interaction between catalyst surface and intermediate, strong or weak, will directly affect the reaction activity. According to the Sabatier principle, if the interaction is too weak, the adsorbate (i.e. the reagent) will be unable to bind to the catalyst, while if the interaction is too strong, the reaction product will fail to desorb.[97,199] Consequently, an optimal binding strength corresponds to the maximum OER efficiency and a minimum theoretical overpotential. DFT calculations have demonstrated that the four-step OER mechanism is fundamentally limited to a minimum theoretical overpotential of 0.3-0.4 V, due to the scaling relation between the binding strength of the OH and OOH intermediates.[26,200] The adsorption strength between the catalyst and intermediate largely depends on the surface electronic states. In a ferroelectric material, the surface states and their occupation could be altered by switching the polarization direction.[93,94,201,202] For a given surface, switching of the polarization direction can be used to optimize the adsorption strength for intermediates along the OER pathways, overcoming the limit imposed by the Sabatier principle.

In this work, we have used DFT calculations to investigate the OER performance of $InSnO_2N$ surfaces with negatively/positively polarized bulk. We find that the clean surface with a downward (negatively) polarized bulk has a lower theoretical overpotential of 0.58 V *vs* SHE than the clean surface with an upward (positively) polarized bulk (0.77 V). Under (photo)-electrochemical operating conditions, for the negatively polarized bulk, a 1 monolayer (ML) OH covered surface is the most stable while for the positively polarized bulk, a 2/3 ML OH coverage is preferred. The overpotentials for the OER on the OH covered surfaces with negatively and positively polarized bulk are both 0.89 V. When the polarization direction is switched during the OER, a much lower theoretical overpotential of 0.20 V is achieved for the clean surface and 0.23 V for the surface with OH coverage. These values are far below the minimum theoretical overpotential for oxides (0.37 V),[26] demonstrating that improper ferroelectric switching of suitable-band gap photoelectrodes is an exciting route to boost the OER activity, the enhancement in reaction free energies outweighing the energetic cost for polarization switching by a factor 6-12.

4.2 Computational details

DFT calculations were performed with the Vienna Ab initio Simulation Package (VASP).[117–119] Exchange and correlation effects were described using the Perdew−Burke−Ernzerhof (PBE) functional, in the framework of the generalized gradient approximation (GGA).[163] We used projector augmented wave (PAW)[203] potentials to represent the frozen core electrons and nuclei of each atom, and In (5s, 5d, 5p), Sn (5s, 4d, 5p), O (2s, 2p), and N (3s, 3p) were described as valence electrons, with a plane wave cutoff energy of 520 eV. We used a 6 × 6 × 3 Γ-centered Monkhorst Pack k-point mesh[164] for the bulk unit cell (30 atoms) and a 6 × 6 × 1 mesh for slab models (66 atoms). For the calculations of the partial density of states (PDOS), we used a Γ-centered k-point mesh with 12 × 12 × 6 for the bulk unit cell and 12 × 12 × 1 for the slab. The slab model is composed of 9 atomic layers where the bottom 4 layers are kept fixed during relaxation, a 20 Å vacuum was added to avoid artificial interaction between periodic images and a dipole correction was included.[204] Grimme's D3-correction was used to account for van der Waals interactions.[165] The spontaneous polarization was calculated according to the Born effective charge method,[205] where the Born effective charges are derived within Density

Functional Perturbation Theory (DFPT).[206] All atoms were fully relaxed during the structural optimization until the force on each atom was less than 0.02 eV/Å. The band gap was determined using the HSE06[207] hybrid functional with a plane wave cutoff of 350 eV and a 6 × 6 × 3 Γ-centered k-point mesh. We studied the OER at standard conditions (T = 298 K, P = 1 bar, pH = 0), within the computational standard hydrogen electrode (SHE) framework, by considering a widely used mechanism that consists of four proton-coupled electron-transfer (PCET) steps (see *OER mechanism*, in section 2.5).[26,208] The Pourbaix diagram gives information regarding the stability against dissolved phases, ions and chemical reactions with water.[209] The detailed calculation method is explained in ref 50. All data are stored and freely available in the DTU Data Repository.[210]

4.3 Results and discussion

4.3.1 Structure and properties of $InSnO_2N$

The $InSnO_2N$ structure studied in this work is hexagonal and belongs to the polar space group $P6_3cm$, as shown in Figure 4.1a. The optimized lattice constants are a=b=6.16 Å, c=12.24 Å. The distortion of the Sn-O-N trigonal bipyramids leads to an "up-down-down" corrugation of the In cations along c axis (or [001]) with a polarization of 12.04 μC/cm^2, analogous to the improper ferroelectricity in the hexagonal manganites.[192,211] During ferroelectric switching, the structure goes through a centrosymmetric phase ($P\bar{3}c1$) shown in Figure 4.2a. Therefore, the energy difference between the non-polar $P\bar{3}c1$ (Figure 4.2a) and the polar $P6_3cm$ structures (Figure 4.1c) is calculated to evaluate the energy barrier for polarization switching. We find an energy difference of 5.50 meV/atom, which is close to the switching energy barrier calculated for $YMnO_3$ (5 meV/atom),[212,213] but much smaller than that for $BaTiO_3$ (28 meV/atom),[214] indicating that the polarization in $InSnO_2N$ can be switched using electric fields. The stability of $InSnO_2N$ in the solution has also been studied by Pourbaix diagram in Figure 4.1b. The yellow zone represents that $InSnO_2N$ is stable under a broad range of potential and pHs, corresponding to the working OER conditions. $InSnO_2N$ can be stable even at the highly acidic/alkaline condition. To evaluate the light absorption properties, we calculate the band structure of bulk $InSnO_2N$ using HSE06: the polar phase $InSnO_2N$ is a direct semiconductor with band gap of 1.61 eV where both the valence band maximum (VBM) and the conduction band minimum (CBM) are located at the Γ point (Figure 4.1d). The suitable band gap and

direct transition are desirable to absorb a large fraction of solar light. As for the non-polar phase, the band gap is 1.45 eV (Figure 4.2b) which is slightly smaller than the polar one.

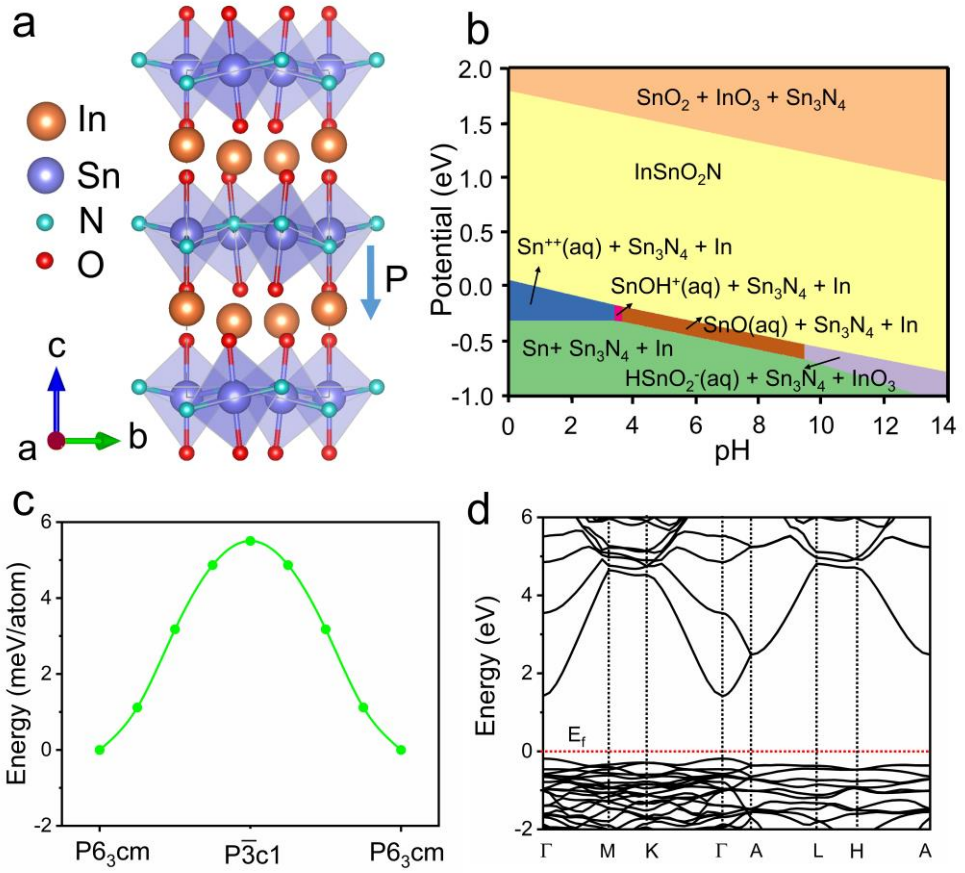

Figure 4.1. (a) Structure of bulk $InSnO_2N$ with $P6_3cm$ space group. The arrow represents the polarization direction. (b) Calculated Pourbaix diagram for $InSnO_2N$. The diagrams are drawn for a concentration of 10^{-6} M at 25 °C. (c) Energy barrier of $InSnO_2N$ during through the centrosymmetric $P\bar{3}c1$ phase. (d) HSE06 band structure of bulk $InSnO_2N$ with $P6_3cm$ (polar) space group.

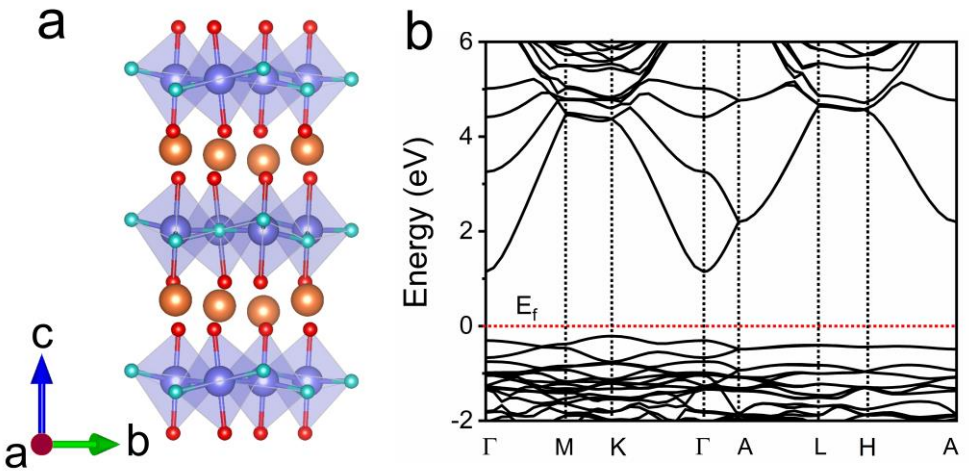

Figure 4.2. (a) Structure of bulk $InSnO_2N$ with space group of $P\bar{3}c1$(centrosymmetric phase). (b) HSE06 band structure of bulk $InSnO_2N$ with $P3\bar{c}1$ (non-polar) space group.

Changes in polarization direction perpendicular to the surface could be used to modulate the surface properties.[93] As the polarization in $InSnO_2N$ lies along the c axis (or [001]) direction, we study the OER on the (001) surface. The (001) facet has two terminations, SnN and InO_2. To determine which termination is more stable, we calculate surface energies[127,128] of 1.45 J/m^2 and 1.68 J/m^2, for the SnN and InO_2 terminations respectively and consequently investigate the OER on the more stable SnN termination. After surface relaxation, the In corrugations remain "up-down-down" for the slab with negatively polarized bulk (Figure 4.3a) and "down-up-up" for the slab with positively polarized bulk (Figure 4.3d). It should be noted that the polarization in each layer is highly dependent on the paraelectric reference state used to calculate the polarization. When the unrelaxed centrosymmetric phase is used as reference, all relaxed layers have a negative polarization for the nominally negatively polarized slab (Figure 4.3b). On the other hand, for the positively polarized slab, due to the surface relaxation, there is an effective reversal of the polarization in the first three layers, as shown in Figure 4.3e, despite the fact that the In corrugation does not change. When the relaxed centrosymmetric phase is used as reference, only the first subsurface layer in the negatively polarized slab has a

small positive polarization (Figure 4.3c) and only the surface layer in the positively polarized slab has a small negative polarization (Figure 4.3f). Since the In corrugation is retained, we believe that relaxations of the interlayer spacing and interlayer rumpling are responsible for the subtle local changes in the sign of the polarization.

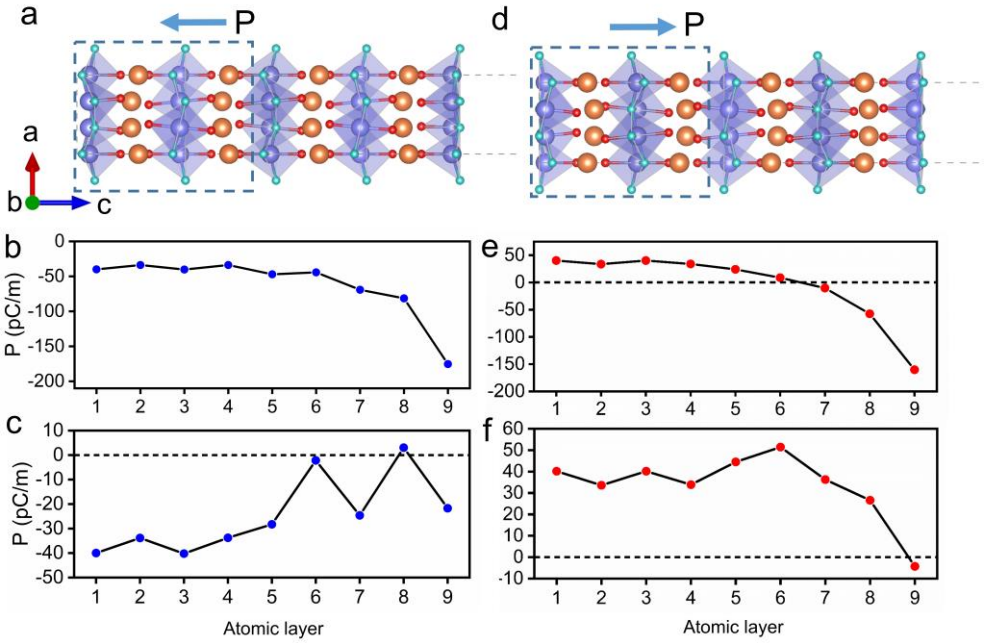

Figure 4.3. (a) Structure of the $InSnO_2N$ (001) surface with negatively polarized bulk. Layer-by-layer out of plane spontaneous polarization of the $InSnO_2N$ (001) surface with negatively polarized bulk using (b) the unrelaxed (c) the relaxed centrosymmetric phase as reference state. (d) Structure of the $InSnO_2N$ (001) surface with positively polarized bulk. Layer-by-layer out of plane spontaneous polarization of the $InSnO_2N$ (001) surface with positively polarized bulk using (e) the unrelaxed (f) the relaxed centrosymmetric phase as reference state. The blue arrows represent the polarization direction.

We investigate the electronic structure for the two slabs with oppositely polarized bulk. From the layer-resolved partial density of states (Figure 4.4), there is a positive shift of the Fermi level for the surface with positively polarized bulk compared to the surface with negative polarization direction, which implies electrons transfer to the surface. This is also conformed from the Bader analysis (Table 4.1), which shows charge of positively

polarized surface is 0.14 electrons more than the charge of the negatively polarized surface.

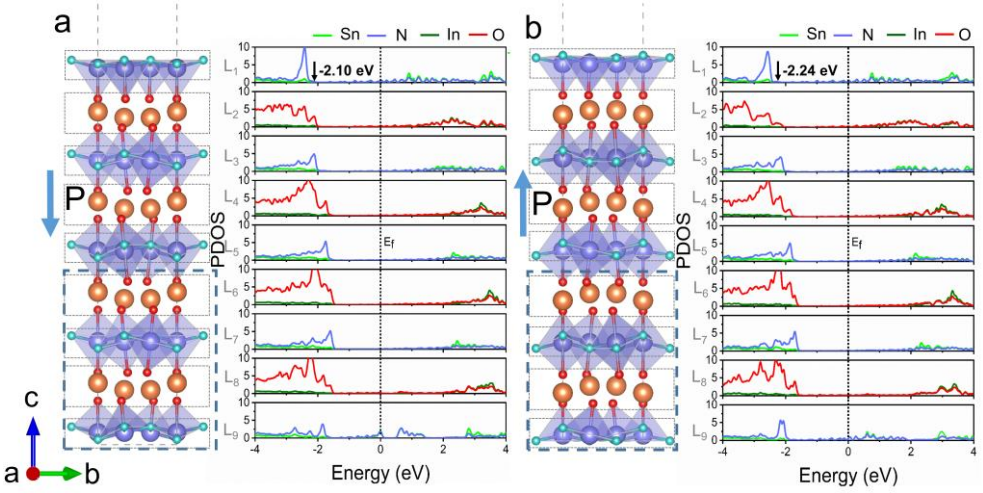

Figure 4.4. Structures and layer-resolved partial density of states (PDOS) of the $InSnO_2N$ (001) surface with (a) negatively polarized bulk and (b) positively polarized bulk. The arrow represents the polarization direction. L_n (1, 2, 3…9) corresponds to the atomic layer of the left structure. The bottom four-layer atoms marked by the dashed rectangle are fixed during the optimization.

Table 4.1. Net charge of the atoms on the surface according to Bader charge analysis. Positive value indicates that the electron is removed from the atom.

	N_1 (e)	N_2 (e)	N_3 (e)	Sn_1 (e)	Sn_2 (e)	Sn_3 (e)
Negative	-1.43	-1.40	-1.40	1.87	1.87	1.87
Positive	-1.40	-1.40	-1.42	1.82	1.82	1.82

4.3.2 OER on the SnN-terminated surface

To study the effect of the polarization on the OER activity, we first calculate free energy differences for the reaction steps on the clean (without adsorbates) (001) surface with oppositely polarized bulk. From the free energy profile of the OER in Figure 4.5, we find that for the surface with a negatively polarized bulk, the potential determining step is the

formation of O, resulting in a theoretical overpotential of 0.58 V. For the surface with a positive bulk polarization, the binding energies of the adsorbates are more negative as shown in Table 4.2. This is due to the higher electron density on the surface with positively polarized bulk. The potential determining step also changes to the formation of OOH and results in a theoretical overpotential of 0.77 V.

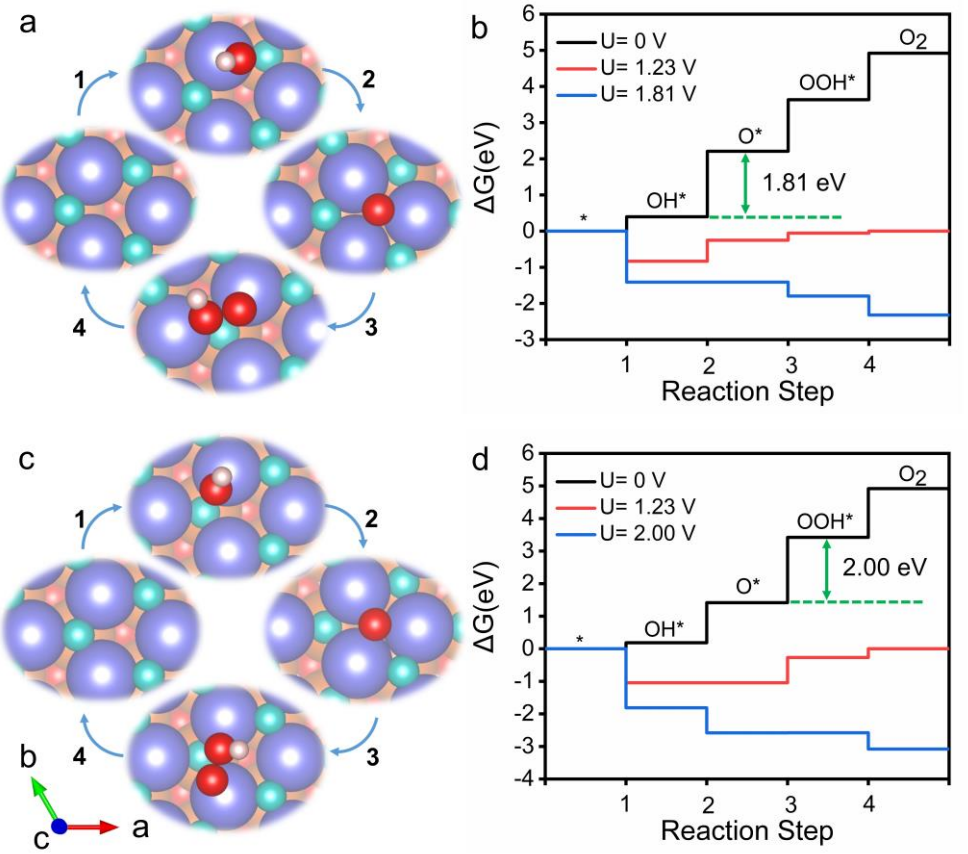

Figure 4.5. (a) OER steps and (b) Gibbs free energy diagram for the clean $InSnO_2N$ (001) surface with negatively polarized bulk. (c) OER steps and (d) Gibbs free energy diagram for the clean $InSnO_2N$ (001) surface with positively polarized bulk. Color code: In = orange, Sn = violet, O = red, N = cyan, H = pale pink.

Table 4.2. Calculated Gibbs adsorption free energies of the three OER intermediates on the (001) surface with negatively/positively polarized bulk.

	ΔG_{OH^*} (eV)	ΔG_{O^*} (eV)	ΔG_{OOH^*} (eV)
Surface with negatively polarized bulk	0.40	2.21	3.64
Surface with positively polarized bulk	0.19	1.42	3.42

The surface structure changes under OER operating conditions, and we evaluate the stable adsorbate coverage via surface Pourbaix diagrams for surfaces with negative and positive bulk polarization at pH=0. In Figure 4.6a, we see that, for the surface with negatively polarized bulk, at a potential close to zero, the clean surface is the most stable. When the potential is in the range between 0.39 and 1.07 V, the surface prefers to be covered with 1/3 ML OH. In the range of 1.07 to 1.53 V, a 1 ML OH coverage is thermodynamically favored. For higher potentials, the surface prefers to be covered with 1 ML O. For the positively polarized surface (Figure 4.6b), when the potential is lower

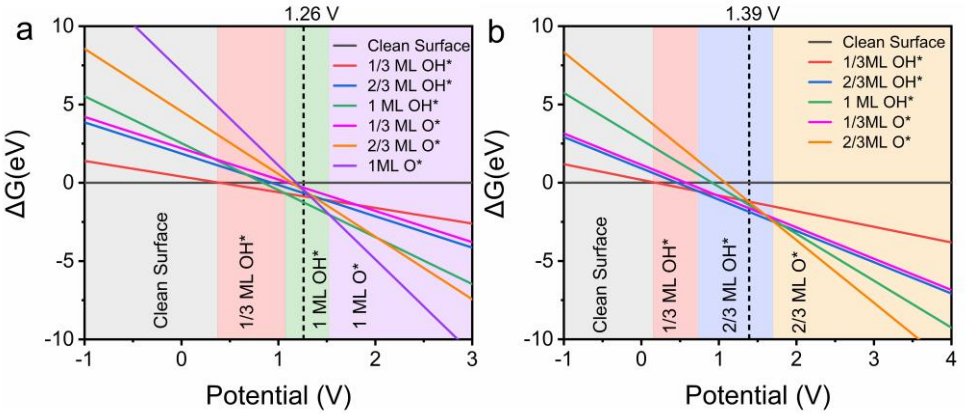

Figure 4.6. Surface Pourbaix diagram of the SnN terminated (001) surface at pH=0 with (a) negatively polarized bulk and (b) positively polarized bulk. The dotted lines represent the redox potential of the photogenerated holes.

than 0.14 V, the clean surface is the most stable. The 1/3 ML OH covered surface becomes the most stable for the potential between 0.14 and 0.72 V. While the most stable surface

changes to the 2/3 ML OH covered surface for the potential in the range of 0.72–1.71 V. When the potential is higher than 1.71 V, the surface prefers to be covered with 2/3 ML O.

As the working potential of the photocatalyst is determined by the energy difference between the VBM and the SHE, we evaluate the position of valence band edge of bulk $InSnO_2N$ with respect to the SHE as 1.89 eV via an empirical method.[171,173,215] The band edges of the various surfaces have further been evaluated by aligning the density of states (DOS) of bulk $InSnO_2N$ and its surfaces at In 1s states. For the surface with negatively polarized bulk, the estimated surface VBM is 1.26 eV *vs* SHE (Figure 4.6a) and the surface is covered with 1 ML OH at this potential. For the surface with positively polarized bulk, the estimated surface VBM is 1.39 eV *vs* SHE and, as shown in Figure 4.6b, the surface is covered with 2/3 ML OH at this potential.

When OER happens on the 1 ML OH covered surface with negatively polarized bulk, as shown in Figure 4.7a, there are two possible OH positions, one on top of a Sn atom and the other on top of an N atom. We find that the OER is more facile when started from the OH on top of the Sn atoms. The free energy diagram (Figure 4.7b) reveals that the potential determining step is the formation of OOH with a free energy change of 2.12 eV, corresponding to a fairly large theoretical overpotential of 0.89 V.

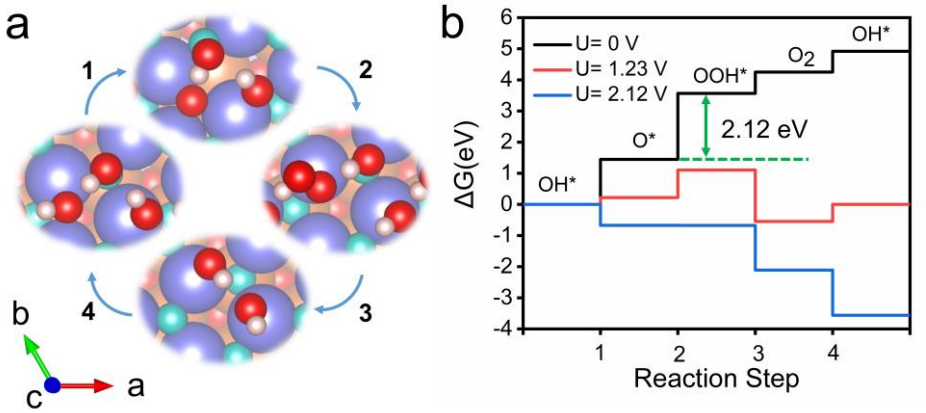

Figure 4.7. (a) OER steps and (b) Gibbs free energy diagram for the 1 ML OH* covered $InSnO_2N$ (001) surface with negatively polarized bulk.

Unlike on the negatively polarized one, the OER on the 2/3 ML OH* covered surface with positively polarized bulk has two possible paths. As shown in Figure 4.8a-b, the OER starting from an OH, proceeding in a similar fashion to the negatively polarized bulk, requires a theoretical overpotential of 0.89 V. On the other hand, as shown in Figure 4.8c-d, the OER can also start via the deprotonation of one H_2O molecule on the top site of the Sn atom. Interestingly the OOH fragment is unstable on top of the Sn and will spontaneously dissociate into two O fragment adsorbed on top of the Sn, while H binds to OH on a neighboring site to form H_2O bound to a Sn atom. In this mechanism, the potential determining step is the formation of two O fragment which corresponds to a change in free energy of 2.27 eV, corresponding to a much higher theoretical overpotential of 1.04 V.

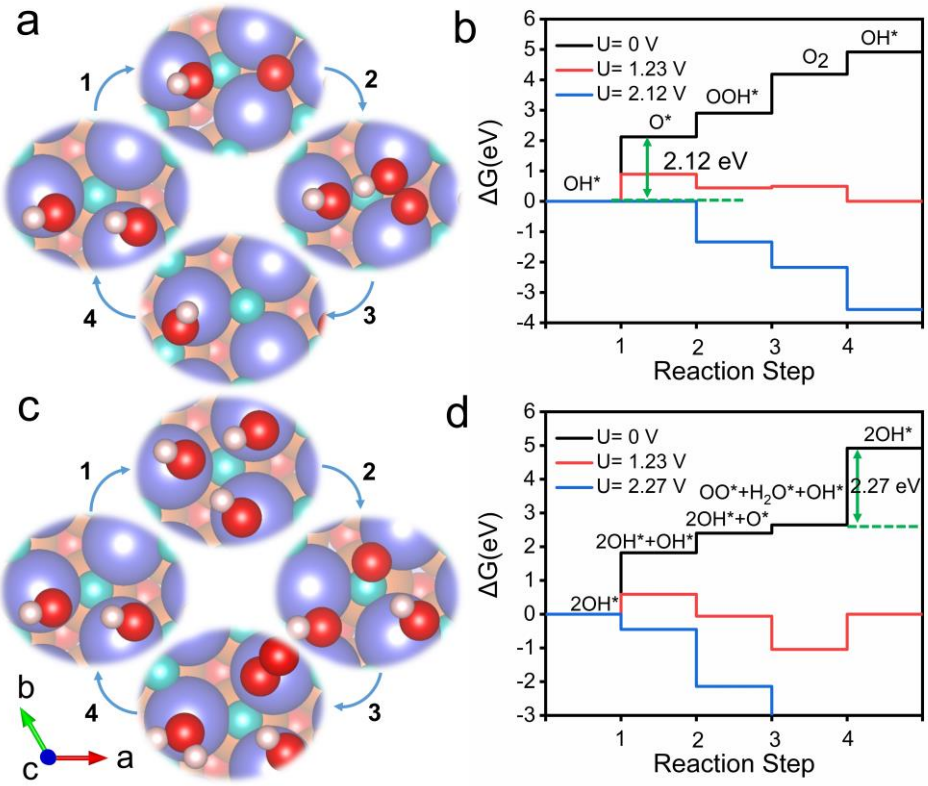

Figure 4.8. (a) OER steps and (b) Gibbs free energy diagram for the 2/3 ML OH* covered $InSnO_2N$ (001) surface with positively polarized bulk considering OH* as starting site. (c)

OER steps and (d) Gibbs free energy diagram for the 2/3 ML OH* covered $InSnO_2N$ (001) surface with positively polarized bulk considering the top of Sn top site as starting site.

4.3.3 Effect of polarization switching on OER

Based on the above, neither of the two polarization directions alone are particularly promising for OER. However, the different potentials determining steps for surfaces with opposite bulk polarization suggest that switching of the polarization direction could be used to enhance the OER activity. Such an enhanced pathway on the clean surface is shown in Figure 4.9a, where first, one H_2O molecule is deprotonated, leading to an OH

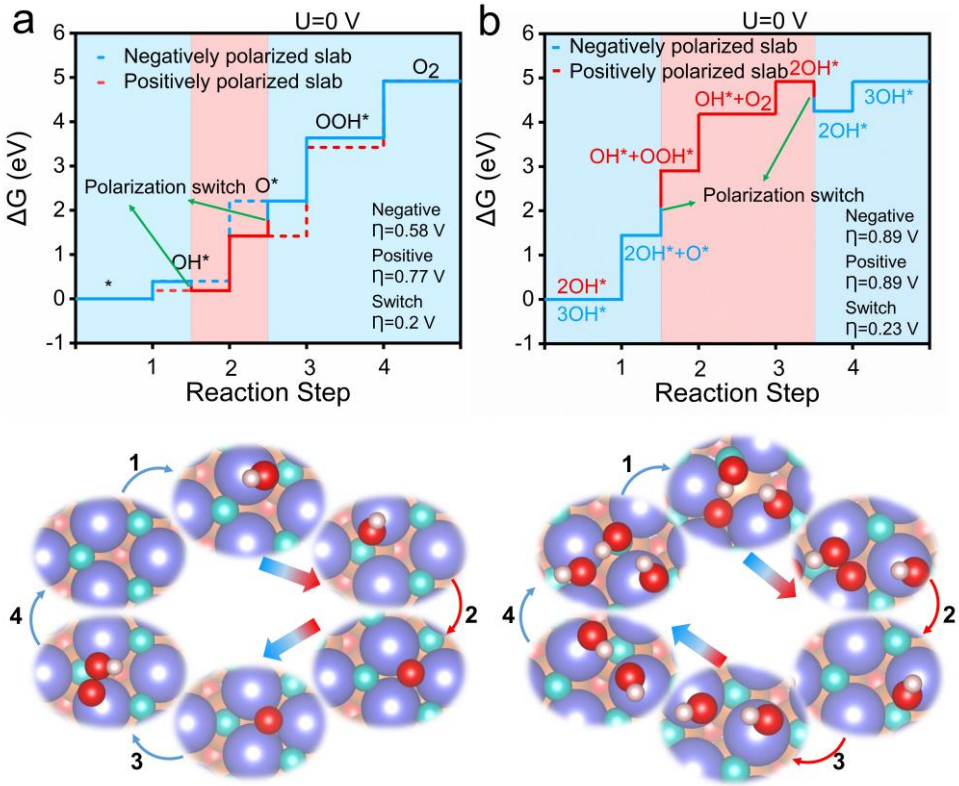

Figure 4.9. Gibbs free energy diagrams and OER steps including polarization switching for (a) the clean $InSnO_2N$ (001) surface and (b) the OH* covered $InSnO_2N$ (001) surface. The arrows indicate switching of the polarization direction.

fragment adsorbed on the surface with negatively polarized bulk. Then the polarization is switched and the OH fragment is adsorbed on the surface with positive polarization before being deprotonated to O. Afterwards the polarization direction is switched again to negative and a deprotonated H_2O molecule associates with the O to form an OOH on the surface. The OOH is then deprotonated and forms an O_2 molecule that leaves from the surface in step 4. The potential determining step of this process is the formation of OOH with a free energy change of 1.43 eV, corresponding to a theoretical overpotential of only 0.20 V. The theoretical overpotential is largely decreased, compared to that of the clean surface with negatively (0.58 V) or positively (0.77 V) polarized bulk.

Under operating condition, the change of the bulk polarization direction could also be useful to enhance the OER activity. As shown in Figure 4.9b, in step 1, for the 1ML OH covered surface with negatively polarized bulk, the OER happens on one of the OH, which is deprotonated to O. The polarization direction can then be changed to positive. In this state a sub-ML coverage of OH is preferred and we assume that one OH desorbs from the surface and then forms OOH with the O adsorbate. This OOH is then deprotonated and desorbs as O_2 before the OH coverage is restored after a further polarization switch. This OER process is limited by the formation of OOH and the potential needed for all steps to be downhill is 1.46 V, which corresponds to a theoretical overpotential of only 0.23 V.

The above enhancement of the OER activity relies on switching the polarization direction twice throughout the catalytic cycle, which is associated with an energetic cost. Based on the data in Figure 4.1b, switching amounts to an energetic cost of 5.5 meV/atom or 27.5 meV per formula unit having one Sn reactive site. During one OER cycle we thus need to provide 55 meV for the switching. We note that this analysis considers homogeneous switching of the ferroelectric, whereas a domain-mediated mechanism usually leads to a smaller energetic cost in non-2D or ultrathin ferroelectrics.[216] We also neglect the fact that surface adsorbates will slightly affect the switching barrier but expect this effect to cancel to a large extent for the two polarization switches, since one barrier will increase, while the one of the reverse switch is decreased.[217] Despite these approximations, we expect the above estimation to yield a good upper-bound estimate of the involved energetic costs. One performance metric for a dynamic switched catalyst is the thermodynamic efficiency,[218] defined in our case as the ratio of the free-energy change of the largest OER step and the energetic cost of the ferroelectric switching, i.e. (0.58 eV - 0.20 eV) / 0.055 eV = 6.9 for the clean surface and (0.89 eV – 0.23 eV) / 0.055 eV = 12 for the adsorbate covered

surface, respectively. These ratios show that the reduction of the OER free energy profile by far outweighs the cost for polarization switching. Enhanced turnover frequencies compared to the steady state represent another possible switching-frequency dependent performance metric for dynamic catalysts,[218] which unfortunately are not readily available in our thermochemical DFT framework. Nevertheless, we note that ferroelectric hexagonal manganite oxides such as $ErMnO_3$, were shown to be switchable in a frequency range from 0.1 to 1000 Hz,[219] which covers the optimally resonant range for typical catalytic reactions such as formic acid oxidation[220] and should allow the practical implementation of switched $InSnO_2N$ ferroelectric photocatalysts. Morever, it is also suitable for the large-scale catalyst with numerous active sites although the reaction steps of each active site are not synchronized usually. When the overpotential is larger than the needed value, the reaction will stop, and the fragments will "pile up". The reaction will restart until the polarization direction is flipped which would enable a self-syncronization of the active sites.

4.4 Summary

In this chapter, we have theoretically investigated the effect of surface ferroelectric switching on the OER performance of the improper ferroelectric $InSnO_2N$ by means of DFT calculations. For the clean surface, the surface with negatively polarized bulk has a lower theoretical overpotential of 0.58 V, compared with the surface with positively polarized bulk (0.77 V), which is related to the increased surface electrons density. Under (photo)-electrochemical operating condition, the surface with negatively polarized bulk prefers to be covered with 1 ML OH, while for the positively polarized bulk, the surface covered with 2/3 ML OH is most stable. The theoretical overpotential for the OER on the surface with negative polarized bulk is 0.89 V which is same as the one with positively polarized bulk. When the polarization direction is switched during the OER, a lower theoretical overpotential as low as 0.20 V is observed for the clean surface and 0.23 V for the surface with OH coverage, which is far below the minimum theoretical overpotential for oxides (0.37 V). Moreover the reduction in reaction free energy is larger by a factor 6 to 12 compared to the estimated energetic cost for polarization switching. This suggests that switching the improper ferroelectric polarization direction is a valuable path towards optimizing ferroelectric OER catalysts.

Other works not included in this thesis.

In addition to the investigation on OER in oxynitride catalysts, I have also carried out other researches on energy conversion during my three-year PhD study.

1) From above study we have investigated the polarization influence on the OER. Since polarization can be applied to reduce the carrier recombination and also affect the surface reaction. It is vital to find more new materials with polarization for application of solar energy. As co-supervisor, I work with Alexandra C. Ludvigsen and Ivano E. Castelli to discover new photoferroic materials using autonomous workflow in the framework of DFT simulations. The results have been summarized and the related manuscript has been prepared to submit.
2) Using DFT calculations, the defects in the functional materials have been investigated. The intrinsic point defects in Cesium copper halides have been explored by calculating their formation energies and charge transition level, and this work has been published (**Lan, Z.**, Meng, J, Zheng K, et al. Exploring the Intrinsic Point Defects in Cesium Copper Halides. J. Phys. Chem. C 2021, 125, 1592-1598.). Cooperating with experiment group, the defects effects on Mn-doped halide perovskite quantum dots have been studied, and this work has been published (Meng, J.†, **Lan, Z.**†, Abdellah, M.,et al. Modulating Charge-Carrier Dynamics in Mn-Doped All-Inorganic Halide Perovskite Quantum Dots through the Doping-Induced Deep Trap States. J. Phys. Chem. Lett. 2020, 11, 3705–3711.). Besides, another research cooperated with experiment is to investigate the oxygen vacancy in WO_3. This study shows that the formation of step reconstruction is due to the oxygen vacancy. This work has been published (Meng, J. †, **Lan, Z.**†, Castelli I E, et al. Atomic-Scale Observation of Oxygen Vacancy-Induced Step Reconstruction in WO_3. J. Phys. Chem. C 2021, 125, 8456-8460.).

Chapter 5

Conclusion and Outlook

5.1 Conclusion

In this thesis, basing on DFT calculation, doping, strain and polarization engineering have been studied to modulate the OER in oxynitride materials. Our results show that that strain and doping can be used to modify the surface properties to improve the electrocatalytic properties to the minimum predicted theoretical overpotential. Switching the polarization direction during OER process can overcome the foundational limitation due to Sabatier principle and further improve the electrocatalytic performance.

1) The roles of anion ordering, strain and doping modification in OER of $BaTaO_2N$ have been studied. For the (001) TaON-terminated surface of $BaTaO_2N$, the theoretical overpotential is 1.64 V which is much larger than the (100) TaO_2N-terminated surface due to different anion ordering. Under realistic (photo-)electrochemical conditions, 1% tensile uniaxial strain in the [001] direction can lower the theoretical overpotential to 0.37 V from 0.43 V for the full oxygen-covered TaO_2N-terminated surface. While 4% compressive uniaxial strain in the [010] direction can lower the theoretical overpotential to 0.59 V from 0.78 V for the full OH-coverage TaON-terminated surface. For the clean (001) TaON-terminated surface, the theoretical overpotential can be reduced from 0.97 to 0.90 V by replacing a sublayer Ba with Sr and it is further reduced to 0.88 V when a sublayer Ba was replaced by Ca. Moreover, combing with 4% tensile uniaxial strain in the [010] direction, the Ca-doping can lower theoretical overpotential to 0.53 V for TaON-terminated (001) clean surface.
2) The OER performance of $InSnO_2N$ surfaces with negatively/positively polarized bulk has been investigated. For the clean surface with a downward (negatively) polarized bulk, the theoretical overpotential is 0.58 V is lower than the clean surface with an upward (positively) polarized bulk (0.77 V). If the polarization direction is

flipped during the OER, for the clean surface, theoretical overpotential can be greatly reduced to 0.20 V. Under (photo)-electrochemical operating conditions, for the negatively polarized bulk, the surface with a 1 monolayer (ML) OH coverage is the most stable while for the positively polarized bulk, the surface is preferred to be covered with a 2/3 ML OH. For the OH-covered surfaces with negatively and positively polarized bulk, they have same value of overpotentials of 0.89 V. When switching the polarization direction during the OER, this value can be lowered to 0.23 V, which is far below the minimum theoretical overpotential for oxides (0.37 V).

5.2 Outlook

The findings in this project point to several possible researches that can enrich the exploration of (photo-)electrochemical reaction activities.

1) The study of the OER of $BaTaO_2N$ shows that the OER performance varies for different facets, and the strain and doping modifications behave differently on different surfaces. Hence, it is possible to study OER on a series of perovskite oxynitrides surfaces with different anion orderings to find out how the surface nitrogen distribution influences the surface reaction activity. Moreover, it will be worth to carry out the strain and doping engineering on the surface to enhance the OER performance in oxynitride catalysts.
2) The investigation of the OER performance of $InSnO_2N$ surfaces with improper ferroelectricity represents that switching of polarization is a highly promising route to boost the OER activity. The strain can be applied to change the surface polarization of the ferroelectric $InSnO_2N$, and hence modulate the surface reaction. Thus, the effect of the strain on the OER performance in the ferroelectric $InSnO_2N$ is also a meaningful research. What's more, other kinds of catalytic processes, like CO oxidation and NO reduction can also be investigated on the polarized surface and the reaction can be optimized by flipping the polarization direction during the catalytic process. Another interesting idea is to utilize the polarization of the polar substrate. Then the OER on the non-polar surface with polar substrate can be modified by switching the polarization direction of the substrate.

Reference

(1) Ahuja, S. Food, Energy, and Water; Elsevier, 2015.

(2) Ellabban, O.; Abu-Rub, H.; Blaabjerg, F. Renewable Energy Resources: Current Status, Future Prospects and Their Enabling Technology. *Renew. Sustain. Energy Rev.* **2014**, *39*, 748–764.

(3) Dincer, I. Comprehensive Energy Systems; Elsevier, 2018.

(4) Fujishima, A.; Honda, K. Electrochemical Photolysis of Water at a Semiconductor Electrode. *Nature* **1972**, *238*, 37–38.

(5) Sakar; Prakash; Do. Insights into the TiO_2-Based Photocatalytic Systems and Their Mechanisms. *Catalysts* **2019**, *9*, 680.

(6) Zou, Z.; Ye, J.; Sayama, K.; Arakawa, H. Direct Splitting of Water under Visible Light Irradiation with an Oxide Semiconductor Photocatalyst. *Nature* **2001**, *414*, 625–627.

(7) Wenderich, K.; Mul, G. Methods, Mechanism, and Applications of Photodeposition in Photocatalysis: A Review. *Chemical Reviews*. 2016, *116*, 14587–14619.

(8) Serpone, N.; Emeline, A. V.; Horikoshi, S.; Kuznetsov, V. N.; Ryabchuk, V. K. On the Genesis of Heterogeneous Photocatalysis: A Brief Historical Perspective in the Period 1910 to the Mid-1980s. *Photochem. Photobiol. Sci.* **2012**, *11*, 1121.

(9) Serpone, N.; Emeline, A. V. Semiconductor Photocatalysis–Past, Present, and Future Outlook. *J. Phys. Chem. Lett.* **2012**, *3*, 673–677.

(10) Ganguly, P.; Panneri, S.; Hareesh, U. S.; Breen, A.; Pillai, S. C. Recent Advances in Photocatalytic Detoxification of Water. In *Nanoscale Materials in Water Purification*; Elsevier, 2019; pp 653–688.

(11) Https://Www.Energy.Gov/Eere/Fuelcells/Hydrogen-Production-Thermochemical-Water-Splitting.

(12) Valdés, Á.; Qu, Z. W.; Kroes, G. J.; Rossmeisl, J.; Nørskov, J. K. Oxidation and Photo-Oxidation of Water on TiO_2 Surface. *J. Phys. Chem. C* **2008**, *112*, 9872–9879.

(13) Varghese, O. K.; Grimes, C. A. Appropriate Strategies for Determining the Photoconversion Efficiency of Water Photoelectrolysis Cells: A Review with Examples Using Titania Nanotube Array Photoanodes. *Sol. Energy Mater. Sol. Cells* **2008**, *92*, 374–384.

(14) Lu, Q.; Yu, Y.; Ma, Q.; Chen, B.; Zhang, H. 2D Transition-Metal-Dichalcogenide-Nanosheet-Based Composites for Photocatalytic and Electrocatalytic Hydrogen Evolution Reactions. *Adv. Mater.* **2016**, *28*, 1917–1933.

(15) Hellman, A.; Iandolo, B.; Wickman, B.; Grönbeck, H.; Baltrusaitis, J. Electro-Oxidation of Water on Hematite: Effects of Surface Termination and Oxygen Vacancies Investigated by First-Principles. *Surf. Sci.* **2015**, *640*, 45–49.

(16) Hellman, A.; Pala, R. G. S. First-Principles Study of Photoinduced Water-Splitting on Fe_2O_3. *J. Phys. Chem. C* **2011**, *115*, 12901–12907.

(17) Persson, K. A.; Waldwick, B.; Lazic, P.; Ceder, G. Prediction of Solid-Aqueous Equilibria: Scheme to Combine First-Principles Calculations of Solids with Experimental Aqueous States. *Phys. Rev. B* **2012**, *85*, 235438.

(18) Hansen, H. A.; Rossmeisl, J.; Nørskov, J. K. Surface Pourbaix Diagrams and Oxygen Reduction Activity of Pt, Ag and Ni(111) Surfaces Studied by DFT. *Phys. Chem. Chem. Phys.* **2008**, *10*, 3722.

(19) Pourbaix, M. Atlas of Electrochemical Equilibria in Aqueous Solutions*, Second English Edition*; 1974.

(20) Huang, L. F.; Rondinelli, J. M. Electrochemical Phase Diagrams for Ti Oxides from Density Functional Calculations. *Phys. Rev. B* **2015**, *92*, 245126.

(21) Bockris, J. O. M. Kinetics of Activation Controlled Consecutive Electrochemical Reactions: Anodic Evolution of Oxygen. *J. Chem. Phys.* **1956**, *24*, 817–827.

(22) Scheuermann, A. G.; Prange, J. D.; Gunji, M.; Chidsey, C. E. D.; McIntyre, P. C. Effects of Catalyst Material and Atomic Layer Deposited TiO_2 Oxide Thickness on the Water Oxidation Performance of Metal–Insulator–Silicon Anodes. *Energy Environ. Sci.* **2013**, *6*, 2487.

(23) Matsumoto, Y.; Sato, E. Electrocatalytic Properties of Transition Metal Oxides for Oxygen Evolution Reaction. *Mater. Chem. Phys.* **1986**, *14*, 397–426.

(24) Rossmeisl, J.; Qu, Z. W.; Zhu, H.; Kroes, G. J.; Nørskov, J. K. Electrolysis of Water on Oxide Surfaces. *J. Electroanal. Chem.* **2007**, *607*, 83–89.

(25) Reier, T.; Nong, H. N.; Teschner, D.; Schlögl, R.; Strasser, P. Electrocatalytic Oxygen Evolution Reaction in Acidic Environments–Reaction Mechanisms and Catalysts. *Adv. Energy Mater.* **2017**, *7*, 1601275.

(26) Man, I. C.; Su, H.; Calle–Vallejo, F.; Hansen, H. A.; Martínez, J. I.; Inoglu, N. G.; Kitchin, J.; Jaramillo, T. F.; Nørskov, J. K.; Rossmeisl, J. Universality in Oxygen Evolution Electrocatalysis on Oxide Surfaces. *ChemCatChem* **2011**, *3*, 1159–1165.

(27) Hurum, D. C.; Agrios, A. G.; Gray, K. A.; Rajh, T.; Thurnauer, M. C. Explaining the Enhanced Photocatalytic Activity of Degussa P25 Mixed-Phase TiO_2 Using EPR. *J. Phys. Chem. B* **2003**, *107*, 4545–4549.

(28) Morgade, C. I. N.; Castellani, N. J.; Cabeza, G. F. Theoretical Analysis of Band Alignment and Charge Carriers Migration in Mixed-Phase TiO_2 Systems. *J. Comput. Electron.* **2018,** *17*, 1505-1514.

(29) Luo, W.; Yang, Z.; Li, Z.; Zhang, J.; Liu, J.; Zhao, Z.; Wang, Z.; Yan, S.; Yu, T.; Zou, Z. Solar Hydrogen Generation from Seawater with a Modified $BiVO_4$ Photoanode. *Energy Environ. Sci.* **2011**, *4*, 4046.

(30) Li, P.; Chen, X.; He, H.; Zhou, X.; Zhou, Y.; Zou, Z. Polyhedral 30-Faceted $BiVO_4$ Microcrystals Predominantly Enclosed by High-Index Planes Promoting Photocatalytic Water-Splitting Activity. *Adv. Mater.* **2018**, *30*, 1703119.

(31) Thalluri, S. M.; Martinez Suarez, C.; Hernández, S.; Bensaid, S.; Saracco, G.; Russo, N. Elucidation of Important Parameters of $BiVO_4$ Responsible for Photo-Catalytic O_2 Evolution and Insights about the Rate of the Catalytic Process. *Chem. Eng. J.* **2014**, *245*, 124–132.

(32) Huang, Z. F.; Song, J.; Pan, L.; Zhang, X.; Wang, L.; Zou, J. J. Tungsten Oxides for Photocatalysis, Electrochemistry, and Phototherapy. *Advanced Materials*. 2015, 27, *5309-5327*.

(33) Pihosh, Y.; Turkevych, I.; Mawatari, K.; Asai, T.; Hisatomi, T.; Uemura, J.; Tosa, M.; Shimamura, K.; Kubota, J.; Domen, K.; et al. Nanostructured WO_3/$BiVO_4$ Photoanodes for Efficient Photoelectrochemical Water Splitting. *Small* **2014**, *10*, 3692–3699.

(34) Rettie, A. J. E.; Klavetter, K. C.; Lin, J.-F.; Dolocan, A.; Celio, H.; Ishiekwene, A.; Bolton, H. L.; Pearson, K. N.; Hahn, N. T.; Mullins, C. B. Improved Visible Light Harvesting of WO_3 by Incorporation of Sulfur or Iodine: A Tale of Two Impurities. *Chem. Mater.* **2014**, *26*, 1670–1677.

(35) Rao, P. M.; Cai, L.; Liu, C.; Cho, I. S.; Lee, C. H.; Weisse, J. M.; Yang, P.; Zheng, X. Simultaneously Efficient Light Absorption and Charge Separation in WO_3 /$BiVO_4$ Core/Shell Nanowire Photoanode for Photoelectrochemical Water Oxidation. *Nano Lett.* **2014**, *14*, 1099–1105.

(36) Fan, X.; Gao, B.; Wang, T.; Huang, X.; Gong, H.; Xue, H.; Guo, H.; Song, L.; Xia, W.; He, J. Layered Double Hydroxide Modified WO_3 Nanorod Arrays for Enhanced Photoelectrochemical Water Splitting. *Appl. Catal. A Gen.* **2016**, *528*, 52–58.

(37) Xie, Y. P.; Liu, G.; Yin, L.; Cheng, H.-M. Crystal Facet-Dependent Photocatalytic Oxidation and Reduction Reactivity of Monoclinic WO_3 for Solar Energy Conversion. *J. Mater. Chem.* **2012**, *22*, 6746.

(38) Newton, K. A.; Osterloh, F. E. Size and Morphology of Suspended WO_3 Particles Control Photochemical Charge Carrier Extraction and Photocatalytic Water Oxidation Activity. *Top. Catal.* **2016**, *59*, 750–756.

(39) Zhang, S.; Xu, W.; Zeng, M.; Li, J.; Xu, J.; Wang, X. Hierarchically Grown CdS/α-Fe_2O_3 Heterojunction Nanocomposites with Enhanced Visible-Light-Driven Photocatalytic Performance. *Dalt. Trans.* **2013**, *42*, 13417.

(40) Saha, S.; Kumar, J. S.; Chandra Murmu, N.; Samanta, P.; Kuila, T. Controlled Electrodeposition of Iron Oxide/Nickel Oxide@Ni for the Investigation of the Effects of Stoichiometry and Particle Size on Energy Storage and Water Splitting Applications. *J. Mater. Chem. A* **2018**, *6*, 9657–9664.

(41) Xu, L.; Xia, J.; Wang, K.; Wang, L.; Li, H.; Xu, H.; Huang, L.; He, M. Ionic Liquid Assisted Synthesis and Photocatalytic Properties of α-Fe_2O_3 Hollow Microspheres. *Dalt. Trans.* **2013**, *42*, 6468.

(42) Liu, G.; Deng, Q.; Wang, H.; Ng, D. H. L.; Kong, M.; Cai, W.; Wang, G. Micro /Nanostructured α-Fe_2O_3 Spheres: Synthesis, Characterization, and Structurally Enhanced Visible-Light Photocatalytic Activity. *J. Mater. Chem.* **2012**, *22*, 9704.

(43) She, X.; Wu, J.; Xu, H.; Zhong, J.; Wang, Y.; Song, Y.; Nie, K.; Liu, Y.; Yang, Y.; Rodrigues, M. T. F.; et al. High Efficiency Photocatalytic Water Splitting Using 2D α-Fe_2O_3 /g-C_3N_4 Z-Scheme Catalysts. *Adv. Energy Mater.* **2017**, *7*, 1700025.

(44) Wang, J.; Zhang, N.; Su, J.; Guo, L. α-Fe_2O_3 Quantum Dots: Low-Cost Synthesis and Photocatalytic Oxygen Evolution Capabilities. *RSC Adv.* **2016**, *6*, 41060–41066.

(45) Fuertes, A. Metal Oxynitrides as Emerging Materials with Photocatalytic and Electronic Properties. *Mater. Horizons* **2015**, *2*, 453–461.

(46) Moriya, Y.; Takata, T.; Domen, K. Recent Progress in the Development of (Oxy)Nitride Photocatalysts for Water Splitting under Visible-Light Irradiation. *Coord. Chem. Rev.* **2013**, *257*, 1957–1969.

(47) Fuertes, A. Synthesis and Properties of Functional Oxynitrides–from Photocatalysts to CMR Materials. *Dalt. Trans.* **2010**, *39*, 5942.

(48) Ebbinghaus, S. G.; Abicht, H.-P.; Dronskowski, R.; Müller, T.; Reller, A.; Weidenkaff, A. Perovskite-Related Oxynitrides–Recent Developments in Synthesis, Characterisation and Investigations of Physical Properties. *Prog. Solid State Chem.* **2009**, *37*, 173–205.

(49) Fuertes, A. Chemistry and Applications of Oxynitride Perovskites. *J. Mater. Chem.* **2012**, *22*, 3293.

(50) Xie, R. J.; Bert Hintzen, H. T. Optical Properties of (Oxy)Nitride Materials: A Review. *J. Am. Ceram. Soc.* **2013**, *96*, 665–687.

(51) Attfield, J. P.; Lightfoot, P.; Morris, R. E. Perovskites. *Dalt. Trans.* **2015**, *44*, 10541–10542.

(52) Peña, M. A.; Fierro, J. L. G. Chemical Structures and Performance of Perovskite Oxides. *Chem. Rev.* **2001**, *101*, 1981–2018.

(53) Zulueta, Y. A.; Lim, T. C.; Dawson, J. A. Defect Clustering in Rare-Earth-Doped $BaTiO_3$ and $SrTiO_3$ and Its Influence on Dopant Incorporation. *J. Phys. Chem. C* **2017**, *121*, 23642–23648.

(54) Shi, J.; Guo, L. ABO_3-Based Photocatalysts for Water Splitting. *Prog. Nat. Sci. Mater. Int.* **2012**, *22*, 592–615.

(55) Marchand, R. Oxynitrides with Potassium Nickel (II) Tetrafluoride Structure. Ln_2AlO_3N Compounds (Ln= Lanthanum, Neodymium, Samarium). *CR Acad. Sci. C* **1976**, *282*, 329–331.

(56) Bacher, P.; Antoine, P.; Marchand, R.; L'Haridon, P.; Laurent, Y.; Roult, G. Time-of-Flight Neutron Diffraction Study of the Structure of the Perovskite-Type Oxynitride $LaWO_{0.6}N_{2.4}$. *J. Solid State Chem.* **1988**, *77*, 67–71.

(57) Oró-Solé, J.; Clark, L.; Kumar, N.; Bonin, W.; Sundaresan, A.; Attfield, J. P.; Rao, C. N. R.; Fuertes, A. Synthesis, Anion Order and Magnetic Properties of $RVO_{3-x}N_x$ Perovskites (R = La, Pr, Nd; $0 \leq x \leq 1$). *J. Mater. Chem. C* **2014**, *2*, 2212.

(58) Yang, M.; Oró-Solé, J.; Rodgers, J. A.; Jorge, A. B.; Fuertes, A.; Attfield, J. P. Anion Order in Perovskite Oxynitrides. *Nat. Chem.* **2011**, *3*, 47–52.

(59) Oró-Solé, J.; Clark, L.; Bonin, W.; Attfield, J. P.; Fuertes, A. Anion-Ordered Chains in a D1 Perovskite Oxynitride: $NdVO_2N$. *Chem. Commun.* **2013**, *49*, 2430.

(60) Hinuma, Y.; Moriwake, H.; Zhang, Y. R.; Motohashi, T.; Kikkawa, S.; Tanaka, I. First-Principles Study on Relaxor-Type Ferroelectric Behavior without Chemical Inhomogeneity in $BaTaO_2N$ and $SrTaO_2N$. *Chem. Mater.* **2012**, *24*, 4343–4349.

(61) Page, K.; Stoltzfus, M. W.; Kim, Y. I.; Proffen, T.; Woodward, P. M.; Cheetham, A. K.; Seshadri, R. Local Atomic Ordering in $BaTaO_2N$ Studied by Neutron Pair Distribution Function Analysis and Density Functional Theory. *Chem. Mater.* **2007**, *19*, 4037–4042.

(62) Wolff, H.; Dronskowski, R. First-Principles and Molecular-Dynamics Study of Structure and Bonding in Perovskite-Type Oxynitrides ABO_2N (A = Ca, Sr, Ba; B = Ta, Nb). *J. Comput. Chem.* **2008**, *29*, 2260–2267.

(63) Poloni, R.; Íñiguez, J.; García, A.; Canadell, E. An Efficient Computational Method for Use in Structural Studies of Crystals with Substitutional Disorder. *J. Phys. Condens. Matter* **2010**, *22*, 415401.

(64) Tobías, G.; Oró-Solé, J.; Beltrán-Porter, D.; Fuertes, A. New Family of Ruddlesden−Popper Strontium Niobium Oxynitrides: $(SrO)(SrNbO_{2-x}N)_n$ (n = 1, 2). *Inorg. Chem.* **2001**, *40*, 6867–6869.

(65) Diot, N.; Marchand, R.; Haines, J.; Léger, J. M.; Macaudière, P.; Hull, S. Crystal Structure Determination of the Oxynitride Sr_2TaO_3N. *J. Solid State Chem.* **1999**, *146*, 390–393.

(66) Tobías, G.; Beltrán-Porter, D.; Lebedev, O. I.; Van Tendeloo, G.; Rodríguez-Carvajal, J.; Fuertes, A. Anion Ordering and Defect Structure in Ruddlesden−Popper Strontium Niobium Oxynitrides. *Inorg. Chem.* **2004**, *43*, 8010–8017.

(67) Fuertes, A. Prediction of Anion Distributions Using Pauling's Second Rule. *Inorg. Chem.* **2006**, *45*, 9640–9642.

(68) Kasahara, A.; Nukumizu, K.; Hitoki, G.; Takata, T.; Kondo, J. N.; Hara, M.; Kobayashi, H.; Domen, K. Photoreactions on $LaTiO_2N$ under Visible Light Irradiation. *J. Phys. Chem. A* **2002**, *106*, 6750-6753.

(69) Balaz, S.; Porter, S. H.; Woodward, P. M.; Brillson, L. J. Electronic Structure of Tantalum Oxynitride Perovskite Photocatalysts. *Chem. Mater.* **2013**, *25*, 3337–3343.

(70) Siritanaratkul, B.; Maeda, K.; Hisatomi, T.; Domen, K. Synthesis and Photocatalytic Activity of Perovskite Niobium Oxynitrides with Wide Visible-Light Absorption Bands. *ChemSusChem* **2011**, *4*, 74–78.

(71) Hisatomi, T.; Katayama, C.; Moriya, Y.; Minegishi, T.; Katayama, M.; Nishiyama, H.; Yamada, T.; Domen, K. Photocatalytic Oxygen Evolution Using $BaNbO_2N$ Modified with Cobalt Oxide under Photoexcitation up to 740 nm. *Energy Environ. Sci.* **2013**, *6*, 3595.

(72) Hisatomi, T.; Katayama, C.; Teramura, K.; Takata, T.; Moriya, Y.; Minegishi, T.; Katayama, M.; Nishiyama, H.; Yamada, T.; Domen, K. The Effects of Preparation Conditions for a $BaNbO_2N$ Photocatalyst on Its Physical Properties. *ChemSusChem* **2014**, *7*, 2016–2021.

(73) Ahmed, M.; Xinxin, G. A Review of Metal Oxynitrides for Photocatalysis. *Inorg. Chem. Front.* **2016**, *3*, 578–590.

(74) Lottermoser, T.; Fiebig, M.; Fröhlich, D.; Leute, S.; Kohn, K. Magnetic Structure of Hexagonal Manganites $RMnO_3$ (R=Sc,Y,Ho,Er,Tm,Yb,Lu). *J. Magn. Magn. Mater.* **2001**, *226–230*, 1131–1133.

(75) Yakel Jnr, H. L.; Koehler, W. C.; Bertaut, E. F.; Forrat, E. F. On the Crystal Structure of the Manganese(III) Trioxides of the Heavy Lanthanides and Yttrium. *Acta Crystallogr.* **1963**, *16*, 957-962.

(76) Bosak, A. A.; Dubourdieu, C.; Sénateur, J. P.; Gorbenko, O. Y.; Kaul, A. R. Epitaxial Stabilization of Hexagonal $RMnO_3$ (R = Eu–Dy) Manganites. *J. Mater. Chem.* **2002**, *12*, 800–801.

(77) Hartman, S. T.; Thind, A. S.; Mishra, R. Tin Oxynitride-Based Ferroelectric Semiconductors for Solar Energy Conversion Applications. *Chem. Mater.* **2020**, *32*, 9542–9550.

(78) Stoerzinger, K. A.; Choi, W. S.; Jeen, H.; Lee, H. N.; Shao-Horn, Y. Role of Strain and Conductivity in Oxygen Electrocatalysis on $LaCoO_3$ Thin Films. *J. Phys. Chem. Lett.* **2015**, *6*, 487–492.

(79) Petrie, J. R.; Cooper, V. R.; Freeland, J. W.; Meyer, T. L.; Zhang, Z.; Lutterman, D. A.; Lee, H. N. Enhanced Bifunctional Oxygen Catalysis in Strained $LaNiO_3$ Perovskites. *J. Am. Chem. Soc.* **2016**, *138*, 2488–2491.

(80) Hammer, B.; Norskov, J. K. Why Gold Is the Noblest of All the Metals. *Nature* **1995**, *376*, 238–240.

(81) Luo, M.; Guo, S. Strain-Controlled Electrocatalysis on Multimetallic Nanomaterials. *Nat. Rev. Mater.* **2017**, *2*, 17059.

(82) Yao, Y.; Hu, S.; Chen, W.; Huang, Z. Q.; Wei, W.; Yao, T.; Liu, R.; Zang, K.; Wang, X.; Wu, G.; et al. Engineering the Electronic Structure of Single Atom Ru Sites via Compressive Strain Boosts Acidic Water Oxidation Electrocatalysis. *Nat. Catal.* **2019**, *2*, 304–313.

(83) Wang, H. F.; Tang, C.; Li, B. Q.; Zhang, Q. A Review of Anion-Regulated Multi-Anion Transition Metal Compounds for Oxygen Evolution Electrocatalysis. *Inorg. Chem. Front.* **2018**, *5*, 521–534.

(84) Montoya, J. H.; Seitz, L. C.; Chakthranont, P.; Vojvodic, A.; Jaramillo, T. F.; Nørskov, J. K. Materials for Solar Fuels and Chemicals. *Nat. Mater.* **2017**, *16*, 70–81.

(85) Seh, Z. W.; Kibsgaard, J.; Dickens, C. F.; Chorkendorff, I.; Nørskov, J. K.; Jaramillo, T. F. Combining Theory and Experiment in Electrocatalysis: Insights into Materials Design. *Science.* **2017**, *355*, eaad4998.

(86) Burke, M. S.; Kast, M. G.; Trotochaud, L.; Smith, A. M.; Boettcher, S. W. Cobalt–Iron (Oxy)Hydroxide Oxygen Evolution Electrocatalysts: The Role of Structure and Composition on Activity, Stability, and Mechanism. *J. Am. Chem. Soc.* **2015**, *137*, 3638–3648.

(87) Friebel, D.; Louie, M. W.; Bajdich, M.; Sanwald, K. E.; Cai, Y.; Wise, A. M.; Cheng, M. J.; Sokaras, D.; Weng, T. C.; Alonso-Mori, R.; et al. Identification of Highly Active Fe Sites in (Ni,Fe)OOH for Electrocatalytic Water Splitting. *J. Am. Chem. Soc.* **2015**, *137*, 1305–1313.

(88) Trotochaud, L.; Young, S. L.; Ranney, J. K.; Boettcher, S. W. Nickel–Iron Oxyhydroxide Oxygen-Evolution Electrocatalysts: The Role of Intentional and Incidental Iron Incorporation. *J. Am. Chem. Soc.* **2014**, *136*, 6744–6753.

(89) Liao, P.; Keith, J. A.; Carter, E. A. Water Oxidation on Pure and Doped Hematite (0001) Surfaces: Prediction of Co and Ni as Effective Dopants for Electrocatalysis. *J. Am. Chem. Soc.* **2012**, *134*, 13296–13309.

(90) Liu, Y.; Yu, Y. X.; Zhang, W. De. Photoelectrochemical Properties of Ni-Doped Fe_2O_3 Thin Films Prepared by Electrodeposition. *Electrochim. Acta* **2012**, *59*, 121–127.

(91) Wygant, B. R.; Jarvis, K. A.; Chemelewski, W. D.; Mabayoje, O.; Celio, H.; Mullins, C. B. Structural and Catalytic Effects of Iron- and Scandium-Doping on a Strontium Cobalt Oxide Electrocatalyst for Water Oxidation. *ACS Catal.* **2016**, *6*, 1122–1133.

(92) Cui, Y.; Briscoe, J.; Dunn, S. Effect of Ferroelectricity on Solar-Light-Driven Photocatalytic Activity of $BaTiO_3$ —Influence on the Carrier Separation and Stern Layer Formation. *Chem. Mater.* **2013**, *25*, 4215–4223.

(93) Garrity, K.; Kakekhani, A.; Kolpak, A.; Ismail-Beigi, S. Ferroelectric Surface Chemistry: First-Principles Study of the $PbTiO_3$ Surface. *Phys. Rev. B* **2013**, *88*, 045401.

(94) Kakekhani, A.; Ismail-Beigi, S. Ferroelectric-Based Catalysis: Switchable Surface Chemistry. *ACS Catal.* **2015**, *5*, 4537-4545.

(95) Ju, L.; Shang, J.; Tang, X.; Kou, L. Tunable Photocatalytic Water Splitting by the Ferroelectric Switch in a 2D $AgBiP_2Se_6$ Monolayer. *J. Am. Chem. Soc.* **2020**, *142*, 1492–1500.

(96) Lee, J. H.; Selloni, A. TiO_2/Ferroelectric Heterostructures as Dynamic Polarization-Promoted Catalysts for Photochemical and Electrochemical Oxidation of Water. *Phys. Rev. Lett.* **2014** *112*, 196102.

(97) Vonrüti, N.; Aschauer, U. Catalysis on Oxidized Ferroelectric Surfaces—Epitaxially Strained $LaTiO_2N$ and $BaTiO_3$ for Photocatalytic Water Splitting. *J. Chem. Phys.* **2020**, *152*, 024701.

(98) Maeda, K.; Domen, K. Oxynitride Materials for Solar Water Splitting. *MRS Bull.* **2011**, *36*, 25–31.

(99) Maeda, K.; Domen, K. New Non-Oxide Photocatalysts Designed for Overall Water Splitting under Visible Light. *J. Phys. Chem. C* **2007**, *111*, 7851–7861.

(100) Attfield, J. P. Principles and Applications of Anion Order in Solid Oxynitrides. *Cryst. Growth Des.* **2013**, *13*, 4623–4629.

(101) Kubo, A.; Giorgi, G.; Yamashita, K. Anion Ordering in $CaTaO_2N$: Structural Impact on the Photocatalytic Activity. Insights from First-Principles. *Chem. Mater.* **2017**, *29*, 539–545.

(102) Liu, L.; Huang, H.; Chen, F.; Yu, H.; Tian, N.; Zhang, Y.; Zhang, T. Cooperation of Oxygen Vacancies and 2D Ultrathin Structure Promoting CO_2 Photoreduction Performance of $Bi_4Ti_3O_{12}$. *Sci. Bull.* **2020**, *65*, 934–943.

(103) Li, H.; Shang, J.; Zhu, H.; Yang, Z.; Ai, Z.; Zhang, L. Oxygen Vacancy Structure Associated Photocatalytic Water Oxidation of BiOCl. *ACS Catal.* **2016**, *6*, 8276–8285.

(104) Wang, L. J.; Bai, J. Y.; Zhang, Y. J.; Mao, F.; Liu, Y.; Yuan, H.; Liu, P. F.; Yang, H. G. Controllable Synthesis of Conical $BiVO_4$ for Photocatalytic Water Oxidation. *J. Mater. Chem. A* **2020**, *8*, 2331–2335.

(105) Liu, G.; Han, J.; Zhou, X.; Huang, L.; Zhang, F.; Wang, X.; Ding, C.; Zheng, X.; Han, H.; Li, C. Enhancement of Visible-Light-Driven O_2 Evolution from Water Oxidation on WO_3 Treated with Hydrogen. *J. Catal.* **2013**, *307*, 148–152.

(106) Born, M.; Oppenheimer, R. Zur Quantentheorie Der Molekeln. *Ann. Phys.* **1927**, *389*, 457–484.

(107) Strinati, G. C. Hartree and Hartree-Fock Methods in Electronic Structure. *Encycl. Condens. Matter Phys.* **2005**, 311–318.

(108) Thomas, L. H. The Calculation of Atomic Fields. *Math. Proc. Cambridge Philos. Soc.* **1927**, *23*, 542–548.

(109) Dirac, P. A. M. Note on Exchange Phenomena in the Thomas Atom. *Math. Proc. Cambridge Philos. Soc.* **1930**, *26*, 376–385.

(110) Rajagopal, A. K.; Callaway, J. Inhomogeneous Electron Gas. *Phys. Rev. B* **1973**, *7*, 1912.

(111) Vanderbilt, D. Soft Self-Consistent Pseudopotentials in a Generalized Eigenvalue Formalism. *Phys. Rev. B* **1990**, *41*, 7892–7895.

(112) Perdew, J. P.; Burke, K.; Ernzerhof, M. Generalized Gradient Approximation Made Simple. *Phys. Rev. Lett.* **1996**, *77*, 3865–3868.

(113) Perdew, J. P.; Chevary, J. A.; Vosko, S. H.; Jackson, K. A.; Pederson, M. R.; Singh, D. J.; Fiolhais, C. Atoms, Molecules, Solids, and Surfaces: Applications of the Generalized Gradient Approximation for Exchange and Correlation. *Phys. Rev. B* **1992**, *46*, 6671–6687.

(114) Becke, A. D. Density-Functional Exchange-Energy Approximation with Correct Asymptotic Behavior. *Phys. Rev. A* **1988**, *38*, 3098–3100.

(115) Lee, C.; Yang, W.; Parr, R. G. Development of the Colle-Salvetti Correlation-Energy Formula into a Functional of the Electron Density. *Phys. Rev. B* **1988**, *37*, 785–789.

(116) Peng, Q.; Duarte, F.; Paton, R. S. Computing Organic Stereoselectivity – from Concepts to Quantitative Calculations and Predictions. *Chem. Soc. Rev.* **2016**, *45*, 6093–6107.

(117) Kresse, G.; Furthmüller, J. Efficient Iterative Schemes for Ab Initio Total-Energy Calculations Using a Plane-Wave Basis Set. *Phys. Rev. B* **1996**, *54*, 11169–11186.

(118) Kresse, G.; Furthmüller, J. Efficiency of Ab-Initio Total Energy Calculations for Metals and Semiconductors Using a Plane-Wave Basis Set. *Comput. Mater. Sci.* **1996**, *6*, 15–50.

(119) Kresse, G.; Hafner, J. Ab Initio Molecular Dynamics for Liquid Metals. *Phys. Rev. B* **1993**, *47*, 558–561.

(120) Wien, T. U.; Hauptstrage, W. Ab Initio Molecular-Dynamics Simulation of the Liquid-Metal-Amorphous-Semiconductor Transition in Germanium. *Phys. Rev. B* **1994**, *49*, 14251.

(121) Giannozzi, P.; Baroni, S.; Bonini, N.; Calandra, M.; Car, R.; Cavazzoni, C.; Ceresoli, D.; Chiarotti, G. L.; Cococcioni, M.; Dabo, I.; et al. QUANTUM ESPRESSO: A Modular and Open-Source Software Project for Quantum Simulations of Materials. *J. Phys. Condens. Matter* **2009**, *21*, 395502.

(122) Gonze, X.; Beuken, J. M.; Caracas, R.; Detraux, F.; Fuchs, M.; Rignanese, G. M.; Sindic, L.; Verstraete, M.; Zerah, G.; Jollet, F.; et al. First-Principles Computation of Material Properties: The ABINIT Software Project. *Comput. Mater. Sci.* **2002**, *25*, 478–492.

(123) Gonze, X. A Brief Introduction to the ABINIT Software Package. *Zeitschrift für Krist. - Cryst. Mater.* **2005**, *220*, 558–562.

(124) Gonze, X.; Amadon, B.; Anglade, P. M.; Beuken, J. M.; Bottin, F.; Boulanger, P.; Bruneval, F.; Caliste, D.; Caracas, R.; Côté, M.; et al. ABINIT: First-Principles Approach to Material and Nanosystem Properties. *Comput. Phys. Commun.* **2009**, *180*, 2582–2615.

(125) Gonze, X.; Jollet, F.; Abreu Araujo, F.; Adams, D.; Amadon, B.; Applencourt, T.; Audouze, C.; Beuken, J. M.; Bieder, J.; Bokhanchuk, A.; et al. Recent Developments in the ABINIT Software Package. *Comput. Phys. Commun.* **2016**, *205*, 106–131.

(126) Gonze, X.; Amadon, B.; Antonius, G.; Arnardi, F.; Baguet, L.; Beuken, J.-M.; Bieder, J.; Bottin, F.; Bouchet, J.; Bousquet, E.; et al. The Abinitproject: Impact, Environment and Recent Developments. *Comput. Phys. Commun.* **2020**, *248*, 107042.

(127) Heifets, E.; Eglitis, R. I.; Kotomin, E. A.; Kotomin, E. A.; Maier, J.; Borstel, G. Ab Initio Modeling of Surface Structure for $SrTiO_3$ Perovskite Crystals. *Phys. Rev. B - Condens. Matter Mater. Phys.* **2001**, *64*, 235417.

(128) Eglitis, R. I.; Vanderbilt, D. Ab Initio Calculations of $BaTiO_3$ and $PbTiO_3$ (001) and (011) Surface Structures. *Phys. Rev. B* **2007**, *76*, 155439.

(129) Atkins, P.; de, P. J. Atkins' Physical Chemistry, 7th Edition. *Oxford Univ. Press* **2002**.

(130) Bouri, M.; Aschauer, U. Suitability of Different Sr_2TaO_3N Surface Orientations for Photocatalytic Water Oxidation. *Chem. Mater.* **2020**, *32*, 75–84.

(131) Kikkawa, S.; Sun, S.; Masubuchi, Y.; Nagamine, Y.; Shibahara, T. Ferroelectric Response Induced in cis-Type Anion Ordered $SrTaO_2N$ Oxynitride Perovskite. *Chem. Mater.* **2016**, *28*, 1312–1317.

(132) Pan, J.; Hansen, H. A.; Vegge, T. Vanadium Oxynitrides as Stable Catalysts for Electrochemical Reduction of Nitrogen to Ammonia: The Role of Oxygen. *J. Mater. Chem. A* **2020**, *8*, 24098–24107.

(133) Fuertes, A. Metal Oxynitrides as Emerging Materials with Photocatalytic and Electronic Properties. *Mater. Horizons* **2015**, *2*, 453–461.

(134) Sivula, K.; van de Krol, R. Semiconducting Materials for Photoelectrochemical Energy Conversion. *Nat. Rev. Mater.* **2016**, *1*, 15010.

(135) Ueda, K.; Minegishi, T.; Clune, J.; Nakabayashi, M.; Hisatomi, T.; Nishiyama, H.; Katayama, M.; Shibata, N.; Kubota, J.; Yamada, T.; et al. Photoelectrochemical Oxidation of Water Using $BaTaO_2N$ Photoanodes Prepared by Particle Transfer Method. *J. Am. Chem. Soc.* **2015**, *137*, 2227–2230.

(136) Jadhav, S.; Hasegawa, S.; Hisatomi, T.; Wang, Z.; Seo, J.; Higashi, T.; Katayama, M.; Minegishi, T.; Takata, T.; Peralta-Hernández, J. M.; et al. Efficient Photocatalytic Oxygen Evolution Using $BaTaO_2N$ Obtained from Nitridation of Perovskite-Type Oxide. *J. Mater. Chem. A* **2020**, *8*, 1127–1130.

(137) Maeda, K.; Domen, K. Preparation of $BaZrO_3$–$BaTaO_2N$ Solid Solutions and the Photocatalytic Activities for Water Reduction and Oxidation under Visible Light. *J. Catal.* **2014**, *310*, 67–74.

(138) Hafez, A. M.; Salem, N. M.; Allam, N. K. Unravelling the Correlated Electronic and Optical Properties of $BaTaO_2N$ with Perovskite-Type Structure as a Potential Candidate for Solar Energy Conversion. *Phys. Chem. Chem. Phys.* **2014**, *16*, 18418–18424.

(139) Seo, J.; Nakabayashi, M.; Hisatomi, T.; Shibata, N.; Minegishi, T.; Domen, K. Solar-Driven Water Splitting over a $BaTaO_2N$ Photoanode Enhanced by Annealing in Argon. *ACS Appl. Energy Mater.* **2019**, *2*, 5777–5784.

(140) Higashi, M.; Domen, K.; Abe, R. Fabrication of an Efficient $BaTaO_2N$ Photoanode Harvesting a Wide Range of Visible Light for Water Splitting. *J. Am. Chem. Soc.* **2013**, *135*, 10238–10241.

(141) Maeda, K.; Lu, D.; Domen, K. Oxidation of Water under Visible-Light Irradiation over Modified $BaTaO_2N$ Photocatalysts Promoted by Tungsten Species. *Angew. Chemie Int. Ed.* **2013**, *52*, 6488–6491.

(142) Vonrüti, N.; Aschauer, U. Anion Order and Spontaneous Polarization in $LaTiO_2N$ Oxynitride Thin Films. *Phys. Rev. Lett.* **2018**, *120*, 046001.

(143) Kubo, A.; Giorgi, G.; Yamashita, K. $MgTaO_2N$ Photocatalysts: Perovskite versus Ilmenite Structure. A Theoretical Investigation. *J. Phys. Chem. C* **2017**, *121*, 27813–27821.

(144) Kim, Y. I.; Woodward, P. M.; Baba-Kishi, K. Z.; Tai, C. W. Characterization of the Structural, Optical, and Dielectric Properties of Oxynitride Perovskites AMO_2N (A = Ba, Sr, Ca; M = Ta, Nb). *Chem. Mater.* **2004**, *16*, 1267–1276.

(145) Luo, Y.; Suzuki, S.; Wang, Z.; Yubuta, K.; Vequizo, J. J. M.; Yamakata, A.; Shiiba, H.; Hisatomi, T.; Domen, K.; Teshima, K. Construction of Spatial Charge Separation Facets on $BaTaO_2N$ Crystals by Flux Growth Approach for Visible-Light-Driven H_2 Production. *ACS Appl. Mater. Interfaces* **2019**, *11*, 22264–22271.

(146) Wang, W.; Xu, M.; Xu, X.; Zhou, W.; Shao, Z. Perovskite Oxide Based Electrodes for High–Performance Photoelectrochemical Water Splitting. *Angew. Chemie Int. Ed.* **2020**, *59*, 136–152.

(147) You, B.; Tang, M. T.; Tsai, C.; Abild-Pedersen, F.; Zheng, X.; Li, H. Enhancing Electrocatalytic Water Splitting by Strain Engineering. *Adv. Mater.* **2019**, *31*, 1807001.

(148) Yuan, J.; Wang, C.; Liu, Y.; Wu, P.; Zhou, W. Tunable Photocatalytic HER Activity of Single-Layered TiO_2 Nanosheets with Transition-Metal Doping and Biaxial Strain. *J. Phys. Chem. C* **2019**, *123*, 526–533.

(149) Lawley, C.; Nachtegaal, M.; Stahn, J.; Roddatis, V.; Döbeli, M.; Schmidt, T. J.; Pergolesi, D.; Lippert, T. Examining the Surface Evolution of $LaTiO_xN_y$ an Oxynitride Solar Water Splitting Photocatalyst. *Nat. Commun.* **2020**, *11*, 1728.

(150) Higashi, M.; Yamanaka, Y.; Tomita, O.; Abe, R. Fabrication of Cation-Doped $BaTaO_2N$ Photoanodes for Efficient Photoelectrochemical Water Splitting under Visible Light Irradiation. *APL Mater.* **2015**, *3*, 104418.

(151) Zhang, H.; Wei, S.; Xu, X. Mg Modified $BaTaO_2N$ as an Efficient Visible-Light-Active Photocatalyst for Water Oxidation. *J. Catal.* **2020**, *383*, 135–143.

(152) Cao, N.; Chen, Z.; Zang, K.; Xu, J.; Zhong, J.; Luo, J.; Xu, X.; Zheng, G. Doping Strain Induced bi-Ti^{3+} Pairs for Efficient N_2 Activation and Electrocatalytic Fixation. *Nat. Commun.* **2019**, *10*, 2877.

(153) Johnston, H.; Black, A. P.; Kayser, P.; Oró-Solé, J.; Keen, D. A.; Fuertes, A.; Attfield, J. P. Dimensional Crossover of Correlated Anion Disorder in Oxynitride Perovskites. *Chem. Commun.* **2018**, *54*, 5245–5247.

(154) Yamamoto, T.; Chikamatsu, A.; Kitagawa, S.; Izumo, N.; Yamashita, S.; Takatsu, H.; Ochi, M.; Maruyama, T.; Namba, M.; Sun, W.; et al. Strain-Induced Creation and Switching of Anion Vacancy Layers in Perovskite Oxynitrides. *Nat. Commun.* **2020**, *11*, 5923.

(155) Kim, Y. I.; Si, W.; Woodward, P. M.; Sutter, E.; Park, S.; Vogt, T. Epitaxial Thin-Film Deposition and Dielectric Properties of the Perovskite Oxynitride $BaTaO_2N$. *Chem. Mater.* **2007**, *19*, 618–623.

(156) Oka, D.; Hirose, Y.; Kamisaka, H.; Fukumura, T.; Sasa, K.; Ishii, S.; Matsuzaki, H.; Sato, Y.; Ikuhara, Y.; Hasegawa, T. Possible Ferroelectricity in Perovskite Oxynitride $SrTaO_2N$ Epitaxial Thin Films. *Sci. Rep.* **2015**, *4*, 4987.

(157) Bubeck, C.; Widenmeyer, M.; De Denko, A. T.; Richter, G.; Coduri, M.; Colera, E. S.; Goering, E.; Zhang, H.; Yoon, S.; Osterloh, F. E.; et al. Bandgap-Adjustment and Enhanced Surface Photovoltage in Y-Substituted $LaTa^{IV}O_2N$. *J. Mater. Chem. A* **2020**, *8*, 11837–11848.

(158) Maegli, A. E.; Pokrant, S.; Hisatomi, T.; Trottmann, M.; Domen, K.; Weidenkaff, A. Enhancement of Photocatalytic Water Oxidation by the Morphological Control of $LaTiO_2N$ and Cobalt Oxide Catalysts. *J. Phys. Chem. C* **2014**, *118*, 16344–16351.

(159) Kim, Y.; Watanabe, M.; Matsuda, J.; Song, J. T.; Takagaki, A.; Staykov, A.; Ishihara, T. Tensile Strain for Band Engineering of $SrTiO_3$ for Increasing Photocatalytic Activity to Water Splitting. *Appl. Catal. B Environ.* **2020**, *278*, 119292.

(160) Kim, Y.; Watanabe, M.; Matsuda, J.; Staykov, A.; Kusaba, H.; Takagaki, A.; Akbay, T.; Ishihara, T. Chemo-Mechanical Strain Effects on Band Engineering of the TiO_2 Photocatalyst for Increasing the Water Splitting Activity. *J. Mater. Chem. A* **2020**, *8*, 1335–1346.

(161) Kresse, G.; Joubert, D. From Ultrasoft Pseudopotentials to the Projector Augmented-Wave Method. *Phys. Rev. B* **1999**, *59*, 1758–1775.

(162) Perdew, J.; Ruzsinszky, A.; Csonka, G. I.; Vydrov, O. A.; Scuseria, G.; Constantin, L.; Zhou, X.; Burke, K. Restoring the Density-Gradient Expansion for Exchange in Solids and Surfaces. *Phys. Rev. Lett.* **2008**, *100*, 136406.

(163) Perdew, J. P.; Burke, K.; Ernzerhof, M. Generalized Gradient Approximation Made Simple. *Phys. Rev. Lett.* **1996**, *77*, 3865–3868.

(164) Monkhorst, H. J.; Pack, J. D. Special Points for Brillouin-Zone Integrations. *Phys. Rev. B* **1976**, *13*, 5188–5192.

(165) Grimme, S.; Antony, J.; Ehrlich, S.; Krieg, H. A Consistent and Accurate Ab Initio Parametrization of Density Functional Dispersion Correction (DFT-D) for the 94 Elements H-Pu. *J. Chem. Phys.* **2010**, *132*, 154104.

(166) Henkelman, G.; Uberuaga, B. P.; Jónsson, H. A Climbing Image Nudged Elastic Band Method for Finding Saddle Points and Minimum Energy Paths. *J. Chem. Phys.* **2000**, *113*, 9901–9904.

(167) Kuisma, M.; Ojanen, J.; Enkovaara, J.; Rantala, T. T. Kohn-Sham Potential with Discontinuity for Band Gap Materials. *Phys. Rev. A* **2010**, *51*, 1944–1954.

(168) Gritsenko, O.; Van Leeuwen, R.; Van Lenthe, E.; Baerends, E. J. Self-Consistent Approximation to the Kohn-Sham Exchange Potential. *Phys. Rev. A* **1995**, *51*, 1944.

(169) Enkovaara, J.; Rostgaard, C.; Mortensen, J. J.; Chen, J.; Dułak, M.; Ferrighi, L.; Gavnholt, J.; Glinsvad, C.; Haikola, V.; Hansen, H. A.; et al. Electronic Structure Calculations with GPAW: A Real-Space Implementation of the Projector Augmented-Wave Method. *J. Phys. Condens. Matter* **2010**, *22*, 253202.

(170) FigShare—A Repository Where Users Can Make All Their Research Outputs Available in a Citable, Shareable, and Discoverable Manner. Https://Doi.Org/10.11583/DTU.13318256.

(171) Castelli, I. E.; Landis, D. D.; Thygesen, K. S.; Dahl, S.; Chorkendorff, I.; Jaramillo, T. F.; Jacobsen, K. W. New Cubic Perovskites for One- and Two-Photon Water Splitting Using the Computational Materials Repository. *Energy Environ. Sci.* **2012**, *5*, 9034.

(172) Fang, C. M.; de Wijs, G. A.; Orhan, E.; de With, G.; de Groot, R. A.; Hintzen, H. T.; Marchand, R. Local Structure and Electronic Properties of $BaTaO_2N$ with Perovskite-Type Structure. *J. Phys. Chem. Solids* **2003**, *64*, 281–286.

(173) Bouri, M.; Aschauer, U. Suitability of Different Sr_2TaO_3N Surface Orientations for Photocatalytic Water Oxidation. *Chem. Mater.* **2020**, *32*, 75–84.

(174) Wannakao, S.; Maihom, T.; Kongpatpanich, K.; Limtrakul, J.; Promarak, V. Halogen Substitutions Leading to Enhanced Oxygen Evolution and Oxygen Reduction Reactions in Metalloporphyrin Frameworks. *Phys. Chem. Chem. Phys.* **2017**, *19*, 29540–29548.

(175) Higashi, M.; Domen, K.; Abe, R. Fabrication of Efficient TaON and Ta_3N_5 Photoanodes for Water Splitting under Visible Light Irradiation. *Energy Environ. Sci.* **2011**, *4*, 4138-4147.

(176) Minegishi, T.; Nishimura, N.; Kubota, J.; Domen, K. Photoelectrochemical Properties of $LaTiO_2N$ Electrodes Prepared by Particle Transfer for Sunlight-Driven Water Splitting. *Chem. Sci.* **2013**, *4*, 1120-1124.

(177) Butler, K. T.; Frost, J. M.; Walsh, A. Ferroelectric Materials for Solar Energy Conversion: Photoferroics Revisited. *Energy Environ. Sci.* **2015**, *8*, 838–848.

(178) Castelli, I. E.; Olsen, T.; Chen, Y. Towards Photoferroic Materials by Design: Recent Progress and Perspectives. *J. Phys. Energy* **2019**, *2*, 011001.

(179) Kim, S.; Nguyen, N.; Bark, C. Ferroelectric Materials: A Novel Pathway for Efficient Solar Water Splitting. *Appl. Sci.* **2018**, *8*, 1526.

(180) Singh, S.; Sangle, A. L.; Wu, T.; Khare, N.; MacManus-Driscoll, J. L. Growth of Doped $SrTiO_3$ Ferroelectric Nanoporous Thin Films and Tuning of Photoelectrochemical Properties with Switchable Ferroelectric Polarization. *ACS Appl. Mater. Interfaces* **2019**, *11*, 45683–45691.

(181) Yin, X.; Li, X.; Liu, H.; Gu, W.; Zou, W.; Zhu, L.; Fu, Z.; Lu, Y. Realizing Selective Water Splitting Hydrogen/Oxygen Evolution on Ferroelectric Bi_3TiNbO_9 Nanosheets. *Nano Energy* **2018**, *49*, 489–497.

(182) Tiwari, D.; Dunn, S. Photochemistry on a Polarisable Semi-Conductor: What Do We Understand Today? *J. Mater. Sci.* **2009**, *44*, 5063–5079.

(183) Li, L.; Salvador, P. A.; Rohrer, G. S. Photocatalysts with Internal Electric Fields. *Nanoscale* **2014**, *6*, 24–42.

(184) Scott, J. F. Applications of Modern Ferroelectrics. *Science.* **2007**, *315*, 954–959.

(185) Lejman, M.; Vaudel, G.; Infante, I. C.; Gemeiner, P.; Gusev, V. E.; Dkhil, B.; Ruello, P. Giant Ultrafast Photo-Induced Shear Strain in Ferroelectric $BiFeO_3$. *Nat. Commun.* **2014**, *5*, 4301.

(186) Feng, Y.; Xu, M.; Liu, H.; Li, W.; Li, H.; Bian, Z. Charge Separation and Interfacial Selectivity Induced by Synergistic Effect of Ferroelectricity and Piezoelectricity on $PbTiO_3$ Monocrystalline Nanoplates. *Nano Energy* **2020**, *73*, 104768.

(187) Liu, Y.; Ye, S.; Xie, H.; Zhu, J.; Shi, Q.; Ta, N.; Chen, R.; Gao, Y.; An, H.; Nie, W.; et al. Internal-Field-Enhanced Charge Separation in a Single-Domain Ferroelectric $PbTiO_3$ Photocatalyst. *Adv. Mater.* **2020**, *32*, 1906513.

(188) Senthilkumar, P.; Jency, D. A.; Kavinkumar, T.; Dhayanithi, D.; Dhanuskodi, S.; Umadevi, M.; Manivannan, S.; Giridharan, N. V.; Thiagarajan, V.; Sriramkumar, M.; et al. Built-in Electric Field Assisted Photocatalytic Dye Degradation and Photoelectrochemical Water Splitting of Ferroelectric Ce Doped $BaTiO_3$ Nanoassemblies. *ACS Sustain. Chem. Eng.* **2019**, 7, 12032-12043.

(189) Kasahara, A.; Nukumizu, K.; Takata, T.; Kondo, J. N.; Hara, M.; Kobayashi, H.; Domen, K. $LaTiO_2N$ as a Visible-Light (≤600 nm)-Driven Photocatalyst (2). *J. Phys. Chem. B* **2003**, *107*, 791–797.

(190) Aguiar, R.; Logvinovich, D.; Weidenkaff, A.; Rachel, A.; Reller, A.; Ebbinghaus, S. G. The Vast Colour Spectrum of Ternary Metal Oxynitride Pigments. *Dye. Pigment.* **2008**, *76*, 70–75.

(191) Castelli, I. E.; Olsen, T.; Datta, S.; Landis, D. D.; Dahl, S.; Thygesen, K. S.; Jacobsen, K. W. Computational Screening of Perovskite Metal Oxides for Optimal Solar Light Capture. *Energy Environ. Sci.* **2012**, *5*, 5814–5819.

(192) Van Aken, B. B.; Palstra, T. T. M.; Filippetti, A.; Spaldin, N. A. The Origin of Ferroelectricity in Magnetoelectric $YMnO_3$. *Nat. Mater.* **2004**, *3*, 164–170.

(193) Skjærvø, S. H.; Meier, Q. N.; Feygenson, M.; Spaldin, N. A.; Billinge, S. J. L.; Bozin, E. S.; Selbach, S. M. Unconventional Continuous Structural Disorder at the Order-Disorder Phase Transition in the Hexagonal Manganites. *Phys. Rev. X* **2019**, *9*, 031001.

(194) Li, Y.; Li, J.; Yang, W.; Wang, X. Implementation of Ferroelectric Materials in Photocatalytic and Photoelectrochemical Water Splitting. *Nanoscale Horizons* **2020**, *5*, 1174–1187.

(195) Li, L.; Wang, P.; Shao, Q.; Huang, X. Recent Progress in Advanced Electrocatalyst Design for Acidic Oxygen Evolution Reaction. *Adv. Mater.* **2021**, 2004243.

(196) Rao, R. R.; Kolb, M. J.; Giordano, L.; Pedersen, A. F.; Katayama, Y.; Hwang, J.; Mehta, A.; You, H.; Lunger, J. R.; Zhou, H.; et al. Operando Identification of Site-Dependent Water Oxidation Activity on Ruthenium Dioxide Single-Crystal Surfaces. *Nat. Catal.* **2020**, *3*, 516–525.

(197) Yang, C.; Rousse, G.; Louise Svane, K.; Pearce, P. E.; Abakumov, A. M.; Deschamps, M.; Cibin, G.; Chadwick, A. V.; Dalla Corte, D. A.; Anton Hansen, H.; et al. Cation Insertion to Break the Activity/Stability Relationship for Highly Active Oxygen Evolution Reaction Catalyst. *Nat. Commun.* **2020**, *11*, 1378.

(198) Kim, J. S.; Kim, B.; Kim, H.; Kang, K. Recent Progress on Multimetal Oxide Catalysts for the Oxygen Evolution Reaction. *Adv. Energy Mater.* **2018**, *8*, 1702774.

(199) Nørskov, J. K.; Bligaard, T.; Rossmeisl, J.; Christensen, C. H. Towards the Computational Design of Solid Catalysts. *Nat. Chem.* **2009**, *1*, 37–46.

(200) Koper, M. T. M. Thermodynamic Theory of Multi-Electron Transfer Reactions: Implications for Electrocatalysis. *J. Electroanal. Chem.* **2011**, *660*, 254–260.

(201) Dues, C.; Schmidt, W. G.; Sanna, S. Water Splitting Reaction at Polar Lithium Niobate Surfaces. *ACS Omega* **2019**, *4*, 3850–3859.

(202) Kakekhani, A.; Ismail-Beigi, S. Polarization-Driven Catalysis via Ferroelectric Oxide Surfaces. *Phys. Chem. Chem. Phys.* **2016**, *18*, 19676–19695.

(203) Kresse, G.; Joubert, D. From Ultrasoft Pseudopotentials to the Projector Augmented-Wave Method. *Phys. Rev. B* **1999**, *59*, 1758–1775.

(204) Bengtsson, L. Dipole Correction for Surface Supercell Calculations. *Phys. Rev. B* **1999**, *59*, 12301–12304.

(205) Neaton, J. B.; Ederer, C.; Waghmare, U. V.; Spaldin, N. A.; Rabe, K. M. First-Principles Study of Spontaneous Polarization in Multiferroic $BiFeO_3$. *Phys. Rev. B* **2005**, *71*, 014113.

(206) Stefano Baroni; Giannozzi, P.; Testa, A. Green's-Function Approach to Linear Response in Solids Stefano. *Phys. Rev. Lett.* **1987**, *58*, 1100–1103.

(207) Heyd, J.; Scuseria, G. E.; Ernzerhof, M. Hybrid Functionals Based on a Screened Coulomb Potential. *J. Chem. Phys.* **2003**, *118*, 8207–8215.

(208) Valdés, Á.; Qu, Z. W.; Kroes, G.-J.; Rossmeisl, J.; Nørskov, J. K. Oxidation and Photo-Oxidation of Water on TiO_2 Surface. *J. Phys. Chem. C* **2008**, *112*, 9872–9879.

(209) Castelli, I. E.; Thygesen, K. S.; Jacobsen, K. W. Calculated Pourbaix Diagrams of Cubic Perovskites for Water Splitting: Stability Against Corrosion. *Top. Catal.* **2014**, *57*, 265–272.

(210) DTU Data Repository,Https://Doi.Org/10.11583/DTU.14528670.

(211) Fennie, C. J.; Rabe, K. M. Ferroelectric Transition in $YMnO_3$ from First Principles. *Phys. Rev. B* **2005**, *72*, 100103.

(212) Småbråten, D. R.; Holstad, T. S.; Evans, D. M.; Yan, Z.; Bourret, E.; Meier, D.; Selbach, S. M. Domain Wall Mobility and Roughening in Doped Ferroelectric Hexagonal Manganites. *Phys. Rev. Res.* **2020**, *2*, 033159.

(213) Artyukhin, S.; Delaney, K. T.; Spaldin, N. A.; Mostovoy, M. Landau Theory of Topological Defects in Multiferroic Hexagonal Manganites. *Nat. Mater.* **2014**, *13*, 42–49.

(214) Zhang, Y.; Sun, J.; Perdew, J. P.; Wu, X. Comparative First-Principles Studies of Prototypical Ferroelectric Materials by LDA, GGA, and SCAN Meta-GGA. *Phys. Rev. B* **2017**, *96*, 035143.

(215) Mulliken, R. S. A New Electroaffinity Scale; Together with Data on Valence States and on Valence Ionization Potentials and Electron Affinities. *J. Chem. Phys.* **1934**, *2*, 782–793.

(216) Bystrov, V. S.; Fridkin, V. M. Domain and Homogeneous Switching in Ferroelectrics. *Ferroelectrics* **2020**, *569*, 164–181.

(217) Lee, H.; Kim, T. H.; Patzner, J. J.; Lu, H.; Lee, J. W.; Zhou, H.; Chang, W.; Mahanthappa, M. K.; Tsymbal, E. Y.; Gruverman, A.; et al. Imprint Control of $BaTiO_3$ Thin Films via Chemically Induced Surface Polarization Pinning. *Nano Lett.* **2016**, *16*, 2400–2406.

(218) Shetty, M.; Walton, A.; Gathmann, S. R.; Ardagh, M. A.; Gopeesingh, J.; Resasco, J.; Birol, T.; Zhang, Q.; Tsapatsis, M.; Vlachos, D. G.; et al. The Catalytic Mechanics of Dynamic Surfaces: Stimulating Methods for Promoting Catalytic Resonance. *ACS Catal.* **2020**, *10*, 12666–12695.

(219) Ruff, A.; Li, Z.; Loidl, A.; Schaab, J.; Fiebig, M.; Cano, A.; Yan, Z.; Bourret, E.; Glaum, J.; Meier, D.; et al. Frequency Dependent Polarisation Switching in h-$ErMnO_3$. *Appl. Phys. Lett.* **2018**, *112*, 182908.

(220) Gopeesingh, J.; Ardagh, M. A.; Shetty, M.; Burke, S. T.; Dauenhauer, P. J.; Abdelrahman, O. A. Resonance-Promoted Formic Acid Oxidation via Dynamic Electrocatalytic Modulation. *ACS Catal.* **2020**, *10*, 9932–9942.

Appendix

Paper1

Theoretical Insight on Anion Ordering, Strain, and Doping Engineering of the Oxygen Evolution Reaction in $BaTaO_2N$

Zhenyun Lan, Tejs Vegge, Ivano E. Castelli *

Chem. Mater. 2021, 33, 9, 3297–3303

CHEMISTRY OF MATERIALS

pubs.acs.org/cm

Article

Theoretical Insight on Anion Ordering, Strain, and Doping Engineering of the Oxygen Evolution Reaction in $BaTaO_2N$

Zhenyun Lan, Tejs Vegge, and Ivano E. Castelli*

Cite This: *Chem. Mater.* 2021, 33, 3297−3303

Read Online

ACCESS | Metrics & More | Article Recommendations | Supporting Information

ABSTRACT: Oxynitride perovskites such as $BaTaO_2N$ are among the most promising materials to achieve efficient direct solar-to-chemical conversion. Albeit photoelectrochemical water splitting has been demonstrated, the required overpotentials remain prohibitively large compared with the theoretically accessible values, particularly for the oxygen evolution reaction (OER). Here, we apply density functional theory (DFT) calculations to investigate the use of strain and cationic doping with Ca and Sr to optimize the OER theoretical overpotential. For the TaON-terminated $BaTaO_2N$ (001) surface, 4% compressive uniaxial strain can lower the theoretical overpotential to η = 0.59 V, under operational conditions. For the most stable TaO_2N-(100) termination, 1% tensile uniaxial strain, which is perfectly accessible by experiments, is enough to reduce the theoretical overpotential from η = 0.43 V to η = 0.37 V under (photo)electrochemical conditions. This value is close to the minimum predicted theoretical overpotential and points out how strain engineering could be efficiently used to improve the electrocatalytic reactions.

INTRODUCTION

Over the last decade, oxynitrides have been investigated for multiple applications, ranging from ferroelectricity[1] to electrocatalysis[2] and photocatalysis.[3] In general, by combining oxygen and nitrogen as anions, oxynitrides show higher stability in air and moisture compared to pure nitrides, and the perovskite-structured oxynitrides display smaller band gaps than those of pure oxides,[4] which contribute to their attractive electronic and optical properties in photocatalysis or photoelectrocatalysis for water-splitting devices. Among the identified compositions,[5] $BaTaO_2N$ is one of the promising candidates as photoelectrocatalysts for water splitting because of its optical band gap (approximately 1.9 eV, which is close to the minimum energy needed to split water once the bare energy to split water and the reaction overpotentials are considered)[6] and band-edge position, which straddle the redox potentials of the hydrogen evolution reaction and OER.[7−10] Although much effort has been carried out to improve the performance of $BaTaO_2N$ for water splitting, its photocatalytic activity is still far from practical applications.[7,8,11−13] One of the strategies to improve the catalytic activity is to reduce the overpotentials required to split water into molecular oxygen and hydrogen. The lowest theoretical overpotentials for the OER on oxide and oxynitrides are predicted to be 0.2−0.4 V.[14] Therefore, the surface reactions, especially for OER, is a critical bottleneck, which currently limits the efficiency of solar-to-chemical conversion and ultimately the use of oxynitrides as materials for water splitting.

The properties of perovskite oxynitrides are sensitive to the surface local structure and oxygen/nitrogen ordering.[15−17] The ordering of the O/N anions in oxynitrides is caused by the four coordinate ionic radii of O^{2-} (1.38 Å) and N^{3-} (1.46 Å) and the corresponding chemical bonding environment (valence) between O/N and neighboring high-valence metals (M/O or M/N).[18,19] Therefore, different exposed surface terminations also show different O/N anionic orderings, which affects the physicochemical properties and catalytic activity.[20] In addition to this, doping and strain engineering have been proved to be effective methods in tailoring the surface electronic structures and catalytic properties.[21−24] Substitution (or partial substitution) of the A site and/or B site by other elements with different radii or valences,[25] as well as strain manipulations, can easily alter the geometrical and electronic structure of the active sites.[26] A typical example is efficient electrochemical N_2 reduction could be achieved by doping strain-induced bi-Ti^{3+} pairs.[27] More specifically, for perovskite oxynitrides, the changes in properties due to the applied strain have also been verified experimentally, starting from computational predictions, such as the change in the anion arrangement in $Ca_{1-x}Sr_xTaO_2N$,[26] the 2D to 3D crossover on a cubic lattice of correlated disorder of O and N atoms within the $Ba_{1-x}Sr_xTaO_2N$ series,[28] and the creation and switching of anion vacancy layers in $SrVO_{2.2}N_{0.6}$.[29] Another example is that epitaxial strain effects lead to a tetragonal distortion of the $BaTaO_2N$ perovskite unit cell, with negligible volume change, which shows a unique combination of high dielectric permittivities and insensitivity to changes in temperature.[30] Furthermore, a ferroelectric response in tensile-strained

Received: February 1, 2021
Revised: April 14, 2021
Published: April 28, 2021

$SrTaO_2N$ films is observed due to a change of the anion ordering as a function of the applied strain.[31] Regarding the electronic properties, tuning of the band gap has been achieved in Y-substituted $LaTaO_2N$ from an orthorhombic strain.[32] From the perspective of photocatalysis, controlling the morphological and structural variations of $LaTiO_2N$ and CoO_x nanoparticles could influence the strain in the structure and hence promote the photocatalytic O_2 evolution.[33] It has also been reported that Au−$SrTiO_3$ with tensile strain, where the strain is induced by the difference of the thermal expansion coefficient between Au and $SrTiO_3$, shows 10.5 times higher photocatalytic activity for water splitting than the unstrained Au−$SrTiO_3$.[34] The significant increase in the rate of H_2 and O_2 formation has also been reported for strained TiO_2, where the strain is obtained by Au dispersion.[35]

In this work, we show that doping and strain engineering, in particular, can be used to improve the catalytic OER performance of $BaTaO_2N$ for water splitting. Using DFT calculations, we have investigated the role of anion ordering, strain, and doping modifications in the OER for the (100) TaO_2N-terminated and (001) TaON-terminated surfaces of $BaTaO_2N$. The theoretical overpotential for OER on the clean TaO_2N surface (η = 1.64 V) is much higher than that of a clean TaON surface (η = 0.97 V). On the other hand, under realistic (photo-)electrochemical conditions, the full oxygen-covered TaO_2N surface shows the lowest theoretical overpotential of 0.37 V when 1% tensile uniaxial strain in the [001] direction (Figure 1b) is applied, compared to 0.59 V that can

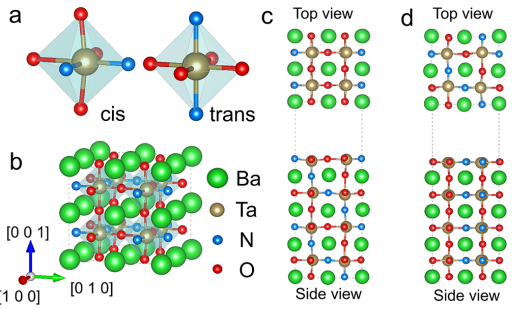

Figure 1. (a) Schematic representation of the anion ordering in a TaO_4N_2 mixed-anion octahedron. Structure of the (b) bulk $BaTaO_2N$, (c) (100) surface of $BaTaO_2N$ with TaO_2N termination on top and (d) (001) surface of $BaTaO_2N$ with TaON termination on top.

be achieved by the TaON termination with full OH coverage and 4% compressive uniaxial strain in the [010] direction. A possible strategy to achieve a lower theoretical overpotential closer to the theoretical limit is to combine strain with doping. The Ca-doped TaON-terminated $BaTaO_2N$ (001) surface, with 4% tensile uniaxial strain in the [010] direction, shows a theoretical overpotential of 0.53 V for the clean surface.

METHOD

Computational Methodology. The calculations were performed by using the projector augmented wave (PAW)[36] potentials implemented in the VASP package[37] in the framework of the generalized gradient approximation (GGA). The Perdew−Burke−Ernzerhof (PBE) revised for solids (PBEsol) exchange-correlation potential[38] was used for optimizing the bulk structures, while for surface calculations, we used the PBE exchange-correlation potential.[39] The Brillouin zone of the 40-atom bulk unit cell, which is the smallest cell allowing the representation of the correct anion ordering, is sampled with a 6 × 6 × 6 Γ-centered Monkhorst−Pack k-point mesh, and for the slab, it is sampled with a 6 × 6 × 1 Γ-centered Monkhorst−Pack k-point mesh.[40] The slab model includes eight atomic layers where the bottom four layers were fixed, and a vacuum thickness of 20 Å was added to separate the reciprocal images. For the doping modification, one Ba atom in the sublayer was replaced by Sr or Ca, and the corresponding doping concentration is 6.25%. Dipole correction was also included. Grimme's D3-type method was carried out for van der Waals interaction corrections.[41] A plane-wave energy cutoff of 550 eV was used. Cell and atomic positions were fully relaxed until the forces on the atoms were below 0.02 eV/Å. These structures were then used to build the surface models, for which only the atomic positions have been relaxed, keeping the cell frozen. The energy barrier for formation of N_2 on the (100) surface of $BaTaO_2N$ was calculated using the climbing images nudged elastic band (CI-NEB) method, and the structures were relaxed with force less than 0.05 eV/Å.[42] A more sophisticated semilocal functional (GLLB-SC)[43,44] was used to calculate the band gap of bulk $BaTaO_2N$ as implemented in the GPAW program package.[45] All data are stored and freely available at the address: DTU DATA.[46]

Surface Energy. In $BaTaO_2N$, each exposed facet has two possible terminated surfaces. To determine the most stable surface, which is more likely to form experimentally, we have calculated the surface energy (γ).[47]

$$E_{\mathrm{surf}}^{\mathrm{unr}}(X) = \frac{1}{4}[E_{\mathrm{slab}}^{\mathrm{unr}}(\text{A-termination}) + E_{\mathrm{slab}}^{\mathrm{unr}}(\text{B-termination}) - nE_{\mathrm{bulk}}] \quad (1)$$

where X is the specific termination and $E_{\mathrm{slab}}^{\mathrm{unr}}$ (A-termination) and $E_{\mathrm{slab}}^{\mathrm{unr}}$ (B-termination) are the unrelaxed A- and B-terminated slab energies. E_{bulk} is the energy of the $BaTaO_2N$ unit cell with 40 atoms.

The relaxation energy for each termination can be computed from the corresponding slab alone using[48]

$$\Delta E_{\mathrm{surf}}^{\mathrm{rel}}(X) = \frac{1}{2}[E_{\mathrm{slab}}(X) - E_{\mathrm{slab}}^{\mathrm{unr}}(X)] \quad (2)$$

where $E_{\mathrm{slab}}(X)$ is the slab energy after relaxation. The relaxed surface energy is then given by

$$E_{\mathrm{surf}}(X) = E_{\mathrm{slab}}^{\mathrm{unr}}(X) + \Delta E_{\mathrm{surf}}^{\mathrm{rel}}(X) \quad (3)$$

OER Mechanism. The OER is regarded as a key reaction as well as bottleneck in the water splitting process. Various mechanisms have been proposed for the OER, which depends on many factors from the material to the reaction environment.[49,50] In this study, we adopted a widely used mechanism for the OER that considers a process in which oxygen molecules are formed via a surface OOH intermediate, at standard conditions (T = 298 K, P = 1 bar, pH = 0), using the computational standard hydrogen electrode (SHE) approach.[50] In this model, it is assumed as a four proton-coupled electron-transfer (PCET) process

$$\text{A: } * + H_2O \rightarrow OH^* + H^+ + e^- \quad (4)$$

https://doi.org/10.1021/acs.chemmater.1c00370
Chem. Mater. 2021, 33, 3297−3303

$$\text{B: } OH^* \rightarrow O^* + H^+ + e^- \quad (5)$$

$$\text{C: } O^* + H_2O \rightarrow OOH^* + H^+ + e^- \quad (6)$$

$$\text{D: } OOH^* \rightarrow * + O_2 + H^+ + e^- \quad (7)$$

where the symbol * represents a surface reaction site, and O*, OH*, and OOH* are adsorbed oxygen, hydroxyl, and hydroperoxy groups, respectively.

While the kinetic overpotential cannot be directly determined from DFT-level calculations, we here introduce the theoretically thermodynamic overpotential (theoretical overpotential, η), which is defined as the lowest overpotential for which all the electrochemical steps are downhill in free energy. The potential of the water splitting reaction is 1.23 V per proton−electron pair transfer, and the entire process has an energy change of 4.92 eV. The step with maximum Gibbs free energy change (ΔG) of these four steps is the potential determining step. To estimate the potential determining step, Gibbs free energy change (ΔG) of each chemical reaction is calculated as

$$\Delta G(U, \text{pH}, T) = \Delta E + \Delta \text{ZPE} - T\Delta S + \Delta G_U + \Delta G_{\text{pH}} \quad (8)$$

where ΔE is the reaction energy determined from the DFT total energies and ΔZPE is the difference in zero-point energies. ΔS is the change in entropy, which was taken from the standard tables for gas-phase molecules. The values of ΔZPE and $T\Delta S$ are reported in Table S2. $\Delta G_U = -eU$ is the free energy change due to the bias potential, where U is the electrode potential relative to the SHE, and $\Delta G_{\text{pH}} = k_B T \ln[H^+] = -k_B T \ln 10 \text{ pH}$ is the correction of the free energy of H^+ ions at pH ≠ 0. Gibbs free energy change (ΔG) of each chemical reaction is affected by the same value of $k_B T \ln 10$ pH at pH ≠ 0, and the theoretical overpotential, η, is independent of pH. All values of ΔG were computed at T = 298 K and pH = 0. Due to the universal scaling relations between the adsorption energies of OOH and OH (a constant difference of 3.2 eV), the theoretical minimum overpotential for the OER, proceeding via these four PCET steps, is 0.37 V = (3.2 eV − 2 × 1.23 eV)/2e.[14]

RESULTS AND DISCUSSION

The perovskite structure of $BaTaO_2N$ exists two possible N/O orderings in the TaO_4N_2 octahedral structures: one is "cis-type" TaO_4N_2 octahedra corresponding to N−Ta−N bonds with 90° angles, and the other one is "trans-type" octahedra with 180° N−Ta−N bonds drawn in Figure 1a.[51] Here, we consider different configurations with various 2D O/N orderings (see Supporting Information, Figure S1 and Table S1), and the cis-ordered structure shown in Figure 1b is thermodynamically most stable among all the structures considered. The 40-atom bulk supercell is the smallest cell allowing representation of the correct anion ordering as well as possible octahedral distortions. The corresponding lattice parameters are $a = b$ = 8.287 Å and c = 8.095 Å. The band gap of bulk $BaTaO_2N$ is 2.49 eV, which is narrow enough to absorb visible light. To study photo-oxidation, it is essential to determine the position of valence-band edge versus SHE at pH = 0 as the driving force for OER is provided by holes at the upper edge of the valence band. We calculate that the VBM position is 2.20 eV versus SHE, which could provide an additional potential of 0.97 V with respect to the OER potential. The details of the calculation can be seen in the Supporting Information.

The two most commonly exposed (100) and (001) facets have been studied. As reported in Figure 1c,d, each facet has two terminations: for the (100) facet, TaO_2N and BaON-terminated surface and for the (001) facet, TaON and BaO_2-terminated surface. As indicated by the surface energies in Table 1, the Ta-exposed surfaces have the lowest energies, for both the (100) and (001) facets, for which we now investigate their catalytic properties. For TaO_2N-terminated (100) surfaces, there are 1/3 N atoms within anions and the two N atoms are in the symmetric sites, while for the TaON-terminated (001) surface, there are 1/2 N atoms within anions, and each two N atoms connected to the Ta atom forms N−Ta−N bonds with 90° angles.

Table 1. Calculated Surface Energies of Different Surfaces

facet	termination	surface energy (eV/Å^2)
(100)	TaO_2N	0.032
	BaON	0.056
(001)	TaON	0.081
	BaO_2	0.086

(100) Facet TaO_2N-Terminated. As shown in Figure 2a−d, the OH and OOH fragments prefer to adsorb on top of one of the Ta atom on the surface. The situation is different for O. When there is only one O, it adsorbs on the bridge site between Ta and N, while for full O coverage, half O atoms are adsorbed on the bridge site and half O atoms are located on top of the Ta atom. To predict the most relevant surface coverage under (photo)-electrocatalytic operating conditions, surface Pourbaix diagrams are computed at pH = 0, as shown in Figure 2e. The clean surface is stable only at low potential (below 0.47 V). At operating conditions, where the potential is higher than 1.23 V, the full O coverage is energetically most stable.

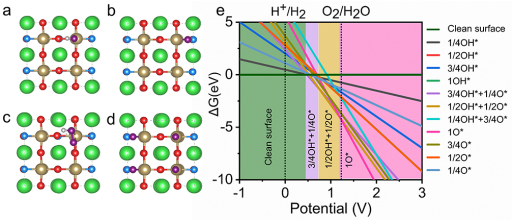

Figure 2. Structure of the (100) surface of TaO_2N-terminated $BaTaO_2N$ with (a) 1/4 OH, (b) 1/4 O, (c) 1/4 OOH, and (d) 1 O adsorbates. The purple ball and white ball represent the adsorbate O and H atoms, respectively. (e) Surface Pourbaix diagram of the TaO_2N-terminated (100) surface at pH = 0.

To investigate the role of the surface, we first study the OER on the clean surface. The surface configurations are shown in Figure 3a: the deprotonation of the H_2O molecule forms OH in step 1; then, in step 2, OH is deprotonated to form an adsorbed oxygen O, when it comes in contact with another deprotonated H_2O molecule forming OOH (step 3); and finally, in step 4, an O_2 molecule forms from the deprotonation of OOH and eventually leaves the surface. From the free energy diagrams (Figure 3a), we can see that the rate

https://doi.org/10.1021/acs.chemmater.1c00370
Chem. Mater. 2021, 33, 3297−3303

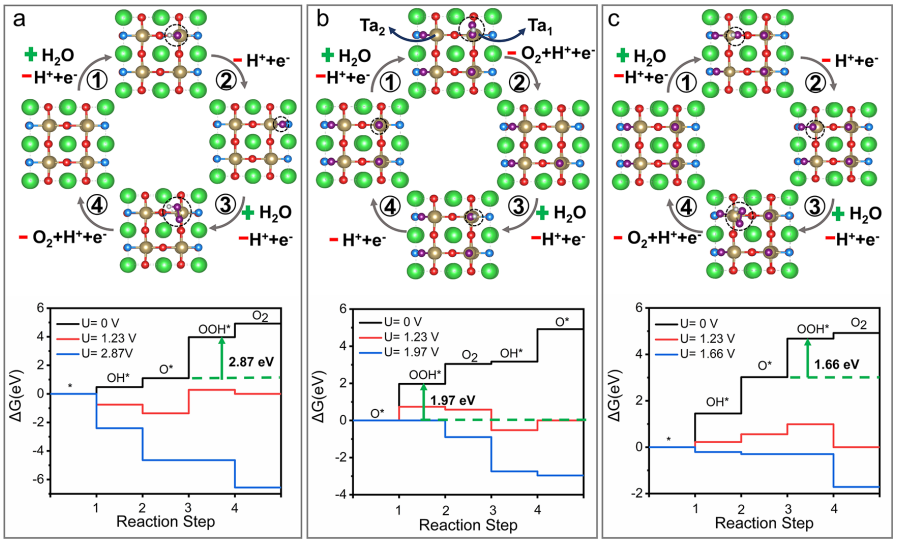

Figure 3. OER steps and Gibbs free energy diagrams for the TaO_2N-terminated (100) (a) clean surface and for the surface covered with full O (b) Ta_1 site and (c) Ta_2 site.

determining step (RDS) is the formation of OOH with a free-energy difference of 2.87 eV, which results in a theoretical overpotential of 1.64 V.

For the full O coverage, half of the O-atoms are adsorbed on the bridge sites and half O on top of Ta; therefore, there are three kinds of possible reaction sites resulting in three possible OER paths. First, the reaction could continue from an O on the bridge site. While we find that OOH cannot be formed from the bridge O, which is similar to the surface reaction on Sr_2TaO_3N.[52] Then, we consider the reaction occurring from the O atom on top of the Ta atom (Ta_1), which shows a theoretical overpotential of η = 0.74 V in Figure 3b. Surprisingly, when the reaction happens on the Ta atom without O on the top sites (Ta_2), the theoretical overpotential is only 0.43 V (Figure 3c). For all OER processes, the RDS are the formation of OOH. To understand the reasons for the much lower theoretical overpotential of the latter mechanism, we calculate the Bader charges and the charge transfer q from the Ta. These values (Table 2) indicates that the Ta with

Table 2. Bader Charge Analysis of Ta in the TaO_2N-Terminated (100) Surface Layer of $BaTaO_2N$ with Full O Coverage[a]

	average Bader charge	charge transfer q (e)
Ta_1	8.44	+2.51
Ta_2	8.49	+2.56

[a]A positive value q indicates that the electrons are removed from Ta.

adsorbed O on the bridge site is more oxidized, which weakens the Ta and O double bond, that breaks more easily on formation of the Ta−OOH intermediate (RDS) leading to a lower theoretical overpotential (0.43 V).

Strain can be used to control the structure of the surface, with its electronic and catalytic properties. Therefore, to tune and improve the OER activity, we apply compressive and tensile uniaxial strain in both [010] and [001] directions, where the negative value means the compressive strain and the positive represents the tensile strain. As indicated by the volcano plot in Figure 4a, under uniaxial strain in the [010] direction, the theoretical overpotential increases. This can be seen for both compressive and tensile strain, however, the effect is more pronounced for tensile strain. This can be explained as a combination of a change in the electronic properties of the surface, in particular, the hybridization of the O 2p and Ta d orbitals and a structural modification of the geometry of the surface and adsorbate under different strain conditions.[53] The response to the uniaxial strain in the [001] direction is, however, different. The change of the $\Delta G_{O^*} - \Delta G_{OH^*}$ in Figure 4a is linear with the strain. Under 4% compressive strain, the theoretical overpotential increases from 0.43 to 0.77 V, while under tensile strain, the theoretical overpotential first decreases, reaching the top of the volcano and afterward increases, on the other branch of the volcano. The lowest theoretical overpotential is reached at 1% tensile strain, and it is equal to 0.37 V. On the left leg of the volcano, the RDS is the formation of OOH (Figures 4a,b and S2a−c), while on the right branch, we find that the formation of O is the RDS (Figures 4d and S2d). At 1% tensile strain, which is found at the top of the volcano, the RDS is shared between the formation of OOH and O (Figure 4c). Hence, the uniaxial strain in the [001] direction can be used to modulate the RDS and tune the OER theoretical overpotential, by changing the adsorption energies of OOH and O on the surface.

It should be noted that the oxidation of the N^{3-} ions forming N_2 has been put forward for oxynitrides[54] and perovskite oxynitrides[55] by photogenerated holes during the photocatalytic reaction, which have been supported by an obvious decrease in nitrogen content indicated by XPS. Therefore, we perform NEB calculations to investigate the migration of the surface N atoms to form N_2. As shown in

https://doi.org/10.1021/acs.chemmater.1c00370
Chem. Mater. 2021, 33, 3297−3303

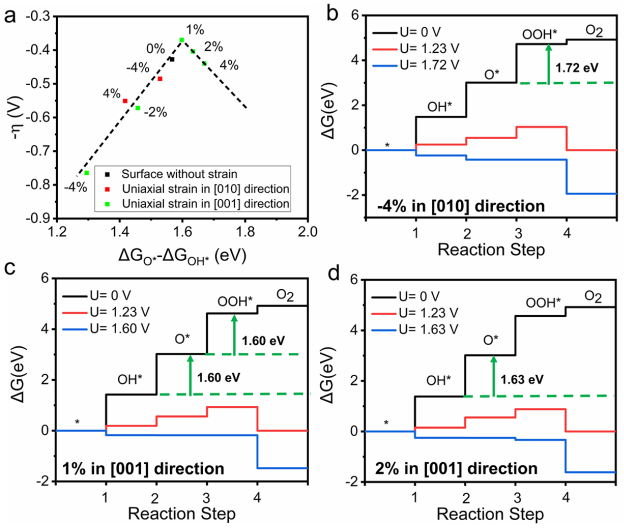

Figure 4. (a) Volcano plot of the free-energy difference of ($\Delta G_{O^*} - \Delta G_{OH^*}$) and the OER theoretical overpotential (η) for TaO_2N-terminated (100) full O-covered surfaces. Gibbs free energy diagrams for the full O-covered TaO_2N-terminated (100) surface with (b) 4% compressive uniaxial strain in the [010] direction, (c) 1% tensile uniaxial strain in the [001] direction, and (d) 2% tensile uniaxial strain in the [001] direction.

Figure S3, the energy barrier is 1.05 eV, and the process is therefore kinetically hindered compared to OER.

(001) Facet TaON-Terminated. Compared to perovskite oxides where all anions are oxygen, the N/O ordering differs from facet to facet. As shown in Figure 1c,d, the TaON-terminated (001) surface shows an obviously different N/O order compared to the TaO_2N-terminated (100) surface. On the TaON-terminated (001) surface, the two N atoms connected to the Ta atom forms N−Ta−N bonds with 90° angles. The difference of the N distribution on the surface then will influence the adsorption of the fragments. The photocatalytic properties of the different facets can thus change significantly. As shown in Figure S4a, for the clean (001) surface, the RDS is the formation of OOH resulting in a theoretical overpotential of 0.97 V, which is lower than the theoretical overpotential of the corresponding (100) surface (1.64 V). This is caused by a change in the adsorption of O. On the (001) surface, the O would like to be adsorbed on top of Ta, while on the (100) surface, the O prefers on the bridge site with a strong bond with N, which is hard to break to form OOH.

As shown in Figure 5, under 4% tensile uniaxial strain, the theoretical overpotential decreases from 0.97 to 0.69 V for the clean surface, while when 4% compressive uniaxial strain is applied, the theoretical overpotential changes from 0.78 to 0.59 V for the full OH covered surface (most stable under operating conditions shown in Figure S4b). Doping can be a valuable alternative to strain to modulate the theoretical overpotentials. Since for the clean (001) TaON surface, tensile uniaxial strain could reduce the theoretical overpotential to only 0.69 V, we attempt to further decrease the theoretical overpotential, by combining the substitution of Ba with isovalent elements with smaller radii and strain. We thus replace a sublayer Ba with Ca and Sr. It should be noted that doping alone only has a small effect on the OER activities. Sr-doping slightly reduces the

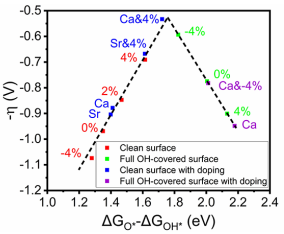

Figure 5. Volcano plot of the free-energy difference of ($\Delta G_{O^*} - \Delta G_{OH^*}$) and the OER theoretical overpotential (η) for both TaON-terminated (001) clean and full OH-covered surfaces. The uniaxial strain is in the [010] direction.

theoretical overpotential from 0.97 to 0.90 V, and Ca-doping further reduces it to 0.88 V. Moreover, combining with 4% tensile uniaxial strain, the smallest theoretical overpotential is reached for the Ca-doping on the clean surface (0.53 V), which results from $\Delta G_{O^*} - \Delta G_{OH^*}$ increasing with doping and strain. All structures with the full OH coverage surface are already on the right branch of the volcano, and 4% compressive strain is not enough to reach the top of the volcano. In general, this facet requires larger strain compared to the (100) facet, which might be hard to achieve experimentally.

■ CONCLUSIONS

In this work, we have investigated the effect that doping and strain engineering have on the OER for different terminations of the perovskite oxynitride $BaTaO_2N$. For the (100) facet TaO_2N-terminated surface, under (photo)electrochemical conditions, we have discovered that 1% tensile uniaxial strain in the [001] direction can lower the theoretical overpotential to 0.37 V from 0.43 V calculated for the structure without any applied strain. The (001) facet shows larger theoretical

https://doi.org/10.1021/acs.chemmater.1c00370
Chem. Mater. 2021, 33, 3297−3303

overpotentials compared to the (100). As an attempt to reduce them, we apply stain, reaching a theoretical overpotential of 0.59 V, under operational conditions, which, however, is still larger than what we can achieve for the (100) facet. The reason for the difference between the (100) and (001) facets is related to the different anion orderings on the surface. By applying a small strain of 1%, which can be easily reached in experiments, this work provides guidelines to experimentalists on how we can tune surface chemistry and optimize the OER catalytic properties of the material only by controlling anion ordering, strain, and doping.

■ ASSOCIATED CONTENT

Supporting Information

The Supporting Information is available free of charge at https://pubs.acs.org/doi/10.1021/acs.chemmater.1c00370.

Structure and energy of $BaTaO_2N$ with different possible anion orderings; Gibbs free energy diagrams for the full O-covered TaO_2N-terminated (100) surface under different strain; zero-point-energy corrections; and entropic contributions to free energies and band-edge analysis (PDF)

■ AUTHOR INFORMATION

Corresponding Author

Ivano E. Castelli − *Department of Energy Conversion and Storage, Technical University of Denmark, DK-2800 Kgs. Lyngby, Denmark;* orcid.org/0000-0001-5880-5045; Email: ivca@dtu.dk

Authors

Zhenyun Lan − *Department of Energy Conversion and Storage, Technical University of Denmark, DK-2800 Kgs. Lyngby, Denmark;* orcid.org/0000-0001-7943-5936

Tejs Vegge − *Department of Energy Conversion and Storage, Technical University of Denmark, DK-2800 Kgs. Lyngby, Denmark;* orcid.org/0000-0002-1484-0284

Complete contact information is available at: https://pubs.acs.org/10.1021/acs.chemmater.1c00370

Notes

The authors declare no competing financial interest.

■ ACKNOWLEDGMENTS

Z.L. acknowledges support from the China Scholarship Council (CSC). T.V. and I.E.C. wish to acknowledge the Velux Foundations for financial support through the research center V-Sustain (grant #9455) and the support from the Department of Energy Conversion and Storage, Technical University of Denmark, through the Special Competence Initiative "Autonomous Materials Discovery (http://www.aimade.org/)".

■ REFERENCES

(1) Kikkawa, S.; Sun, S.; Masubuchi, Y.; Nagamine, Y.; Shibahara, T. Ferroelectric Response Induced in Cis -Type Anion Ordered $SrTaO_2N$ Oxynitride Perovskite. *Chem. Mater.* **2016**, *28*, 1312−1317.

(2) Pan, J.; Hansen, H. A.; Vegge, T. Vanadium Oxynitrides as Stable Catalysts for Electrochemical Reduction of Nitrogen to Ammonia: The Role of Oxygen. *J. Mater. Chem. A* **2020**, *8*, 24098−24107.

(3) Fuertes, A. Metal Oxynitrides as Emerging Materials with Photocatalytic and Electronic Properties. *Mater. Horiz.* **2015**, *2*, 453−461.

(4) Ahmed, M.; Xinxin, G. A Review of Metal Oxynitrides for Photocatalysis. *Inorg. Chem. Front.* **2016**, *3*, 578−590.

(5) Maeda, K.; Domen, K. Oxynitride Materials for Solar Water Splitting. *MRS Bull.* **2011**, *36*, 25−31.

(6) Sivula, K.; van de Krol, R. Semiconducting Materials for Photoelectrochemical Energy Conversion. *Nat. Rev. Mater.* **2016**, *1*, 15010.

(7) Ueda, K.; Minegishi, T.; Clune, J.; Nakabayashi, M.; Hisatomi, T.; Nishiyama, H.; Katayama, M.; Shibata, N.; Kubota, J.; Yamada, T.; et al. Photoelectrochemical Oxidation of Water Using $BaTaO_2N$ Photoanodes Prepared by Particle Transfer Method. *J. Am. Chem. Soc.* **2015**, *137*, 2227−2230.

(8) Jadhav, S.; Hasegawa, S.; Hisatomi, T.; Wang, Z.; Seo, J.; Higashi, T.; Katayama, M.; Minegishi, T.; Takata, T.; Peralta-Hernández, J. M.; et al. Efficient Photocatalytic Oxygen Evolution Using $BaTaO_2N$ Obtained from Nitridation of Perovskite-Type Oxide. *J. Mater. Chem. A* **2020**, *8*, 1127−1130.

(9) Maeda, K.; Domen, K. Preparation of $BaZrO_3$−$BaTaO_2N$ Solid Solutions and the Photocatalytic Activities for Water Reduction and Oxidation under Visible Light. *J. Catal.* **2014**, *310*, 67−74.

(10) Hafez, A. M.; Salem, N. M.; Allam, N. K. Unravelling the Correlated Electronic and Optical Properties of $BaTaO_2N$ with Perovskite-Type Structure as a Potential Candidate for Solar Energy Conversion. *Phys. Chem. Chem. Phys.* **2014**, *16*, 18418−18424.

(11) Seo, J.; Nakabayashi, M.; Hisatomi, T.; Shibata, N.; Minegishi, T.; Domen, K. Solar-Driven Water Splitting over a $BaTaO_2N$ Photoanode Enhanced by Annealing in Argon. *ACS Appl. Energy Mater.* **2019**, *2*, 5777−5784.

(12) Higashi, M.; Domen, K.; Abe, R. Fabrication of an Efficient $BaTaO_2N$ Photoanode Harvesting a Wide Range of Visible Light for Water Splitting. *J. Am. Chem. Soc.* **2013**, *135*, 10238−10241.

(13) Maeda, K.; Lu, D.; Domen, K. Oxidation of Water under Visible-Light Irradiation over Modified $BaTaO_2N$ Photocatalysts Promoted by Tungsten Species. *Angew. Chem., Int. Ed.* **2013**, *52*, 6488−6491.

(14) Man, I. C.; Su, H. Y.; Calle-Vallejo, F.; Hansen, H. A.; Martínez, J. I.; Inoglu, N. G.; Kitchin, J.; Jaramillo, T. F.; Nørskov, J. K.; Rossmeisl, J. Universality in Oxygen Evolution Electrocatalysis on Oxide Surfaces. *ChemCatChem* **2011**, *3*, 1159−1165.

(15) Kubo, A.; Giorgi, G.; Yamashita, K. Anion Ordering in $CaTaO_2N$: Structural Impact on the Photocatalytic Activity. Insights from First-Principles. *Chem. Mater.* **2017**, *29*, 539−545.

(16) Fuertes, A. Chemistry and Applications of Oxynitride Perovskites. *J. Mater. Chem.* **2012**, *22*, 3293.

(17) Vonrüti, N.; Aschauer, U. Anion Order and Spontaneous Polarization in $LaTiO_2N$ Oxynitride Thin Films. *Phys. Rev. Lett.* **2018**, *120*, 046001.

(18) Kubo, A.; Giorgi, G.; Yamashita, K. $MgTaO_2N$ Photocatalysts: Perovskite versus Ilmenite Structure. A Theoretical Investigation. *J. Phys. Chem. C* **2017**, *121*, 27813−27821.

(19) Kim, Y.-I.; Woodward, P. M.; Baba-Kishi, K. Z.; Tai, C. W. Characterization of the Structural, Optical, and Dielectric Properties of Oxynitride Perovskites AMO_2N (A = Ba, Sr, Ca; M = Ta, Nb). *Chem. Mater.* **2004**, *16*, 1267−1276.

(20) Luo, Y.; Suzuki, S.; Wang, Z.; Yubuta, K.; Vequizo, J. J. M.; Yamakata, A.; Shiiba, H.; Hisatomi, T.; Domen, K.; Teshima, K. Construction of Spatial Charge Separation Facets on $BaTaO_2N$ Crystals by Flux Growth Approach for Visible-Light-Driven H_2 Production. *ACS Appl. Mater. Interfaces* **2019**, *11*, 22264−22271.

(21) Wang, W.; Xu, M.; Xu, X.; Zhou, W.; Shao, Z. Perovskite Oxide Based Electrodes for High-Performance Photoelectrochemical Water Splitting. *Angew. Chem., Int. Ed.* **2020**, *59*, 136−152.

(22) You, B.; Tang, M. T.; Tsai, C.; Abild-Pedersen, F.; Zheng, X.; Li, H. Enhancing Electrocatalytic Water Splitting by Strain Engineering. *Adv. Mater.* **2019**, *31*, 1807001.

(23) Yuan, J.; Wang, C.; Liu, Y.; Wu, P.; Zhou, W. Tunable Photocatalytic HER Activity of Single-Layered TiO_2 Nanosheets with Transition-Metal Doping and Biaxial Strain. *J. Phys. Chem. C* **2019**, *123*, 526−533.
(24) Lawley, C.; Nachtegaal, M.; Stahn, J.; Roddatis, V.; Döbeli, M.; Schmidt, T. J.; Pergolesi, D.; Lippert, T. Examining the Surface Evolution of $LaTiO_xN_y$ an Oxynitride Solar Water Splitting Photocatalyst. *Nat. Commun.* **2020**, *11*, 1728.
(25) Higashi, M.; Yamanaka, Y.; Tomita, O.; Abe, R. Fabrication of Cation-Doped $BaTaO_2N$ Photoanodes for Efficient Photoelectrochemical Water Splitting under Visible Light Irradiation. *APL Mater.* **2015**, *3*, 104418.
(26) Zhang, H.; Wei, S.; Xu, X. Mg Modified $BaTaO_2N$ as an Efficient Visible-Light-Active Photocatalyst for Water Oxidation. *J. Catal.* **2020**, *383*, 135−143.
(27) Cao, N.; Chen, Z.; Zang, K.; Xu, J.; Zhong, J.; Luo, J.; Xu, X.; Zheng, G. Doping Strain Induced Bi-Ti^{3+} Pairs for Efficient N_2 Activation and Electrocatalytic Fixation. *Nat. Commun.* **2019**, *10*, 2877.
(28) Johnston, H.; Black, A. P.; Kayser, P.; Oró-Solé, J.; Keen, D. A.; Fuertes, A.; Attfield, J. P. Dimensional Crossover of Correlated Anion Disorder in Oxynitride Perovskites. *Chem. Commun.* **2018**, *54*, 5245−5247.
(29) Yamamoto, T.; Chikamatsu, A.; Kitagawa, S.; Izumo, N.; Yamashita, S.; Takatsu, H.; Ochi, M.; Maruyama, T.; Namba, M.; Sun, W.; et al. Strain-Induced Creation and Switching of Anion Vacancy Layers in Perovskite Oxynitrides. *Nat. Commun.* **2020**, *11*, 5923.
(30) Kim, Y.-I.; Si, W.; Woodward, P. M.; Sutter, E.; Park, S.; Vogt, T. Epitaxial Thin-Film Deposition and Dielectric Properties of the Perovskite Oxynitride $BaTaO_2N$. *Chem. Mater.* **2007**, *19*, 618−623.
(31) Oka, D.; Hirose, Y.; Kamisaka, H.; Fukumura, T.; Sasa, K.; Ishii, S.; Matsuzaki, H.; Sato, Y.; Ikuhara, Y.; Hasegawa, T. Possible Ferroelectricity in Perovskite Oxynitride $SrTaO_2N$ Epitaxial Thin Films. *Sci. Rep.* **2015**, *4*, 4987.
(32) Bubeck, C.; Widenmeyer, M.; De Denko, A. T.; Richter, G.; Coduri, M.; Colera, E. S.; Goering, E.; Zhang, H.; Yoon, S.; Osterloh, F. E.; et al. Bandgap-Adjustment and Enhanced Surface Photovoltage in Y-Substituted $LaTa^{IV}O_2N$. *J. Mater. Chem. A* **2020**, *8*, 11837−11848.
(33) Maegli, A. E.; Pokrant, S.; Hisatomi, T.; Trottmann, M.; Domen, K.; Weidenkaff, A. Enhancement of Photocatalytic Water Oxidation by the Morphological Control of $LaTiO_2N$ and Cobalt Oxide Catalysts. *J. Phys. Chem. C* **2014**, *118*, 16344−16351.
(34) Kim, Y.; Watanabe, M.; Matsuda, J.; Song, J. T.; Takagaki, A.; Staykov, A.; Ishihara, T. Tensile Strain for Band Engineering of $SrTiO_3$ for Increasing Photocatalytic Activity to Water Splitting. *Appl. Catal., B* **2020**, *278*, 119292.
(35) Kim, Y.; Watanabe, M.; Matsuda, J.; Staykov, A.; Kusaba, H.; Takagaki, A.; Akbay, T.; Ishihara, T. Chemo-Mechanical Strain Effects on Band Engineering of the TiO_2 Photocatalyst for Increasing the Water Splitting Activity. *J. Mater. Chem. A* **2020**, *8*, 1335−1346.
(36) Kresse, G.; Joubert, D. From Ultrasoft Pseudopotentials to the Projector Augmented-Wave Method. *Phys. Rev. B: Condens. Matter Mater. Phys.* **1999**, *59*, 1758−1775.
(37) Kresse, G.; Furthmüller, J. Efficient Iterative Schemes for Ab Initio Total-Energy Calculations Using a Plane-Wave Basis Set. *Phys. Rev. B: Condens. Matter Mater. Phys.* **1996**, *54*, 11169−11186.
(38) Perdew, J. P.; Ruzsinszky, A.; Csonka, G. I.; Vydrov, O. A.; Scuseria, G. E.; Constantin, L. A.; Zhou, X.; Burke, K. Restoring the Density-Gradient Expansion for Exchange in Solids and Surfaces. *Phys. Rev. Lett.* **2008**, *100*, 136406.
(39) Perdew, J. P.; Burke, K.; Ernzerhof, M. Generalized Gradient Approximation Made Simple. *Phys. Rev. Lett.* **1996**, *77*, 3865−3868.
(40) Monkhorst, H. J.; Pack, J. D. Special Points for Brillouin-Zone Integrations. *Phys. Rev. B: Solid State* **1976**, *13*, 5188−5192.
(41) Grimme, S.; Antony, J.; Ehrlich, S.; Krieg, H. A Consistent and Accurate Ab Initio Parametrization of Density Functional Dispersion Correction (DFT-D) for the 94 Elements H-Pu. *J. Chem. Phys.* **2010**, *132*, 154104.
(42) Henkelman, G.; Uberuaga, B. P.; Jónsson, H. A Climbing Image Nudged Elastic Band Method for Finding Saddle Points and Minimum Energy Paths. *J. Chem. Phys.* **2000**, *113*, 9901−9904.
(43) Kuisma, M.; Ojanen, J.; Enkovaara, J.; Rantala, T. T. Kohn-Sham Potential with Discontinuity for Band Gap Materials. *Phys. Rev. B: Condens. Matter Mater. Phys.* **2010**, *82*, 115106.
(44) Gritsenko, O.; Van Leeuwen, R.; Van Lenthe, E.; Baerends, E. J. Self-Consistent Approximation to the Kohn-Sham Exchange Potential. *Phys. Rev. A: At., Mol., Opt. Phys.* **1995**, *51*, 1944.
(45) Enkovaara, J.; Rostgaard, C.; Mortensen, J. J.; Chen, J.; Dułak, M.; Ferrighi, L.; Gavnholt, J.; Glinsvad, C.; Haikola, V.; Hansen, H. A.; et al. Electronic Structure Calculations with GPAW: A Real-Space Implementation of the Projector Augmented-Wave Method. *J. Phys.: Condens. Matter* **2010**, *22*, 253202.
(46) FigShare—A repository where users can make all their research outputs available in a citable, shareable, and discoverable manner (2021). https://doi.org/10.11583/DTU.13318256.
(47) Heifets, E.; Eglitis, R. I.; Kotomin, E. A.; Kotomin, E. A.; Maier, J.; Borstel, G. Ab Initio Modeling of Surface Structure for $SrTiO_3$ Perovskite Crystals. *Phys. Rev. B: Condens. Matter Mater. Phys.* **2001**, *64*, 235417.
(48) Eglitis, R. I.; Vanderbilt, D. Ab Initio Calculations of $BaTiO_3$ and $PbTiO_3$ (001) and (011) Surface Structures. *Phys. Rev. B: Condens. Matter Mater. Phys.* **2007**, *76*, 155439.
(49) Pan, Y.; Xu, X.; Zhong, Y.; Ge, L.; Chen, Y.; Veder, J.-P. M.; Guan, D.; O'Hayre, R.; Li, M.; Wang, G.; et al. Direct Evidence of Boosted Oxygen Evolution over Perovskite by Enhanced Lattice Oxygen Participation. *Nat. Commun.* **2020**, *11*, 2002.
(50) Valdés, A.; Qu, Z.-W.; Kroes, G.-J.; Rossmeisl, J.; Nørskov, J. K. Oxidation and Photo-Oxidation of Water on TiO_2 Surface. *J. Phys. Chem. C* **2008**, *112*, 9872−9879.
(51) Fang, C. M.; de Wijs, G. A.; Orhan, E.; de With, G.; de Groot, R. A.; Hintzen, H. T.; Marchand, R. Local Structure and Electronic Properties of $BaTaO_2N$ with Perovskite-Type Structure. *J. Phys. Chem. Solids* **2003**, *64*, 281−286.
(52) Bouri, M.; Aschauer, U. Suitability of Different Sr_2TaO_3N Surface Orientations for Photocatalytic Water Oxidation. *Chem. Mater.* **2020**, *32*, 75−84.
(53) Wannakao, S.; Maihom, T.; Kongpatpanich, K.; Limtrakul, J.; Promarak, V. Halogen Substitutions Leading to Enhanced Oxygen Evolution and Oxygen Reduction Reactions in Metalloporphyrin Frameworks. *Phys. Chem. Chem. Phys.* **2017**, *19*, 29540−29548.
(54) Higashi, M.; Domen, K.; Abe, R. Fabrication of Efficient TaON and Ta_3N_5 Photoanodes for Water Splitting under Visible Light Irradiation. *Energy Environ. Sci.* **2011**, *4*, 4138−4147.
(55) Minegishi, T.; Nishimura, N.; Kubota, J.; Domen, K. Photoelectrochemical Properties of $LaTiO_2N$ Electrodes Prepared by Particle Transfer for Sunlight-Driven Water Splitting. *Chem. Sci.* **2013**, *4*, 1120.

Supporting Information

Theoretical Insight on Anion Ordering, Strain, and Doping Engineering of the Oxygen Evolution Reaction in $BaTaO_2N$

*Zhenyun Lan, Tejs Vegge and Ivano E. Castelli**

Department of Energy Conversion and Storage, Technical University of Denmark, Anker Engelundsvej 411, DK-2800 Kgs. Lyngby, Denmark

E-mail address: ivca@dtu.dk (IEC)

Band edges analysis

We used an empirical method based on the electronegativity of the constituent elements, $\chi_{element}$, and the band gap to estimate the valance band edge[1]. The band edges are calculated as

$$E_{VB,CB} = E_0 + (\chi_{Ba}\chi_{Ta}\chi_O^2\chi_N)^{1/5} \pm E_{gap}/2 \quad (1)$$

Where E_0 is the difference between the vacuum level and the SHE. E_{gap} is the band gap of bulk $BaTaO_2N$ (2.49 eV). The electrongenativity $\chi_{element}$ is calculated in Mulliken scale[2]. We calculate that the VBM positions is 2.20 eV vs SHE, which could provide an additional potential of 0.97 V with respect to the OER potential.

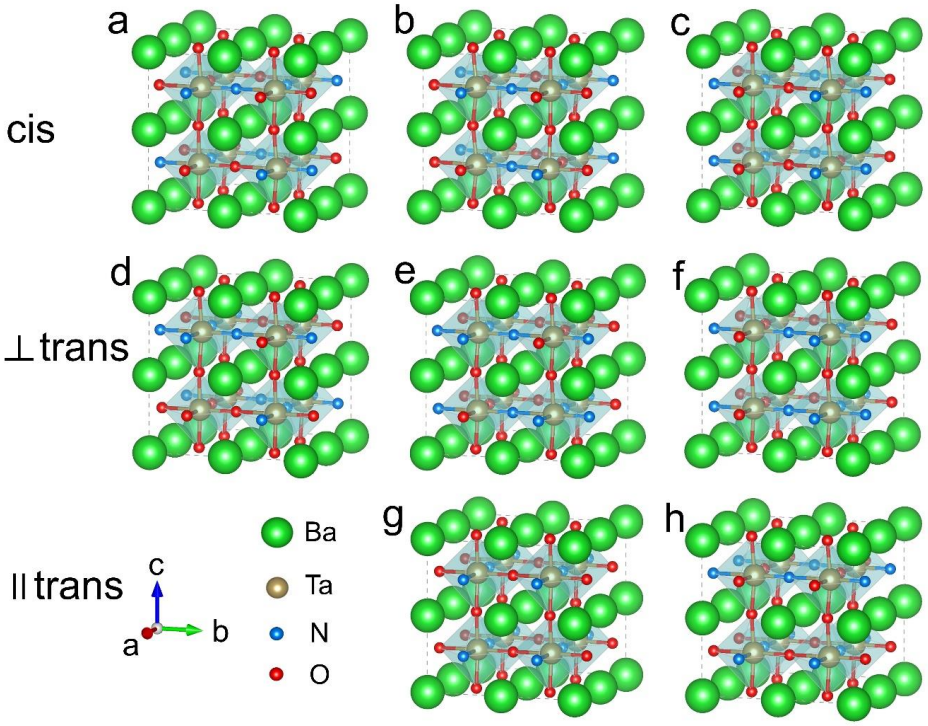

Figure S1. Structure of $BaTaO_2N$ with different anion orders. (a-c) cis - N-Ta-N chains form a 2D network with 90°angles, (d-f) ⊥trans - 180°N-Ta-N chains rectangular to each other. (g-f) ∥-trans -180°N-Ta-N chains parallel to each other. The alignment of the anion order in/along 3 different directions/planes, so there should be 24 structures. Here we only show the cis - N-Ta-N chains in a and b direction, 180°N-Ta-N chains point to a and/or b direction.

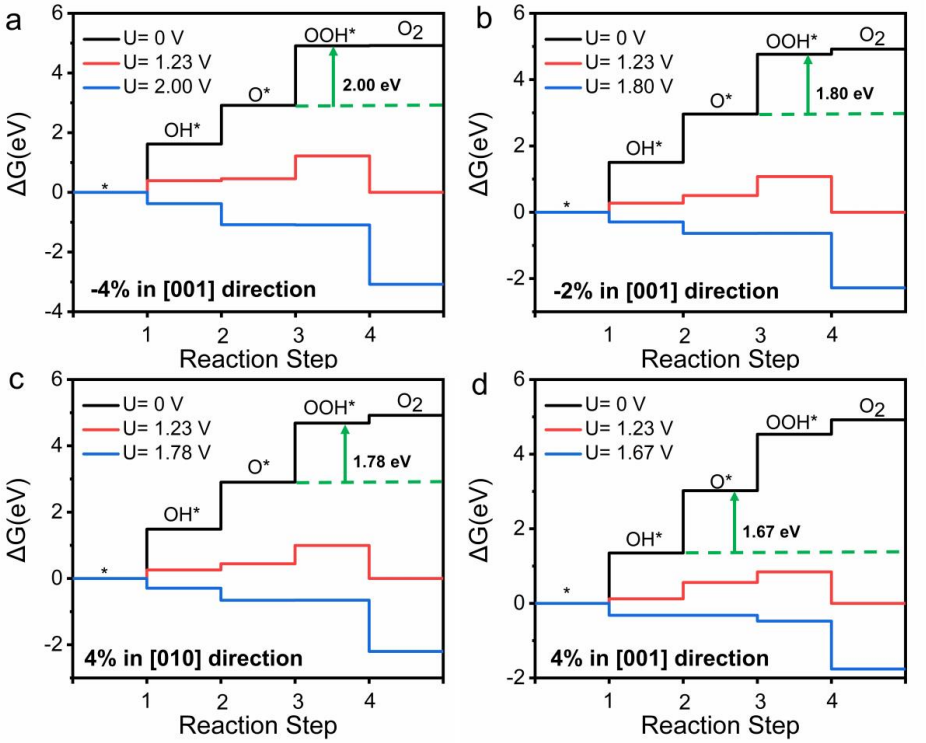

Figure S2. Gibbs free energy diagrams for the full O covered TaO_2N-terminated (100) surface with (b) 4% compressive uniaxial strain in the [001] direction, (c) 2% compressive uniaxial strain in the [001] direction, 4% tensile uniaxial strain in the [010] direction, and (d) 4% tensile uniaxial strain in the [001] direction.

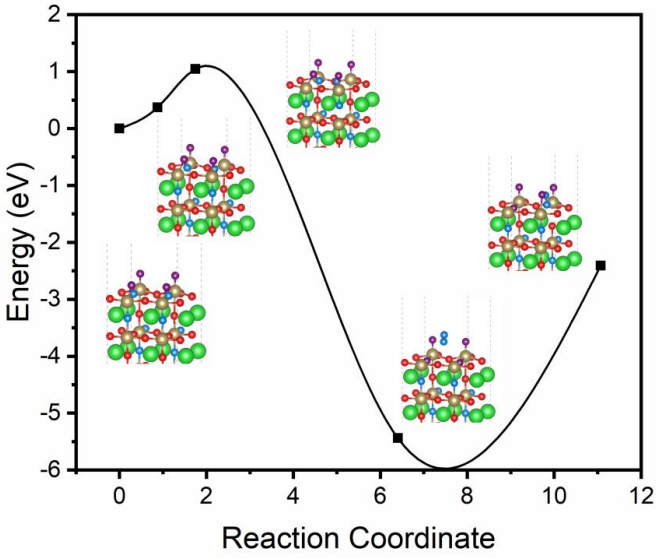

Figure S3. Energy barrier of surface nitrogen to for N_2 on the surface.

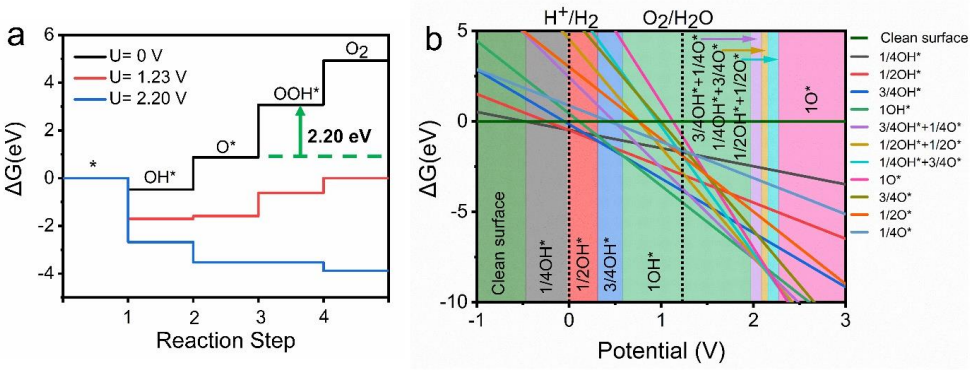

Figure S4. (a) Gibbs free energy diagrams for the TaON-terminated (001) clean surface. (b) Surface Pourbaix diagram of the TaON-terminated (001) surface at pH=0.

Table S1. The calculation energies for $BaTaO_2N$ configurations with various 2D O/N orderings.

(Corresponding to the structures in Figure S1)

Configuration	Energy (eV)	Energy compare to the most stable phase (eV)
1-cis-ab	-367.302	0.092
1-cis-ac	-367.302	0.092
1-cis-bc	-367.302	0.092
2-cis-ab	-367.315	0.079
2-cis-ac	-367.309	0.085
2-cis-bc	-367.309	0.085
3-cis-ab	-367.394	0
3-cis-ac	-367.394	0
3-cis-bc	-367.394	0
1-⊥ trans-ab	-365.162	2.232
1-⊥ trans-ac	-365.145	2.249
1-⊥ trans-bc	-365.146	2.248
2-⊥ trans-ab	-364.959	2.435
2-⊥ trans-ac	-364.959	2.435
2-⊥ trans-bc	-364.959	2.435
3-⊥ trans-ab	-364.959	2.435
3-⊥ trans-ac	-364.959	2.435
3-⊥ trans-bc	-364.959	2.435
1-∥ trans-a	-365.563	1.831
1-∥ trans-b	-365.563	1.831
1-∥ trans-c	-364.990	2.404
2-∥ trans-ab	-365.689	1.705
2-∥ trans-ac	-365.611	1.783
2-∥ trans-bc	-365.611	1.783

Table S2. Zero-Point Energy Corrections and Entropic Contributions to Free Energies.[3]

	ZPE (eV)	TS (T=298 K)
H_2	0.269	0.410
H_2O	0.593	0.670
O_2	0.100	0.640
OH*	0.350	0
O*	0.090	0
OOH*	0.470	0

References

(1) Castelli, I. E.; Landis, D. D.; Thygesen, K. S.; Dahl, S.; Chorkendorff, I.; Jaramillo, T. F.; Jacobsen, K. W. New Cubic Perovskites for One- and Two-Photon Water Splitting Using the Computational Materials Repository. *Energy Environ. Sci.* **2012**, *5*, 9034.

(2) Mulliken, R. S. A New Electroaffinity Scale; Together with Data on Valence States and on Valence Ionization Potentials and Electron Affinities. *J. Chem. Phys.* **1934**, *2*, 782–793.

(3) Valdés, Á.; Qu, Z.-W.; Kroes, G.-J.; Rossmeisl, J.; Nørskov, J. K. Oxidation and Photo-Oxidation of Water on TiO_2 Surface. *J. Phys. Chem. C* **2008**, *112*, 9872–9879.

Paper2

Enhancing Oxygen Evolution Reaction Activity by Using Switchable Polarization in Ferroelectric $InSnO_2N$

Zhenyun Lan, Didrik René Småbråten, Chengcheng Xiao, Tejs Vegge, Ulrich Aschauerb,* and Ivano E. Castelli* (Submitted)

Enhancing Oxygen Evolution Reaction Activity by Using Switchable Polarization in Ferroelectric $InSnO_2N$

Zhenyun Lan[a], Didrik René Småbråten[b], Chengcheng Xiao[c], Tejs Vegge[a], Ulrich Aschauer[b,*] and Ivano E. Castelli[a,*]

[a] Department of Energy Conversion and Storage, Technical University of Denmark, DK-2800 Kgs. Lyngby, Denmark
[b] Department of Chemistry, Biochemistry and Pharmaceutical Sciences, University of Bern, Bern CH-3012, Switzerland
[c] Departments of Materials and Physics, and the Thomas Young Centre for Theory and Simulation of Materials, Imperial College London, London SW7 2AZ, United Kingdom

* Corresponding Authors
Email: ivca@dtu.dk
Email: ulrich.aschauer@dcb.unibe.ch

Abstract

Ferroelectric modulation of the surface charge density is a promising strategy to promote the surface oxygen evolution reaction (OER) in photocatalytic water splitting. The limitations of the Sabatier principle could be overcome by tuning the interaction strength between the OER intermediates and the surface for the individual reaction steps via switching of the polarization direction. $InSnO_2N$, a newly reported improper ferroelectric semiconductor, is promising for applications as a photocatalyst due to its direct band gap of 1.61 eV and its sizable ferroelectric polarization. Therefore, in this work, we use Density Functional Theory (DFT) to investigate the OER performance on its (001) surface as a function of the bulk polarization direction. We find that the clean surface of the downward (negatively) polarized bulk structure ("polarized bulk" henceforth) has a lower theoretical overpotential of $\eta = 0.58$ V vs the standard hydrogen electrode (SHE) compared to the clean surface with an upward (positively) polarized bulk structure (0.77 V). Under (photo)-electrochemical operating conditions, a monolayer (ML) OH

covered surface is the most stable for the negatively polarized bulk and shows a theoretical overpotential of 0.89 V, whereas for the positively polarized bulk structure, a surface covered with 2/3 ML OH is the most stable, also showing an overpotential of 0.89 V. Notably, when switching the polarization direction during the reaction, the overpotential becomes as small as 0.20 V for the clean surface and 0.23 V for the surface with OH coverage, which is far below the usual minimum theoretical overpotential for oxides (η = 0.37 V). We show that the reduction in reaction free energy by ferroelectric switching can be performed in a relevant frequency range and outweighs the energetic cost for polarization switching by a factor 6 to 12. Our study demonstrates that switching of improper ferroelectricity is a highly promising route to boost the OER activity of oxynitride photocatalytic water splitting electrodes.

Introduction

Photoferroic materials that combine ferroelectric and light-harvesting properties, are promising for optoelectronic applications, like photovoltaics[1,2] or photo(electro)chemical water-splitting (PEC).[3] The spontaneous polarization of ferroelectrics can be reversed by application of an external electric field, with potential benefits for photoelectrocatalytic water splitting.[4–7] Due to the strong internal electric field induced by the spontaneous electric polarization, the photogenerated electrons and holes migrate in opposite directions, which enhances charge-carrier separation and promotes photocatalytic properties.[8,9] To date, more than 700 ferroelectric materials have been discovered,[10] the majority of those studied for photoelectrocatalytic applications are complex oxides, such as perovskite oxides, $BiFeO_3$,[11] $PbTiO_3$[12,13] and $BaTiO_3$.[14,15] However, their band gaps are in the ultraviolet (UV) range, they are therefore unable to absorb visible light. Although ferroelectricity could suppress the

recombination of photo-induced carriers, the large band gap of these oxides will inhibit practical photocatalytic applications. To solve this, the methods like substitution of one or more oxygen by nitrogen which leads to the so-called oxynitrides has been proposed.[16,17] Compared to oxygen, the lower electronegativity of nitrogen results in reduced band gaps and higher valence band edges that better match the water redox levels.[18–20] Recently, a tin oxynitride-based semiconductor, $InSnO_2N$, was suggested as a new and promising photocatalyst. It has a direct band gap of approx. 1.61 eV, resulting in excellent light absorption.[21] $InSnO_2N$ (Figure 1a) is isostructural to the multiferroic hexagonal manganites, h-$RMnO_3$ (R=Y, In, Sc, Ho-Lu). These materials are improper ferroelectrics, in which the corner-sharing Mn-O trigonal bipyramids are separated by layers of R ions and the tilting of the corner-sharing Mn-O trigonal bipyramids leads to the "up-down-down" R-cation displacement along c axis (or [001]) that causes polarization as a secondary effect and promotes separation of photoexcited carriers.[22,23] In addition to light absorption and carrier separation, the performance of $InSnO_2N$ in a photoelectrochemical device, will depend on its surface redox reaction properties,[24] which are currently unknown. The major obstacle among the water-splitting redox reactions, is the low efficiency of the oxygen evolution reaction (OER).[25–27] The OER is a multistep reaction involving several intermediates and every step is vital for the overall conversion efficiency.[28,29] The interaction between catalyst surface and intermediate, strong or weak, will directly affect the reaction activity. According to the Sabatier principle, if the interaction is too weak, the adsorbate (i.e. the reagent) will be unable to bind to the catalyst, while if the interaction is too strong, the reaction product will fail to desorb.[30,31] Consequently, an optimal binding strength corresponds to the maximum OER efficiency and a minimum theoretical overpotential. DFT

calculations have demonstrated that the four-step OER mechanism is fundamentally limited to a minimum theoretical overpotential of 0.3-0.4 V, due to the scaling relation between the binding strength of the OH and OOH intermediates.[32,33] The adsorption strength between the catalyst and intermediate largely depends on the surface electronic states. In a ferroelectric material, the surface states and their occupation could be altered by switching the polarization direction.[34–37] For a given surface, switching of the polarization direction can be used to optimize the adsorption strength for intermediates along the OER pathways, overcoming the limit imposed by the Sabatier principle.

In this work, we have used DFT calculations to investigate the OER performance of $InSnO_2N$ surfaces with negatively/positively polarized bulk. We find that the clean surface with a downward (negatively) polarized bulk has a lower theoretical overpotential of 0.58 V vs SHE than the clean surface with an upward (positively) polarized bulk (0.77 V). Under (photo)-electrochemical operating conditions, for the negatively polarized bulk, a 1 monolayer (ML) OH covered surface is the most stable while for the positively polarized bulk, a 2/3 ML OH coverage is preferred. The overpotentials for the OER on the OH covered surfaces with negatively and positively polarized bulk are both 0.89 V. When the polarization direction is switched during the OER, a much lower theoretical overpotential of 0.20 V is achieved for the clean surface and 0.23 V for the surface with OH coverage. These values are far below the minimum theoretical overpotential for oxides (0.37 V),[33] demonstrating that improper ferroelectric switching of suitable-band gap photoelectrodes is an exciting route to boost the OER activity, the enhancement in reaction free energies outweighing the energetic cost for polarization switching by a factor 6-12.

Method

Computational Methodology

DFT calculations were performed with the Vienna Ab initio Simulation Package (VASP).[38–40] Exchange and correlation effects were described using the Perdew−Burke−Ernzerhof (PBE) functional, in the framework of the generalized gradient approximation (GGA).[41] We used projector augmented wave (PAW)[42] potentials to represent the frozen core electrons and nuclei of each atom, and In (5s, 5d, 5p), Sn (5s, 4d, 5p), O (2s, 2p), and N(3s, 3p) were described as valence electrons, with a plane wave cutoff energy of 520 eV. We used a 6 × 6 × 3 Γ-centered Monkhorst Pack k-point mesh[43] for the bulk unit cell (30 atoms) and a 6 × 6 × 1 mesh for slab models (66 atoms). For the calculations of the partial density of states (PDOS), we used a Γ-centered k-point mesh with 12 × 12 × 6 for the bulk unit cell and 12 × 12 × 1 for the slab. The slab model is composed of 9 atomic layers where the bottom 4 layers are kept fixed during relaxation, a 20 Å vacuum was added to avoid artificial interaction between periodic images and a dipole correction was included.[44] Grimme's D3-correction was used to account for van der Waals interactions.[45] The spontaneous polarization was calculated according to the Born effective charge method,[46] where the Born effective charges are derived within Density Functional Perturbation Theory (DFPT).[47] All atoms were fully relaxed during the structural optimization until the force on each atom was less than 0.02 eV/Å. The band gap was determined using the HSE06[48] hybrid functional with a plane wave cutoff of 350 eV and a 6 × 6 × 3 Γ-centered k-point mesh. We studied the OER at standard conditions (T = 298.15 K, P = 1 bar, pH = 0), within the computational standard hydrogen electrode (SHE) framework, by

considering a widely used mechanism that consists of four proton-coupled electron-transfer (PCET) steps (see *OER mechanism*, Supporting Information).[33,49] The Pourbaix diagram gives information regarding the stability against dissolved phases, ions and chemical reactions with water.[50] The detailed calculation method is explained in ref 50. All data are stored and freely available in the DTU Data Repository.[51]

Results and discussion

The $InSnO_2N$ structure studied in this work is hexagonal and belongs to the polar space group $P6_3cm$, as shown in Figure 1a. The optimized lattice constants are a=b=6.16 Å, c=12.24 Å. The distortion of the Sn-O-N trigonal bipyramids leads to an "up-down-down" corrugation of the In cations along c axis (or [001]) with a polarization of 12.04 μC/cm^2, analogous to the improper ferroelectricity in the hexagonal manganites.[22,52] During ferroelectric switching, the structure goes through a centrosymmetric phase ($P\bar{3}c1$) shown in Figure S1. Therefore, the energy difference between the non-polar $P\bar{3}c1$ and the polar $P6_3cm$ structures (Figure 1c) is calculated to evaluate the energy barrier for polarization switching. We find an energy difference of 5.50 meV/atom, which is close to the switching energy barrier calculated for $YMnO_3$ (5 meV/atom),[53,54] but much smaller than that for $BaTiO_3$ (28 meV/atom),[55] indicating that the polarization in $InSnO_2N$ can be switched using electric fields. The stability of $InSnO_2N$ in the solution has also been analyzed in the Pourbaix diagram in Figure 1b. The yellow zone represents that $InSnO_2N$ is stable under a broad range of potential and pHs, corresponding to the working OER conditions. $InSnO_2N$ can be stable even at the highly acidic/alkaline condition. To evaluate the light absorption properties, we calculate the band structure of bulk $InSnO_2N$ using HSE06: the polar phase $InSnO_2N$ is a direct semiconductor with band gap of

1.61 eV where both the valence band maximum (VBM) and the conduction band minimum (CBM) are located at the Γ point (Figure 1c). The suitable band gap and direct transition are desirable to absorb a large fraction of solar light. As for the non-polar phase, the band gap is 1.45 eV (Figure S2) which is slightly smaller than the polar one.

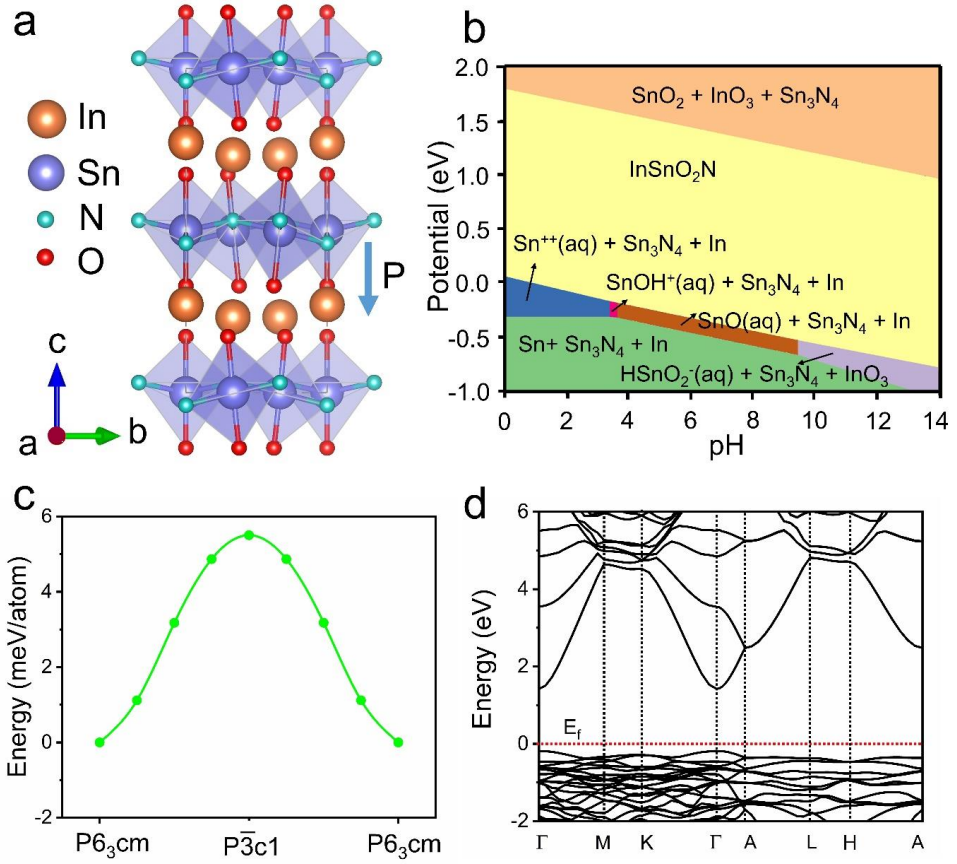

Figure 1. (a) Structure of bulk $InSnO_2N$ with $P6_3cm$ space group. The arrow represents the polarization direction. (b) Theoretical Pourbaix diagram for $InSnO_2N$. The diagrams are drawn for a concentration of 10^{-6} M at 25 °C. (c) Energy barrier of $InSnO_2N$ during through the centrosymmetric $P\bar{3}c1$ phase. (d) HSE06 band structure of bulk $InSnO_2N$ with $P6_3cm$ (polar)

space group.

Changes in polarization direction perpendicular to the surface could be used to modulate the surface properties.[37] As the polarization in $InSnO_2N$ lies along the [001] direction, we study the OER on the (001) surface. The (001) facet has two terminations, SnN and InO_2. To determine which termination is more stable, we calculate surface energies[56,57] of 1.45 J/m^2 and 1.68 J/m^2, for the SnN and InO_2 terminations respectively and consequently investigate the OER on the more stable SnN termination. After surface relaxation, the In corrugations remain "up-down-down" for the slab with negatively polarized bulk (Figure 2a) and "down-up-up" for the slab with positively polarized bulk (Figure 2d). It should be noted that the polarization in each layer is highly dependent on the paraelectric reference state used to calculate the polarization. When the unrelaxed centrosymmetric phase is used as reference, all relaxed layers have a negative polarization for the nominally negatively polarized slab (Figure S3b). On the other hand, for the positively polarized slab, due to the surface relaxation, there is an effective reversal of the polarization in the first three layers, as shown in Figure S3e, despite the fact that the In corrugation does not change. When the relaxed centrosymmetric phase is used as reference, only the first subsurface layer in the negatively polarized slab has a small positive polarization (Figure S3c) and only the surface layer in the positively polarized slab has a small negative polarization (Figure S3f). Since the In corrugation is retained, we believe that relaxations of the interlayer spacing and interlayer rumpling are responsible for the subtle local changes in the sign of the polarization. We investigate the electronic structure for the two slabs with oppositely polarized bulk. From the layer-resolved partial density of states (Figure 2),

there is a positive shift of the Fermi level for the surface with positively polarized bulk compared to the surface with negative polarization direction, which implies electrons transfer to the surface. This is also confirmed by the Bader analysis (see Table S2), which shows that the charge on positively polarized surface is 0.16 electrons higher than the charge on the negatively polarized surface.

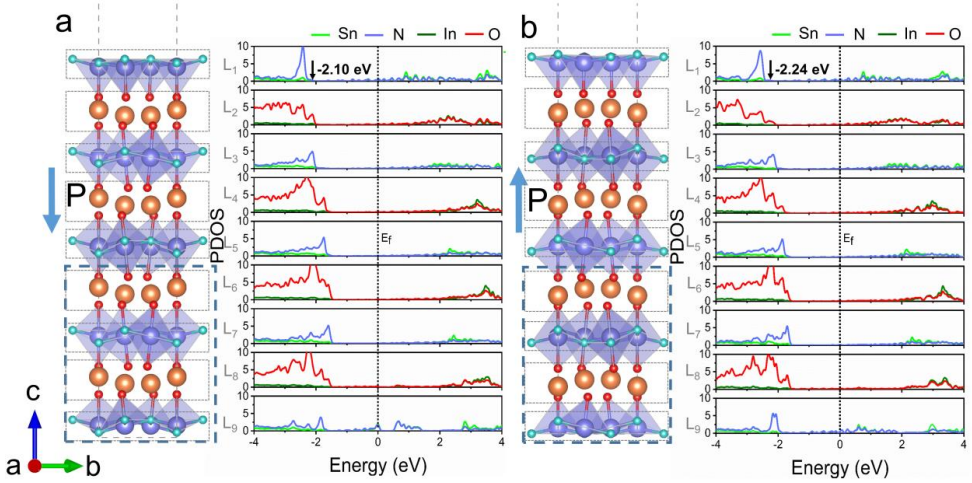

Figure 2. Structures and layer-resolved partial density of states (PDOS) of the $InSnO_2N$ (001) surface with (a) negatively polarized bulk and (b) positively polarized bulk. The arrow represents the polarization direction. L_n (1, 2, 3…9) corresponds to the atomic layer of the left structure. The bottom four-layer atoms marked by the dashed rectangle are fixed during the optimization.

To study the effect of the polarization on the OER activity, we first calculate free energy differences for the reaction steps on the clean (without adsorbates) (001) surface with oppositely polarized bulk. From the free energy profile of the OER in Figure 3, we find that for the surface with a negatively polarized bulk, the potential determining step is the formation

of O, resulting in a theoretical overpotential of 0.58 V. For the surface with a positive bulk polarization, the binding energies of the adsorbates are more negative as shown in Table 1, since the adsorption strength between the adsorbates and surface is related to the surface electronic properties and there is the higher electron density on the surface with positively polarized bulk. The potential determining step also changes to the formation of OOH and results in a theoretical overpotential of 0.77 V.

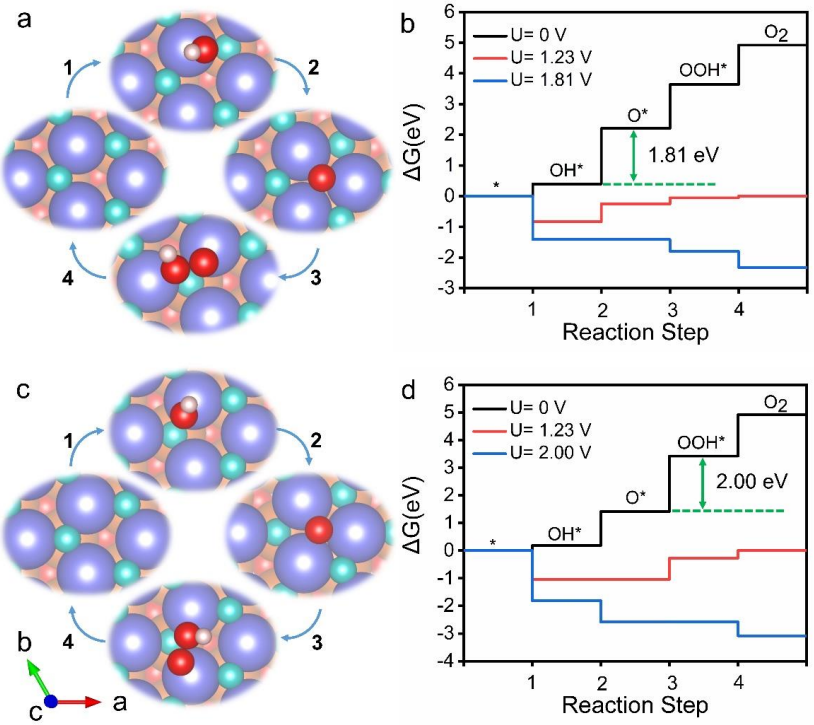

Figure 3. (a) OER steps and (b) Gibbs free energy diagram for the clean $InSnO_2N$ (001) surface with negatively polarized bulk. (c) OER steps and (d) Gibbs free energy diagram for the clean $InSnO_2N$ (001) surface with positively polarized bulk. Color code: In=orange, Sn= violet, O= red, N= cyan, H=pale pink.

Table 1. Calculated Gibbs adsorption free energies of the three OER intermediates on the (001) surface with negatively/positively polarized bulk.

	ΔG_{OH*} (eV)	ΔG_{O*} (eV)	ΔG_{OOH*} (eV)
Surface with negatively polarized bulk	0.40	2.21	3.64
Surface with positively polarized bulk	0.19	1.42	3.42

The surface structure changes under OER operating conditions, and we evaluate the stable adsorbate coverage via surface Pourbaix diagrams for surfaces with negative and positive bulk polarization at pH=0. In Figure 4a, we see that, for the surface with negatively polarized bulk, at a potential close to zero, the clean surface is the most stable. When the potential is in the range between 0.39 and 1.07 V, the surface prefers to be covered with 1/3 ML OH. In the range of 1.07 to 1.53 V, a 1 ML OH coverage is thermodynamically favored. For higher potentials, the surface prefers to be covered with 1 ML O. For the positively polarized surface (Figure 4b), when the potential is lower than 0.14 V, the clean surface is the most stable. The 1/3 ML OH covered surface becomes the most stable for the potential between 0.14 and 0.72 V. While the most stable surface changes to the 2/3 ML OH covered surface for the potential in the range of 0.72-1.71 V. When the potential is higher than 1.71 V, the surface prefers to be covered with 2/3 ML O.

As the working potential of the photocatalyst is determined by the energy difference between the VBM and the SHE, we evaluate the position of valence band edge of bulk $InSnO_2N$ with respect to the SHE as 1.89 eV via an empirical method.[58–60] The band edges of the various surfaces have further been evaluated by aligning the DOS of bulk $InSnO_2N$ and its surfaces at In 1s states. For the surface with negatively polarized bulk, the estimated surface VBM is 1.26 eV vs SHE and the surface is covered with 1 ML OH at this potential. For the surface with

positively polarized bulk, the estimated surface VBM is 1.39 eV vs SHE and, as shown in Figure 4b, the surface is covered with 2/3 ML OH at this potential. From our calculation results, we find that when an electric field of 0.05 V/Å is applied, the VBM position of the estimated surface vs the water redox levels doesn't change.

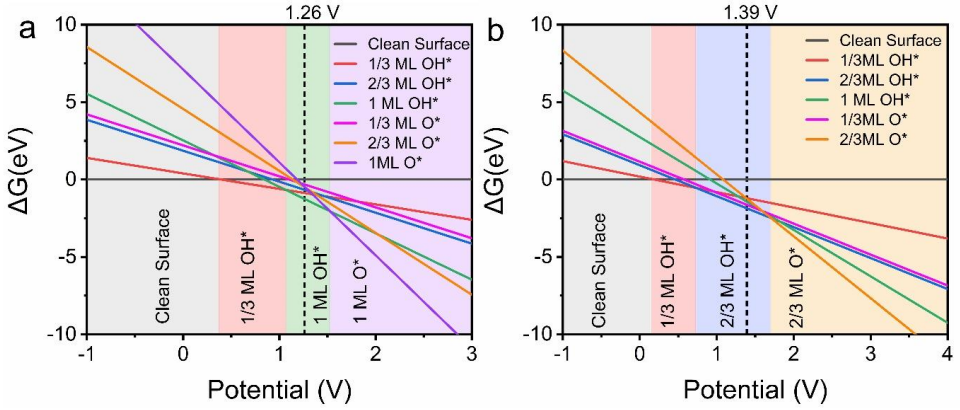

Figure 4. Surface Pourbaix diagrams of the SnN terminated (001) surface at pH=0 with (a) negatively polarized bulk and (b) positively polarized bulk. The dashed lines represent the redox potential of the photogenerated holes.

When OER happens on the 1 ML OH covered surface with negatively polarized bulk, as shown in Figure 5a, there are two possible OH positions, one on top of a Sn atom and the other on top of an N atom. We find that the OER is more facile when started from the OH on top of the Sn atoms. The free energy diagram (Figure 5b) reveals that the potential determining step is the formation of OOH with a free energy change of 2.12 eV, corresponding to a fairly large theoretical overpotential of 0.89 V.

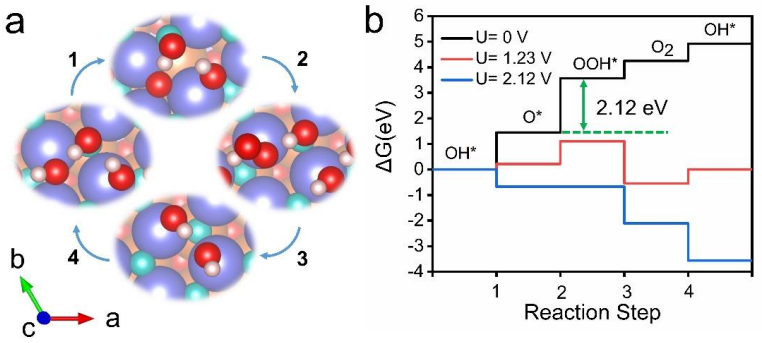

Figure 5. (a) OER steps and (b) Gibbs free energy diagram for the 1 ML OH* covered $InSnO_2N$ (001) surface with negatively polarized bulk.

Unlike on the negatively polarized one, the OER on the 2/3 ML OH* covered surface with positively polarized bulk has two possible paths. As shown in Figure 6a-b, the OER starting from an OH, proceeding in a similar fashion to the negatively polarized bulk, requires a theoretical overpotential of 0.89 V. On the other hand, as shown in Figure 6c-d, the OER can also start via the deprotonation of one H_2O molecule on the top site of the Sn atom. Interestingly the OOH fragment is unstable on top of the Sn and will spontaneously dissociate into two O fragment adsorbed on top of the Sn, while H binds to OH on a neighboring site to form H_2O bound to a Sn atom. In this mechanism, the potential determining step is the formation of two O fragment which corresponds to a change in free energy of 2.27 eV, corresponding to a much higher theoretical overpotential of 1.04 V.

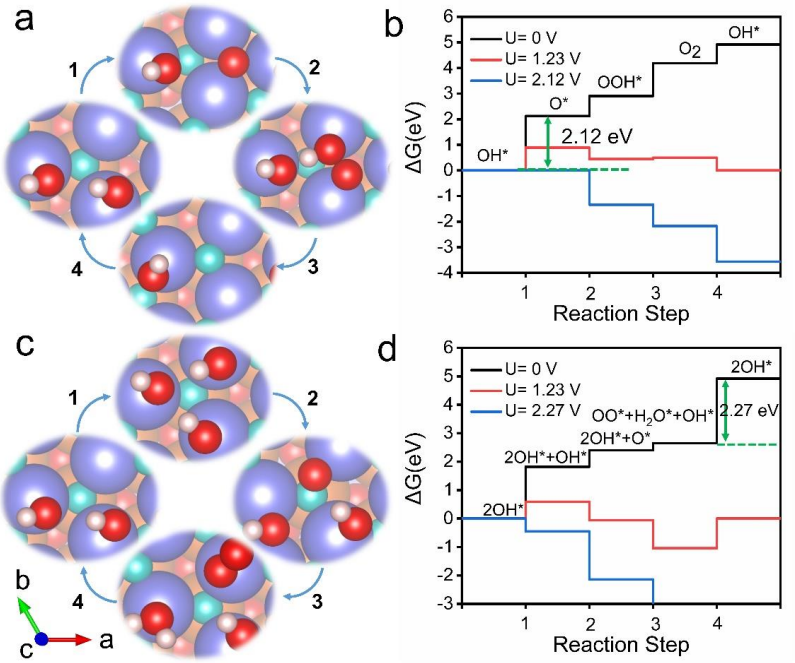

Figure 6. (a) OER steps and (b) Gibbs free energy diagram for the 2/3 ML OH* covered $InSnO_2N$ (001) surface with positively polarized bulk considering OH* as starting site. (c) OER steps and (d) Gibbs free energy diagram for the 2/3 ML OH* covered $InSnO_2N$ (001) surface with positively polarized bulk considering the top of Sn top site as starting site.

Based on the above, neither of the two polarization directions alone are particularly promising for OER. However, the different potentials determining steps for surfaces with opposite bulk polarization suggest that switching of the polarization direction could be used to enhance the OER activity. Such an enhanced pathway on the clean surface is shown in Figure 7a, where first, one H_2O molecule is deprotonated, leading to an OH fragment adsorbed on the surface with negatively polarized bulk. Then the polarization is switched and the OH fragment is adsorbed on the surface with positive polarization before being deprotonated to O. Afterwards

the polarization direction is switched again to negative and a deprotonated H_2O molecule associates with the O to form an OOH on the surface. The OOH is then deprotonated and forms an O_2 molecule that leaves from the surface in step 4. The potential determining step of this process is the formation of OOH with a free energy change of 1.43 eV, corresponding to a theoretical overpotential of only 0.20 V. The theoretical overpotential is largely decreased, compared to that of the clean surface with negatively (0.58 V) or positively (0.77 V) polarized bulk.

Under operating condition, the change of the bulk polarization direction could also be useful to enhance the OER activity. As shown in Figure 7b, in step 1, for the 1ML OH covered surface with negatively polarized bulk, the OER happens on one of the OH, which is deprotonated to O. The polarization direction can then be changed to positive. In this state a sub-ML coverage of OH is preferred and we assume that one OH desorbs from the surface and then forms OOH with the O adsorbate. This OOH is then deprotonated and desorbs as O_2 before the OH coverage is restored after a further polarization switch. This OER process is limited by the formation of OOH and the potential needed for all steps to be downhill is 1.46 V, which corresponds to a theoretical overpotential of only 0.23 V.

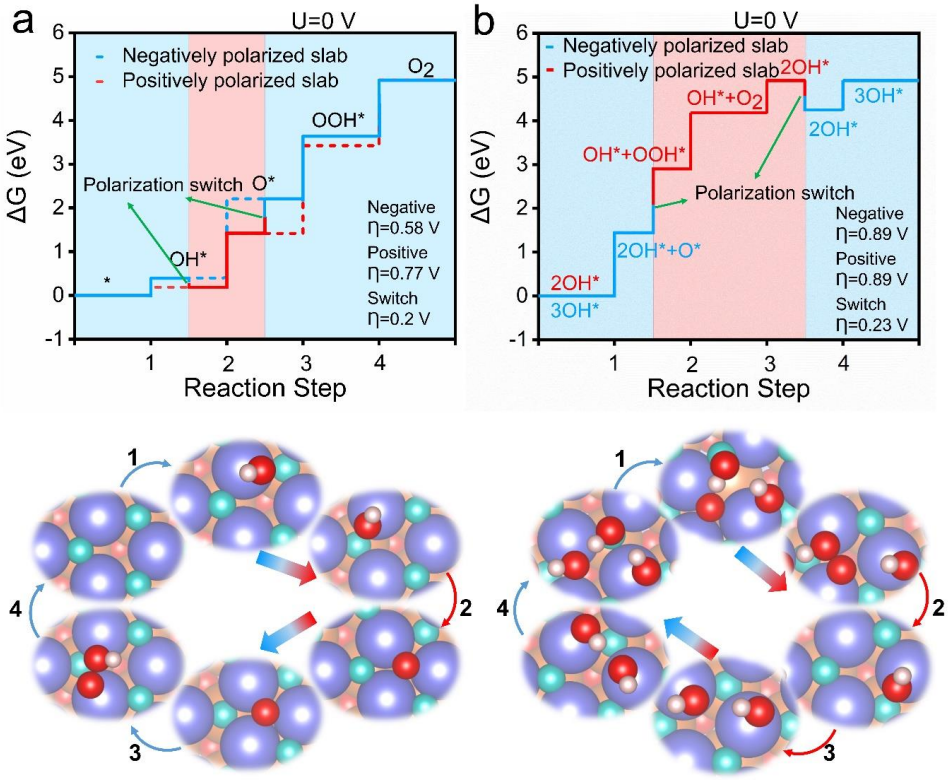

Figure 7. Gibbs free energy diagrams and OER steps including polarization switching for (a) the clean $InSnO_2N$ (001) surface and (b) the OH* covered $InSnO_2N$ (001) surface. The arrows indicate switching of the polarization direction.

The above enhancement of the OER activity relies on switching the polarization direction twice throughout the catalytic cycle, which is associated with an energetic cost. Based on the data in Figure 1b, switching amounts to an energetic cost of 5.5 meV/atom or 27.5 meV per formula unit having one Sn reactive site. During one OER cycle we thus need to provide 55 meV for the switching. We note that this analysis considers homogeneous switching of the ferroelectric, whereas a domain-mediated mechanism usually leads to a smaller energetic cost in non-2D or

ultrathin ferroelectrics.[61] We also neglect the fact that surface adsorbates will slightly affect the switching barrier but expect this effect to cancel to a large extent for the two polarization switches, since one barrier will increase, while the one of the reverse switch is decreased.[62] Despite these approximations, we expect the above estimation to yield a good upper-bound estimate of the involved energetic costs. One performance metric for a dynamic switched catalyst is the thermodynamic efficiency,[63] defined in our case as the ratio of the free-energy change of the largest OER step and the energetic cost of the ferroelectric switching, i.e. (0.58 eV - 0.20 eV) / 0.055 eV = 6.9 for the clean surface and (0.89 eV – 0.23 eV) / 0.055 eV = 12 for the adsorbate covered surface, respectively. These ratios show that the reduction of the OER free energy profile by far outweighs the cost for polarization switching. Enhanced turnover frequencies compared to the steady state represent another possible switching-frequency dependent performance metric for dynamic catalysts,[63] which unfortunately are not readily available in our thermochemical DFT framework. Nevertheless, we note that ferroelectric hexagonal manganite oxides such as $ErMnO_3$, were shown to be switchable in a frequency range from 0.1 to 1000 Hz,[64] which covers the optimally resonant range for typical catalytic reactions such as formic acid oxidation[65] and should allow the practical implementation of switched $InSnO_2N$ ferroelectric photocatalysts. Moreover, it is also suitable for the large-scale catalyst with numerous active sites, even though the reaction steps of each active site are not usually synchronized. However, when the overpotential is larger than the needed value, the reaction will stop, and the fragments will “pile up”. The reaction will restart when the polarization direction is flipped, which would enable a self-synchronization of the active sites.

Conclusion

In this work, we have theoretically investigated the effect of surface ferroelectric switching on the OER performance of the improper ferroelectric $InSnO_2N$ by means of DFT calculations. For the clean surface, the surface with negatively polarized bulk has a lower theoretical overpotential of 0.58 V, compared with the surface with positively polarized bulk (0.77 V), which is related to the increased surface electrons density. Under (photo)-electrochemical operating condition, the surface with negatively polarized bulk prefers to be covered with 1 ML OH, while for the positively polarized bulk, the surface covered with 2/3 ML OH is most stable. The theoretical overpotential for the OER on the surface with negative polarized bulk is 0.89 V which is same as the one with positively polarized bulk. When the polarization direction is switched during the OER, a lower theoretical overpotential as low as $\eta = 0.20$ V is observed for the clean surface and 0.23 V for the surface with OH coverage, which is far below the minimum theoretical overpotential for oxides (0.37 V). Moreover the reduction in reaction free energy is larger by a factor 6 to 12 compared to the estimated energetic cost for polarization switching. This suggests that switching the improper ferroelectric polarization direction is a valuable path towards optimizing ferroelectric OER catalysts.

Supporting information

Method details for OER mechanism; structures for bulk $InSnO_2N$; structures and layer-by-layer out of plane spontaneous polarization of the $InSnO_2N$ (001) surface; zero-point-energy corrections; net charge of the atoms on the surface and entropic contributions to free energies.

Acknowledgments

Z.L. and C.X. acknowledge support from the China Scholarship Council (CSC). T.V. wishes to acknowledge the Velux Foundations for financial support through the research center V-Sustain (grant #9455). T.V and I.E.C. acknowledge the support from the Department of Energy Conversion and Storage, Technical University of Denmark, through the Special Competence Initiative "Autonomous Materials Discovery (http://www.aimade.org/)". D.R.S. and U.A. were supported by the Swiss National Science Foundation under projects 200021_178791 and PP00P2_187185 respectively.

Notes

The authors declare no competing financial interest.

References

(1) Butler, K. T.; Frost, J. M.; Walsh, A. Ferroelectric Materials for Solar Energy Conversion: Photoferroics Revisited. *Energy Environ. Sci.* **2015**, *8*, 838–848.

(2) Castelli, I. E.; Olsen, T.; Chen, Y. Towards Photoferroic Materials by Design: Recent Progress and Perspectives. *J. Phys. Energy* **2019**, *2*, 011001.

(3) Kim, S.; Nguyen, N.; Bark, C. Ferroelectric Materials: A Novel Pathway for Efficient Solar Water Splitting. *Appl. Sci.* **2018**, *8*, 1526.

(4) Lee, J. H.; Selloni, A. TiO_2 Ferroelectric Heterostructures as Dynamic Polarization-Promoted Catalysts for Photochemical and Electrochemical Oxidation of Water. *Phys. Rev. Lett.* **2014**.

(5) Singh, S.; Sangle, A. L.; Wu, T.; Khare, N.; MacManus-Driscoll, J. L. Growth of Doped $SrTiO_3$ Ferroelectric Nanoporous Thin Films and Tuning of Photoelectrochemical Properties with Switchable Ferroelectric Polarization. *ACS Appl. Mater. Interfaces* **2019**, *11*, 45683–45691.

(6) Yin, X.; Li, X.; Liu, H.; Gu, W.; Zou, W.; Zhu, L.; Fu, Z.; Lu, Y. Realizing Selective Water Splitting Hydrogen/Oxygen Evolution on Ferroelectric Bi_3TiNbO_9 Nanosheets. *Nano Energy* **2018**, *49*, 489–497.

(7) Ju, L.; Shang, J.; Tang, X.; Kou, L. Tunable Photocatalytic Water Splitting by the Ferroelectric Switch in a 2D $AgBiP_2Se_6$ Monolayer. *J. Am. Chem. Soc.* **2020**, *142*, 1492–1500.

(8) Tiwari, D.; Dunn, S. Photochemistry on a Polarisable Semi-Conductor: What Do We Understand Today? *J. Mater. Sci.* **2009**, *44*, 5063–5079.

(9) Li, L.; Salvador, P. A.; Rohrer, G. S. Photocatalysts with Internal Electric Fields. *Nanoscale* **2014**, *6*, 24–42.

(10) Scott, J. F. Applications of Modern Ferroelectrics. *Science.* **2007**, *315*, 954–959.

(11) Lejman, M.; Vaudel, G.; Infante, I. C.; Gemeiner, P.; Gusev, V. E.; Dkhil, B.; Ruello, P. Giant Ultrafast Photo-Induced Shear Strain in Ferroelectric $BiFeO_3$. *Nat. Commun.* **2014**, *5*, 4301.

(12) Feng, Y.; Xu, M.; Liu, H.; Li, W.; Li, H.; Bian, Z. Charge Separation and Interfacial Selectivity Induced by Synergistic Effect of Ferroelectricity and Piezoelectricity on

$PbTiO_3$ Monocrystalline Nanoplates. *Nano Energy* **2020**, *73*, 104768.

(13) Liu, Y.; Ye, S.; Xie, H.; Zhu, J.; Shi, Q.; Ta, N.; Chen, R.; Gao, Y.; An, H.; Nie, W.; et al. Internal-Field-Enhanced Charge Separation in a Single-Domain Ferroelectric $PbTiO_3$ Photocatalyst. *Adv. Mater.* **2020**, *32*, 1906513.

(14) Senthilkumar, P.; Jency, D. A.; Kavinkumar, T.; Dhayanithi, D.; Dhanuskodi, S.; Umadevi, M.; Manivannan, S.; Giridharan, N. V.; Thiagarajan, V.; Sriramkumar, M.; et al. Built-in Electric Field Assisted Photocatalytic Dye Degradation and Photoelectrochemical Water Splitting of Ferroelectric Ce Doped $BaTiO_3$ Nanoassemblies. *ACS Sustain. Chem. Eng.* **2019**, *7*, 12032–12043.

(15) Cui, Y.; Briscoe, J.; Dunn, S. Effect of Ferroelectricity on Solar-Light-Driven Photocatalytic Activity of $BaTiO_3$ —Influence on the Carrier Separation and Stern Layer Formation. *Chem. Mater.* **2013**, *25*, 4215–4223.

(16) Fuertes, A. Metal Oxynitrides as Emerging Materials with Photocatalytic and Electronic Properties. *Mater. Horizons* **2015**, *2*, 453–461.

(17) Siritanaratkul, B.; Maeda, K.; Hisatomi, T.; Domen, K. Synthesis and Photocatalytic Activity of Perovskite Niobium Oxynitrides with Wide Visible-Light Absorption Bands. *ChemSusChem* **2011**, *4*, 74–78.

(18) Kasahara, A.; Nukumizu, K.; Takata, T.; Kondo, J. N.; Hara, M.; Kobayashi, H.; Domen, K. $LaTiO_2N$ as a Visible-Light (≤600 nm)-Driven Photocatalyst (2). *J. Phys. Chem. B* **2003**, *107*, 791–797.

(19) Aguiar, R.; Logvinovich, D.; Weidenkaff, A.; Rachel, A.; Reller, A.; Ebbinghaus, S. G. The Vast Colour Spectrum of Ternary Metal Oxynitride Pigments. *Dye. Pigment.* **2008**, *76*, 70–75.

(20) Castelli, I. E.; Olsen, T.; Datta, S.; Landis, D. D.; Dahl, S.; Thygesen, K. S.; Jacobsen, K. W. Computational Screening of Perovskite Metal Oxides for Optimal Solar Light Capture. *Energy Environ. Sci.* **2012**, *5*, 5814–5819.

(21) Hartman, S. T.; Thind, A. S.; Mishra, R. Tin Oxynitride-Based Ferroelectric Semiconductors for Solar Energy Conversion Applications. *Chem. Mater.* **2020**, *32*, 9542–9550.

(22) Van Aken, B. B.; Palstra, T. T. M.; Filippetti, A.; Spaldin, N. A. The Origin of

Ferroelectricity in Magnetoelectric $YMnO_3$. *Nat. Mater.* **2004**, *3*, 164–170.

(23) Skjærvø, S. H.; Meier, Q. N.; Feygenson, M.; Spaldin, N. A.; Billinge, S. J. L.; Bozin, E. S.; Selbach, S. M. Unconventional Continuous Structural Disorder at the Order-Disorder Phase Transition in the Hexagonal Manganites. *Phys. Rev. X* **2019**, *9*, 031001.

(24) Li, Y.; Li, J.; Yang, W.; Wang, X. Implementation of Ferroelectric Materials in Photocatalytic and Photoelectrochemical Water Splitting. *Nanoscale Horizons* **2020**, *5*, 1174–1187.

(25) Li, L.; Wang, P.; Shao, Q.; Huang, X. Recent Progress in Advanced Electrocatalyst Design for Acidic Oxygen Evolution Reaction. *Adv. Mater.* **2021**, 2004243.

(26) Rao, R. R.; Kolb, M. J.; Giordano, L.; Pedersen, A. F.; Katayama, Y.; Hwang, J.; Mehta, A.; You, H.; Lunger, J. R.; Zhou, H.; et al. Operando Identification of Site-Dependent Water Oxidation Activity on Ruthenium Dioxide Single-Crystal Surfaces. *Nat. Catal.* **2020**, *3*, 516–525.

(27) Yang, C.; Rousse, G.; Louise Svane, K.; Pearce, P. E.; Abakumov, A. M.; Deschamps, M.; Cibin, G.; Chadwick, A. V.; Dalla Corte, D. A.; Anton Hansen, H.; et al. Cation Insertion to Break the Activity/Stability Relationship for Highly Active Oxygen Evolution Reaction Catalyst. *Nat. Commun.* **2020**, *11*, 1378.

(28) Rossmeisl, J.; Qu, Z. W.; Zhu, H.; Kroes, G. J.; Nørskov, J. K. Electrolysis of Water on Oxide Surfaces. *J. Electroanal. Chem.* **2007**, *607*, 83–89.

(29) Kim, J. S.; Kim, B.; Kim, H.; Kang, K. Recent Progress on Multimetal Oxide Catalysts for the Oxygen Evolution Reaction. *Adv. Energy Mater.* **2018**, *8*, 1702774.

(30) Nørskov, J. K.; Bligaard, T.; Rossmeisl, J.; Christensen, C. H. Towards the Computational Design of Solid Catalysts. *Nat. Chem.* **2009**, *1*, 37–46.

(31) Vonrüti, N.; Aschauer, U. Catalysis on Oxidized Ferroelectric Surfaces—Epitaxially Strained $LaTiO_2N$ and $BaTiO_3$ for Photocatalytic Water Splitting. *J. Chem. Phys.* **2020**, *152*, 024701.

(32) Koper, M. T. M. Thermodynamic Theory of Multi-Electron Transfer Reactions: Implications for Electrocatalysis. *J. Electroanal. Chem.* **2011**, *660*, 254–260.

(33) Man, I. C.; Su, H. Y.; Calle-Vallejo, F.; Hansen, H. A.; Martínez, J. I.; Inoglu, N. G.; Kitchin, J.; Jaramillo, T. F.; Nørskov, J. K.; Rossmeisl, J. Universality in Oxygen

Evolution Electrocatalysis on Oxide Surfaces. *ChemCatChem* **2011**, *3*, 1159–1165.

(34) Dues, C.; Schmidt, W. G.; Sanna, S. Water Splitting Reaction at Polar Lithium Niobate Surfaces. *ACS Omega* **2019**, *4*, 3850–3859.

(35) Kakekhani, A.; Ismail-Beigi, S. Polarization-Driven Catalysis via Ferroelectric Oxide Surfaces. *Phys. Chem. Chem. Phys.* **2016**, *18*, 19676–19695.

(36) Kakekhani, A.; Ismail-Beigi, S. Ferroelectric-Based Catalysis: Switchable Surface Chemistry. *ACS Catal.* **2015**.

(37) Garrity, K.; Kakekhani, A.; Kolpak, A.; Ismail-Beigi, S. Ferroelectric Surface Chemistry: First-Principles Study of the $PbTiO_3$ Surface. *Phys. Rev. B* **2013**, *88*, 045401.

(38) Kresse, G.; Hafner, J. Ab Initio Molecular Dynamics for Liquid Metals. *Phys. Rev. B* **1993**, *47*, 558–561.

(39) Kresse, G.; Furthmüller, J. Efficient Iterative Schemes for Ab Initio Total-Energy Calculations Using a Plane-Wave Basis Set. *Phys. Rev. B* **1996**, *54*, 11169–11186.

(40) Kresse, G.; Furthmüller, J. Efficiency of Ab-Initio Total Energy Calculations for Metals and Semiconductors Using a Plane-Wave Basis Set. *Comput. Mater. Sci.* **1996**, *6*, 15–50.

(41) Perdew, J. P.; Burke, K.; Ernzerhof, M. Generalized Gradient Approximation Made Simple. *Phys. Rev. Lett.* **1996**, *77*, 3865–3868.

(42) Kresse, G.; Joubert, D. From Ultrasoft Pseudopotentials to the Projector Augmented-Wave Method. *Phys. Rev. B* **1999**, *59*, 1758–1775.

(43) Monkhorst, H. J.; Pack, J. D. Special Points for Brillouin-Zone Integrations. *Phys. Rev. B* **1976**, *13*, 5188–5192.

(44) Bengtsson, L. Dipole Correction for Surface Supercell Calculations. *Phys. Rev. B* **1999**, *59*, 12301–12304.

(45) Grimme, S.; Antony, J.; Ehrlich, S.; Krieg, H. A Consistent and Accurate Ab Initio Parametrization of Density Functional Dispersion Correction (DFT-D) for the 94 Elements H-Pu. *J. Chem. Phys.* **2010**, *132*, 154104.

(46) Neaton, J. B.; Ederer, C.; Waghmare, U. V.; Spaldin, N. A.; Rabe, K. M. First-Principles Study of Spontaneous Polarization in Multiferroic $BiFeO_3$. *Phys. Rev. B* **2005**, *71*, 014113.

(47) Stefano Baroni; Giannozzi, P.; Testa, A. Green's-Function Approach to Linear Response in Solids Stefano. *Phys. Rev. Lett.* **1987**, *58*, 1100–1103.

(48) Heyd, J.; Scuseria, G. E.; Ernzerhof, M. Hybrid Functionals Based on a Screened Coulomb Potential. *J. Chem. Phys.* **2003**, *118*, 8207–8215.

(49) Valdés, Á.; Qu, Z. W.; Kroes, G. J.; Rossmeisl, J.; Nørskov, J. K. Oxidation and Photo-Oxidation of Water on TiO_2 Surface. *J. Phys. Chem. C* **2008**, *112*, 9872–9879.

(50) Castelli, I. E.; Thygesen, K. S.; Jacobsen, K. W. Calculated Pourbaix Diagrams of Cubic Perovskites for Water Splitting: Stability Against Corrosion. *Top. Catal.* **2014**, *57*, 265–272.

(51) DTU Data Repository,Https://Doi.Org/10.11583/DTU.14528670.

(52) Fennie, C. J.; Rabe, K. M. Ferroelectric Transition in $YMnO_3$ from First Principles. *Phys. Rev. B* **2005**, *72*, 100103.

(53) Småbråten, D. R.; Holstad, T. S.; Evans, D. M.; Yan, Z.; Bourret, E.; Meier, D.; Selbach, S. M. Domain Wall Mobility and Roughening in Doped Ferroelectric Hexagonal Manganites. *Phys. Rev. Res.* **2020,** *2*, 033159.

(54) Artyukhin, S.; Delaney, K. T.; Spaldin, N. A.; Mostovoy, M. Landau Theory of Topological Defects in Multiferroic Hexagonal Manganites. *Nat. Mater.* **2014**, *13*, 42–49.

(55) Zhang, Y.; Sun, J.; Perdew, J. P.; Wu, X. Comparative First-Principles Studies of Prototypical Ferroelectric Materials by LDA, GGA, and SCAN Meta-GGA. *Phys. Rev. B* **2017**, *96*, 035143.

(56) Heifets, E.; Eglitis, R. I.; Kotomin, E. A.; Kotomin, E. A.; Maier, J.; Borstel, G. Ab Initio Modeling of Surface Structure for $SrTiO_3$ Perovskite Crystals. *Phys. Rev. B.* **2001,** *64*, 235417.

(57) Eglitis, R. I.; Vanderbilt, D. Ab Initio Calculations of $BaTiO_3$ and $PbTiO_3$ (001) and (011) Surface Structures. *Phys. Rev. B* **2007**, *76*, 155439.

(58) Castelli, I. E.; Landis, D. D.; Thygesen, K. S.; Dahl, S.; Chorkendorff, I.; Jaramillo, T. F.; Jacobsen, K. W. New Cubic Perovskites for One- and Two-Photon Water Splitting Using the Computational Materials Repository. *Energy Environ. Sci.* **2012**, *5*, 9034.

(59) Mulliken, R. S. A New Electroaffinity Scale; Together with Data on Valence States and

on Valence Ionization Potentials and Electron Affinities. *J. Chem. Phys.* **1934**, *2*, 782–793.

(60) Bouri, M.; Aschauer, U. Suitability of Different Sr_2TaO_3N Surface Orientations for Photocatalytic Water Oxidation. *Chem. Mater.* **2020**, *32*, 75–84.

(61) Bystrov, V. S.; Fridkin, V. M. Domain and Homogeneous Switching in Ferroelectrics. *Ferroelectrics* **2020**, *569*, 164–181.

(62) Lee, H.; Kim, T. H.; Patzner, J. J.; Lu, H.; Lee, J.-W.; Zhou, H.; Chang, W.; Mahanthappa, M. K.; Tsymbal, E. Y.; Gruverman, A.; et al. Imprint Control of $BaTiO_3$ Thin Films via Chemically Induced Surface Polarization Pinning. *Nano Lett.* **2016**, *16*, 2400–2406.

(63) Shetty, M.; Walton, A.; Gathmann, S. R.; Ardagh, M. A.; Gopeesingh, J.; Resasco, J.; Birol, T.; Zhang, Q.; Tsapatsis, M.; Vlachos, D. G.; et al. The Catalytic Mechanics of Dynamic Surfaces: Stimulating Methods for Promoting Catalytic Resonance. *ACS Catal.* **2020**, *10*, 12666–12695.

(64) Ruff, A.; Li, Z.; Loidl, A.; Schaab, J.; Fiebig, M.; Cano, A.; Yan, Z.; Bourret, E.; Glaum, J.; Meier, D.; et al. Frequency Dependent Polarisation Switching in H-$ErMnO_3$. *Appl. Phys. Lett.* **2018**, *112*, 182908.

(65) Gopeesingh, J.; Ardagh, M. A.; Shetty, M.; Burke, S. T.; Dauenhauer, P. J.; Abdelrahman, O. A. Resonance-Promoted Formic Acid Oxidation via Dynamic Electrocatalytic Modulation. *ACS Catal.* **2020**, *10*, 9932–9942.

TOC

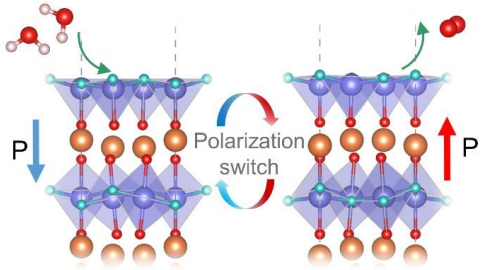

Supporting Information

Enhancing Oxygen Evolution Reaction Activity by Using Switchable Polarization in Ferroelectric $InSnO_2N$

Zhenyun Lan[a], Didrik René Småbråten[b], Chengcheng Xiao[c], Tejs Vegge[a], Ulrich Aschauer[b,*] and Ivano E. Castelli[a,*]

[a] Department of Energy Conversion and Storage, Technical University of Denmark, DK-2800 Kgs. Lyngby, Denmark

[b] Department of Chemistry, Biochemistry and Pharmaceutical Sciences, University of Bern, Bern CH-3012, Switzerland

[c] Departments of Materials and Physics, and the Thomas Young Centre for Theory and Simulation of Materials, Imperial College London, London SW7 2AZ, United Kingdom

* Corresponding Authors

Email: ivca@dtu.dk

Email: ulrich.aschauer@dcb.unibe.ch

OER mechanism

We studied the OER at standard conditions (T = 298 K, P = 1 bar, pH = 0), within the computational standard hydrogen electrode framework, by considering a widely used mechanism that consists of four proton-coupled electron-transfer (PCET) steps:[1,2]

$* + H_2O \rightarrow OH* + H^+ + e^-$, (1)

$OH* \rightarrow O* + H^+ + e^-$, (2)

$O* + H_2O \rightarrow OOH* + H^+ + e^-$, (3)

$OOH* \rightarrow * + O_2 + H^+ + e^-$, (4)

where the symbol * represents a surface reaction site and O*, OH* and OOH* are adsorbed oxygen, hydroxyl and hydroperoxy intermediates, respectively. It is assumed that the entire OER requires an energy of 4.92 eV (i.e. 1.23 eV for each of the four steps at equilibrium conditions).

We calculated the change in reaction free energy (ΔG) of each OER step as:

$\Delta G(U, pH, T) = \Delta E + \Delta ZPE - T\Delta S + \Delta G_U + \Delta G_{pH}$ (5)

where, ΔE is the reaction energy calculated from the DFT total energies and ΔZPE is the difference in zero-point energies. ΔS is the change in entropy, where for gas phase molecules values from standard tables are used [3], while the entropy of adsorbed species is assumed to be zero. The values of ΔZPE and TΔS are reported in Table S1 (Supporting Information). The effect of a bias potential on all steps involving electron transfer is accounted for by modifying the free energy difference by $\Delta G_U = -eU$, where U is the electrode potential vs SHE. The free energy of H^+ ions is corrected by the concentration dependence of the free energy, $\Delta G_{pH} = k_B T \ln[H^+] = -k_B T \ln 10 \, pH$ at $pH \neq 0$.

Since the kinetic overpotential cannot be directly determined from DFT calculations, we determine the theoretically thermodynamic overpotential (theoretical overpotential, η), which is defined as the lowest potential for which all OER steps are downhill in free energy.[1]

$$\eta = \frac{\Delta G_{max}}{e} - 1.23\ V \quad (6)$$

The largest of the four OER steps is hence the potential determining step. Since the Gibbs free energy change (ΔG) of each reaction step is equivalently affected by k_B T ln10 pH at pH≠0, the theoretical overpotential, η, is independent of pH.

The stability of the surfaces with O*/OH* coverage relative to the clean surface at pH=0 were calculated according to the following equations:[4]

$$\Delta G = \Delta E_{4O^*} - E_{clean} + 4E_{H_2} - 4E_{H_2O} + (\Delta ZPE - T\Delta S) - 8eU \quad (7)$$

and

$$\Delta G = \Delta E_{4OH^*} - E_{clean} + 2E_{H_2} - 4E_{H_2O} + (\Delta ZPE - T\Delta S) - 4eU \quad (8)$$

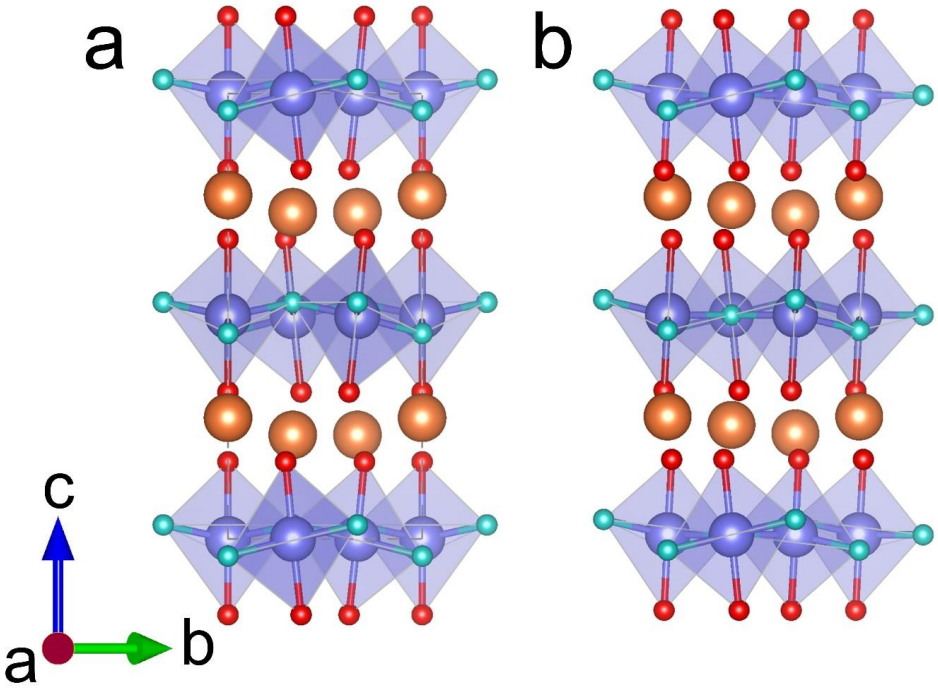

Figure S1. Structure of bulk $InSnO_2N$ with space group (a) of $P6_3cm$ and (b) $P\bar{3}c1$(centrosymmetric phase).

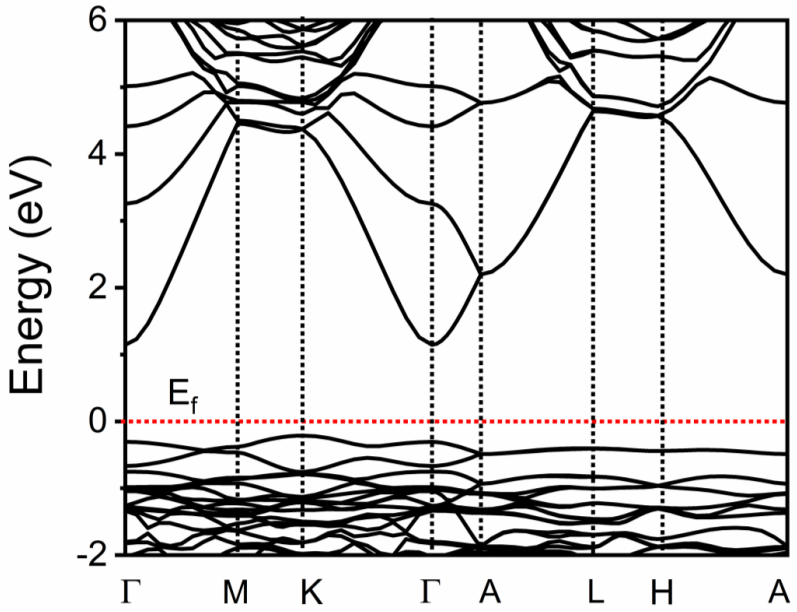

Figure S2. HSE06 band structure of bulk $InSnO_2N$ with $P\bar{3}c1$ (non-polar) space group.

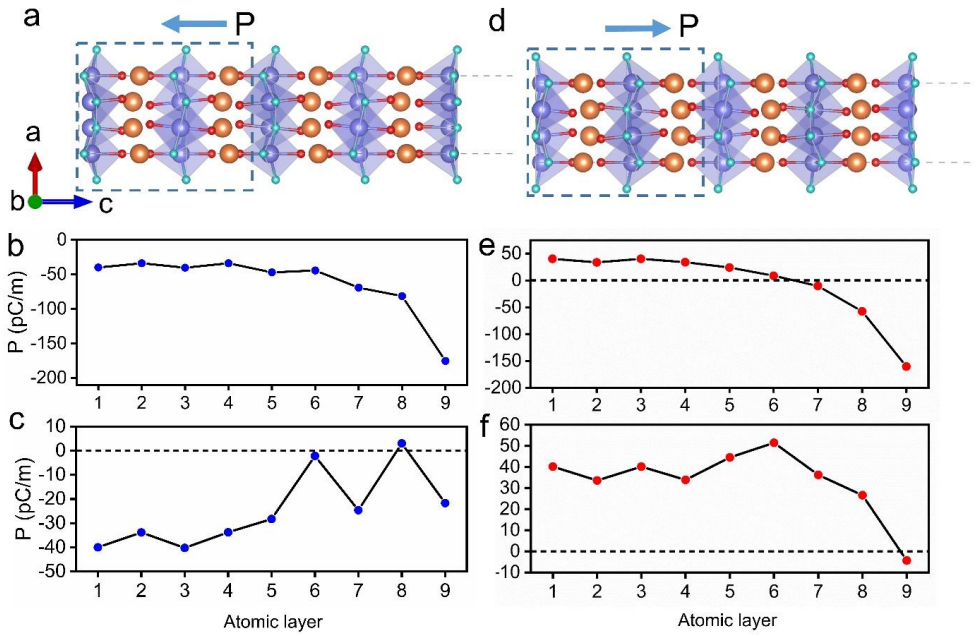

Figure S3. (a) Structure of the $InSnO_2N$ (001) surface with negatively polarized bulk. Layer-by-layer out of plane spontaneous polarization of the $InSnO_2N$ (001) surface with negatively polarized bulk using (b) the unrelaxed (c) the relaxed centrosymmetric phase as reference state. (d) Structure of the $InSnO_2N$ (001) surface with positively polarized bulk. Layer-by-layer out of plane spontaneous polarization of the $InSnO_2N$ (001) surface with positively polarized bulk using (e) the unrelaxed (f) the relaxed centrosymmetric phase as reference state. The blue arrows represent the polarization direction.

Table S1. Zero-point energy corrections and entropic contributions to free energies.[2]

	ZPE (eV)	TS (T=298 K)
H_2	0.27	0.41
H_2O	0.58	0.67
OO*+H_2O*	0.76	0
OH*	0.35	0
O*	0.07	0
OOH*	0.45	0

Table S2. Net charge of the atoms on the surface according to Bader charge analysis. Positive value indicates that the electron is removed from the atom.

	N_1 (e)	N_2 (e)	N_3 (e)	Sn_1 (e)	Sn_2 (e)	Sn_3 (e)
Negative	-1.43	-1.40	-1.40	1.87	1.87	1.87
Positive	-1.40	-1.40	-1.42	1.82	1.82	1.82

References

(1) Man, I. C.; Su, H.; Calle-Vallejo, F.; Hansen, H. A.; Martínez, J. I.; Inoglu, N. G.; Kitchin, J.; Jaramillo, T. F.; Nørskov, J. K.; Rossmeisl, J. Universality in Oxygen Evolution Electrocatalysis on Oxide Surfaces. *ChemCatChem* **2011**, *3*, 1159–1165.

(2) Valdés, Á.; Qu, Z. W.; Kroes, G.-J.; Rossmeisl, J.; Nørskov, J. K. Oxidation and Photo-Oxidation of Water on TiO_2 Surface. *J. Phys. Chem. C* **2008**, *112*, 9872–9879.

(3) Atkins, P.; de, P. J. Atkins' Physical Chemistry, 7th Edition. *Oxford Univ. Press* **2002**.

(4) Bouri, M.; Aschauer, U. Suitability of Different Sr_2TaO_3N Surface Orientations for Photocatalytic Water Oxidation. *Chem. Mater.* **2020**, *32*, 75–84.